Experimental and Numerical Investigations of Skim Milk Powder Stickiness and Deposition Mechanisms

THE UNIVERSITY OF
WAIKATO
Te Whare Wānanga o Waikato

A thesis submitted in fulfillment of the requirements for the degree of

Master of Philosophy

at

The University of Waikato

Songxin Zhao

2009

ABSTRACT

The particle gun method and Computational Fluid Dynamics (CFD) modelling was used to study stickiness and deposition mechanisms of skim milk powder in an impingement jet hitting a stainless steel plate. The particular focus was on the effect of jet velocity and particle size distribution on deposition. Low jet velocities of 10.3, 14.8 and 19.4 m/s were studied at fine particle size levels of 30, 51, and 61 μm, using a jet-plate height to jet diameter ratio of 4.

For skim milk powder with a bulk particle size (d(0.5) = 61 μm), lowering the air velocity from 19.4 m/s to 10.3 m/s increased the level of deposition and decreased the point at which deposition first occur as measured by the temperature difference between the glass transition temperature (T_g) of amorphous lactose and the air jet temperature of the particle gun. This point is called $(T\text{-}T_g)_{critical}$. The critical point decreased from 39.0 °C to 18.6 °C as the velocity decreased from 19.4 to 10.3 m/s and the $(T\text{-}T_g)_{critical}$ obtained at the lower velocity is in closer agreement with previously reported fluid bed rig results.

The $(T\text{-}T_g)_{critical}$ point and level of deposition was also found to be highly dependent on particle size. Increasing the average particle size from 30 μm to 61μm increased the $(T\text{-}T_g)_{critical}$ from 8.2 °C to 18.6 °C and 14.8 °C to 39.0 °C for jet velocities of 10.3 m/s and 19.4 m/s respectively. Levels of particle deposition also dramatically decreased for both velocity ranges.

Ring shaped deposit morphologies were observed with increasing particle stickiness. Beyond $(T\text{-}T_g)_{critical}$ powder deposits formed at the periphery of the plate creating a large round clear zone which decreased until a striped deposit ring formed and finally deposits formed only at the centre. Particles were observed to bounce radially from

the centre of the plate before sticking. Milk powder deposits are therefore governed by the kinetic energy of the impinging particle in addition to particle surface stickiness.

The particle gun method was modelled using Fluent CFD software as an adhesion phenomenon arising from the particle-surface contact dynamics of a particle laden impingement jet contacting a vertical collection plate. The development of a wall boundary condition for specifying the particle-surface interaction has been the focus. A particle is captured by the wall if the impinging kinetic energy is below the prescribed critical normal kinetic energy; otherwise the particle rebounds with reduced kinetic energy. The model was developed through the User Define Function option of Fluent.

The CFD model confirmed that particles rebound radially from the collection plate several times before sticking. Circular deposit morphology results from such modelled contact dynamics which are similar to the observed experimental deposits. The level of deposition predicted by CFD increased with increasing levels of critical normal kinetic energy, in the same way experimental deposits increased with increasing particle stickiness. The current model did not considered the contribution from the tangential velocity component to particle stick/rebound behaviour, but it is expected the tangential velocity may also play a significant role and should be included in future CFD models. It is recommended that the particle-surface interaction needs to be studied in more detail, preferably with imaging systems such as Particle Image Velocimetry (PIV), so that individual particle trajectory and deposition behaviour can be followed and analysed.

ACKNOWLEDGEMENTS

I want to express my sincere thanks to my supervisors, Dr. Michael Walmsley, Dr. James Neale and Professor Peter Kamp for their guidance, advice and encouragement during the course of my study.

Various people from Fonterra have also given me many helps, without which this project will not be what it is today. My thanks thus go to Frank Lin, Nigel Russell, Tuan Truong, Kevin Simmonds, Roger Keedwell, David Barton and David Pearce. Two people are worth special mentioning. I deeply appreciate the many hours put in by Dr. Hong Chen from Fonterra and Dr. Tony Paterson from Massey University. Their willingness to go the extra mile to give help and more importantly their integrity are what makes them the role models for the rest of my life.

I would like to thank the staff and my fellow students in the Energy Research Group for their friendship and assistance. The useful discussions with Jonas and Martin, and the great coffee and chitchat during lunch time with Hamish and Lance are wonderful memories.

Thanks also go to the technical staff at the School of Science and Engineering, especially Yuanji Zhang, Annette Rogers, Steve Hardy and Paul Ewart for their support in various aspects of my project.

No words can describe my gratefulness for the unconditional loves from my parents and wife. Their love is the reason that I will endeavour to achieve higher level of excellence in my life.

TABLE OF CONTENTS

LIST OF FIGURES

LIST OF TABLES

NOMENCLATURE

a	particle radius in Frenkel's equation (m)
a_w	water activity
c	constant in GAB equation
C	particle concentration (kg/m^3)
C_1	WLF equation constant
C_2	WLF equation constant
D	pipe diameter (m)
D	moisture diffusivity (m^2/s)
D_B	particle Brownian diffusivity (m^2/s)
d_p	particle diameter (m)
E_{ad}	kinetic energy lost due to surface adhesion (J)
E_i	incoming kinetic energy of the particle (J)
E_{pd}	kinetic energy lost due to plastic deformation (J)
E_r	available kinetic energy for particle rebound (J)
F_A	fraction of particle affected by moisture diffusion
f	constant in GAB equation
g	gravity (m^2/s)
H	distance between pipe exit and impingement plate (m)
J_B	particle flux (kg/m^{2}s)
K	ratio of liquid bridge diameter to particle diameter
k	constant in Gordon-Taylor equation
k	turbulent kinetic energy (m$^{2/}$s^2)
M	moisture content (g water / g dry powder)
M_o	mono layer moisture content (g water / g dry powder)
m	mass (kg)
n	spread parameter in Rosin-Rammler equation
P_{vap}	partial vapour pressure (Pa)
P_{sat}	saturation vapour pressure of air (Pa)
P_{air}	partial air pressure (Pa)
P_{tot}	total pressure (Pa)
p	vapor pressure of water in powder (Pa)
p_0	vapor pressure of pure water (Pa)
R	particle radius (m)
Re	Reynolds number
RH	relative humidity (%)
T	temperature (°C)
T_g	glass transition temperature (°C)

T_L	fluid Langragian integral time (s)
t	time (s)
u	x component of velocity (m/s)
u^*	friction velocity (m/s)
V	velocity vector (m/s)
V_{cr}	critical deposition velocity (m/s)
V_n	normal deposition velocity (m/s)
V_t	tangential deposition velocity (m/s)
V_p	particle velocity (m/s)
V_{dep}	particle deposition velocity (m/s)
V_{dep}^+	dimensionless deposition velocity
v	y component of velocity (m/s)
w	z component of velocity (m/s)
w_1	weight fraction of amorphous solid
w_2	weight fraction of water
x	inter-particle liquid bridge radius (m)
Y_d	mass fraction of particles of diameter greater than d_p
y^+	dimensionless distance from wall
α_{cr}	critical angle of incidence (degree)
ε	eddy diffusivity of particles (m^2/s)
κ	constant in the equation of Downton *et al.* (1982)
ρ	density of air (kg/m^3)
ρ_p	density of particle (kg/m^3)
σ	surface tension (N/m)
τ_e	eddy life time (s)
τ_p	particle relaxation time (s)
τ_p^+	dimensionless particle relaxation time
μ	viscosity (Pa s)
$\mu_{critical}$	critical viscosity for stickiness (Pa s)
μ_g	viscosity at the glass transition temperature (Pa s)

CHAPTER 1 – PROJECT OVERVIEW

1.1 INTRODUCTION

Deposition of particles from turbulent flows has been the focus of many scientific investigations since the 1950s. In many industries and applications ranging from ultraclean integrated circuit manufacturing, air pollution control to therapeutic drug delivery in human airways, it is often important to predict and in some cases control particle deposition accurately (Li, 1995). In New Zealand, the subject of particle deposition is of particular importance to the dairy sector, which is by far the country's largest industry with annual exports of several billion dollars.

During spray drying of milk into powders, milk powder deposition is likely to occur in the spray dryer chamber, fluidized beds, the exhaust ducts and the cyclones. This is undesirable due to a number of reasons. First of all, it may result in fire and explosion in the plant. It is known that powder deposits may catch fire spontaneously if they attain a critical thickness and the temperature is above the ignition point of the powder (Beever, 1985; Chong *et al.*, 1999). A more frequent problem caused by milk powder deposition is the need to halt the dryer operation regularly and clean the deposits. Extensive deposits formation will encourage the growth of microbes and pathogens. Deposits are also prone to scorching and browning. As a result, when the deposits get re-entrained and mix with milk powders in the airflow, they may affect the appearance of the final products or even cause food safety issues. A more dramatic consequence of deposition is the blockage of the cyclone separators, which is at least partly caused by milk powder deposition or powder cohesion. When this occurs, the dryer needs to be shut down immediately, leading to significant plant downtime and loss of products. Therefore, it is desirable to be able to predict and control particle deposition in milk

powder plants.

A lot of research has been done in this area. Most of the studies have focused on modeling the stickiness development of milk powders without considering their interaction with the flow field in the exhaust ducts and cyclones. On the other hand, researchers studying the detailed flow field of cyclone separators have not specifically looked at milk powder as their material of interest. In this thesis milk powder stickiness development and flow field interactions are studied with the aim of elucidating additional flow related factors that contribute to milk powder deposition such as impact velocity, impact angle and particle size. Experimental and numerical techniques are applied to the investigation.

1.2 RESEARCH PROBLEMS

Currently industrial practices rely on the use of a sticky point curve for controlling powder deposition. The sticky point curve is a line defined by a combination of critical temperature and relative humidity. Conditions below the curve are deemed the safe drying zone, where milk powder stickiness and deposition are not expected to occur. Recent studies undertaken by researchers from Massey University with the particle gun stickiness testing rig (Chatterjee, 2004; Zuo, 2004; Murti, 2006) have shown that particle stickiness and deposition may be also controlled by factors such as air velocity and particle size, in addition to the effect of air temperature and humidity. Understanding how these additional factors affect the particle deposition process is the focus of this thesis and findings may open up new ways to control the problem.

1.3 PROJECT OBJECTIVES

The objectives of the current research were:

(1) To modify the particle gun stickiness test method so it can be used to test particle deposition at velocities lower than 20 m/s. Previous attempts to do this have encountered problems of extensive agglomeration of particles and this needs to be overcome so a wider range of air velocities can be tested.

(2) To investigate the effect of milk powder particle size on stickiness and deposition using the particle gun test.

(3) To use Computational Fluid Dynamics to characterise the flow field of the impingement air jet emanating from the particle gun rig and simulate the milk powder deposition process in such a flow field.

1.4 THESIS STRUCTURE

A literature review will first be given in Chapter 2 on the subject of dairy powder stickiness mechanisms and glass transition theory. Different stickiness testing methods are then compared and contrasted. Chapter 3 gives a detailed account of the past works done with the particle gun rig as well as the experimental work done in this study. The methods and procedures developed for the current experimental study are explained and the results obtained are presented and discussed. In Chapter 4, the basic principles of Computational Fluid Dynamics are reviewed, followed by a discussion of particle transport and deposition mechanisms. At the end of Chapter 4, a case study of using CFD to model particle deposition from turbulent flows in a

straight duct is illustrated. Chapter 5 details the procedures of CFD modelling of the particle gun setup and introduces a wall boundary model for describing particle stick/rebound behaviour at wall surface. The results of the project are summarized in Chapter 6, together with recommendations for further works in this area.

CHAPTER 2 - LITERATURE REVIEW OF DAIRY POWDER STICKINESS AND STICKINESS DETERMINATION

2.1 INTRODUCTION

Stickiness is a commonly encountered issue during milk spray drying and storage of dairy powders containing low-molecular weight sugar such as lactose. It leads to particles adhering to the chamber of the spray dryer wall and the exhaust ducts, resulting in loss of product and reduced plant availability due to cleaning. It is the main material property that contributes to particle deposition. In this chapter, a literature review on the causes of dairy powder stickiness and how it can be measured is given.

2.2 MAIN STAGES OF MILK SPRAY DRYING

The first step of milk spray drying is the atomization of milk concentrates into tiny droplets. The most common types of atomizers used industrially are the pressure nozzle atomizer and rotary atomizer. The droplets sizes produced by both types of atomizers are generally in the range of 10 – 200 μm (Stevenson, 1999). The resultant fine mist of droplets is mixed with a stream of hot air, often in excess of 180 °C and with very low relative humidity. During the mixing and transport step in the dryer, intense evaporation of moisture from the droplets takes place, with the droplets undergoing several physical changes and transforming from a liquid form to solid

particles (Chen, 1994; Kentish *et al.*, 2005) The last step involves the separation of the dried products from the air stream, and this is often achieved industrially with cyclone separators and baghouses.

Stickiness and particle deposition are known to occur during both the active drying stage as well as the powder separation stage. Chen *et al.* (1993) measured deposits formation on a large industrial compact disc dryer producing skim and whole milk powders over a four month period. Particle deposition was found to occur on the dryer ceiling as well on the side wall and lower cone of the dryer chamber. The authors attributed particle deposition mechanisms to direct impact of wet concentrates as well as dry but sticky particles. Ozmen and Langrish (2003) carried out experiments with a pilot-scale spray dryer and found that the deposition flux of skim milk powder on the dryer wall was a strong function of the air inlet swirl vane angle. They concluded that a high swirl vane angle (30° in their study) would increase the extent of air swirling and particle spreading, which in turn lead to more particles being transported to the wall. Bhandari and Howes (2005), in their review of contributions of powder and wall material surface energetic to stickiness, proposed that blockage of powder transport lines and cyclones are caused by powder cohesion (i.e. powder to powder contact), which is initiated by adhesion.

Particle stickiness and deposition is clearly undesirable and should be avoided. In addition to direct experimentation using spray dryers, many studies have looked at the fundamental causes of the problem, i.e. composition-dependency and particle-air interaction. A number of laboratory-scale stickiness testing methods have also been developed and these techniques vary in complexity and the actual stickiness mechanism under consideration.

2.3 DEVELOPMENT AND CAUSES OF PARTICLE STICKINESS

2.3.1 Mechanisms of Sticking

Stickiness of particle is manifested through its tendency to stick to one another or surfaces of other materials. The former is known as cohesion and the latter adhesion. Both cohesion and adhesion can coexist and under specific conditions one form can be more dominant than the other. For example, the caking of dairy powders during handling and storage is mainly due to cohesion while the early stages of particle deposition inside spray dryer chambers is caused by adhesion. According to Papadakis and Bahu (1992), there are five general mechanisms causing particles to stick to each other.

- van der Waals Force
- Electrostatic Force
- Mobile Liquid Bridges
- Immobile Liquid Bridges
- Solid Bridges

In almost of all cases of sticking and caking involving dairy powders, the liquid bridges formed between particles are dominant over van der Waals force and electrostatic force, by several orders of magnitude (Zuo, 2004). Immobile liquid bridges are formed by the introduction of thin layers of viscous binders on the surface of the particles. They are formed due to the viscosity of amorphous substances being sufficiently low and liquid enough to cause viscous flow driven by surface energy.

Figure 2.1 shows the development of stickiness and formation of liquid bridges between two particles.

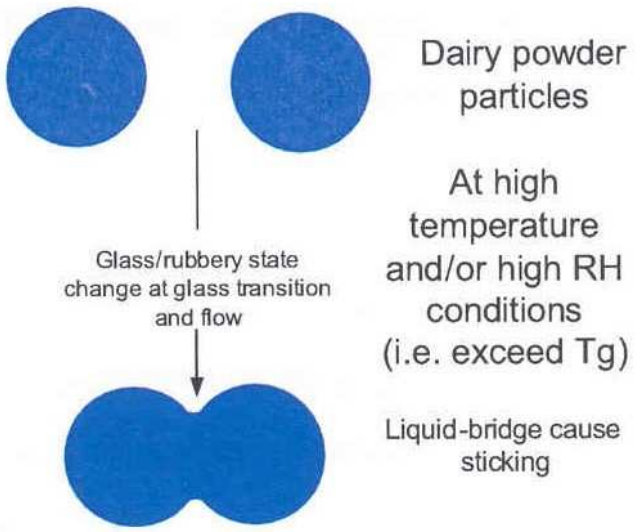

Figure 2.1 Diagram of dairy powders containing amorphous sugars sticking, taken from Zuo (2004).

2.3.2 Glass Transition and Molecular Mobility

Figure 2.1 shows that for the particles to develop the liquid bridge, they need to undergo a critical step, namely, glass transition. The glass transition is closely related with the viscosity and molecular mobility of the amorphous sugars in the dairy powders (Fennema, 1996). For glass transition to occur, a critical combination of particle temperature (T) and moisture content (or ambient air RH) must be reached (Paterson *et al.*, 2005; Boonyai *et al.*, 2005).

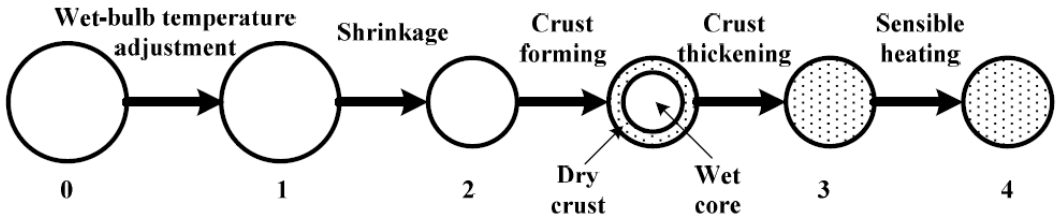

Figure 2.2 Stage of drying and physical changes, taken from Patel (2009).

Figure 2.2 shows an overview of the drying process for a single droplet. Prior to the start of drying, the droplet temperature may be below or above the corresponding wet bulb temperature of the drying air and it adjusts itself towards this temperature. Evaporation of the droplet's free water then begins and it is accompanied by the rapid shrinkage of the droplet until a crust starts to form on the surface of the partially dried particle. Due to the rapid dehydration rate, the solids formed in this way will have an amorphous form. A solid in its amorphous state is generally called a glass and is characterized by the random arrangement of its molecular constituents. Amorphous solid is at a non-equilibrium, high energy state compared to its crystalline, more stable counterpart (Fennema, 1996). As drying proceeds further, the entire wet core is converted into the glassy, solid form. Figure 2.3 shows the formation of glassy and crystalline materials.

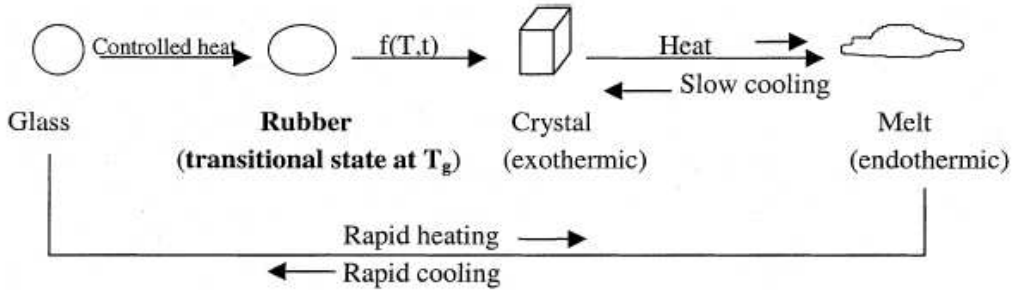

Figure 2.3 Physical states of material during drying, taken from Bhandari and Howes (1999).

The entire spray drying process is very short, on the order of seconds. Thus, the particles produced by spray drying are often amorphous or partially amorphous and they are characterized by a phenomenon known as glass transition. Glass transition is a process by which a supersaturated solution, in this case the milk concentrate, coverts into a glassy solid containing randomly aligned molecules. On the other hand, glass transition is also said to occur if the glassy material receives heat and switches into a rubbery state, as shown in Figure 2.3. Thus the glass transition is a two-way process and the temperature at which this occurs is termed the glass transition temperature, T_g. Below the glass transition temperature, the glassy material is solid and stable and is characterized by extremely high viscosity, on the order of 10^{12} Pa s (Downton *et al.*, 1982). Above the glass transition temperature, the material is in an unstable, rubbery state, with correspondingly low viscosity and more prone to physical and chemical changes such as stickiness development.

At the glass transition of a material several physical changes also take place, which allows this transition to be measured experimentally. The most common type of measurement is the differential scanning calorimetry (DSC), which is based on the monitoring of the step change in material's specific heat capacity at glass transition. Figure 2.4 shows a typical DSC curve following the heat flow through a material undergoing glass transition. As shown in Figure 2.4, the glass transition is not a single step process but takes place over a temperature range. Various definitions of T_g have been reported in literature and these include the T_g onset, T_g extrapolated onset, T_g midpoint and T_g endpoint. This tends to cause discrepancies and makes it difficult to compare the reported T_g for the same material (Foster, 2002).

Other measurement techniques for the glass transition temperature such as the dynamic mechanical thermal analysis (DMTA) and nuclear magnetic resonance (NMR) are reliant upon the detection in the changes of mechanical or dielectric properties of the material of interest (Zuo, 2004).

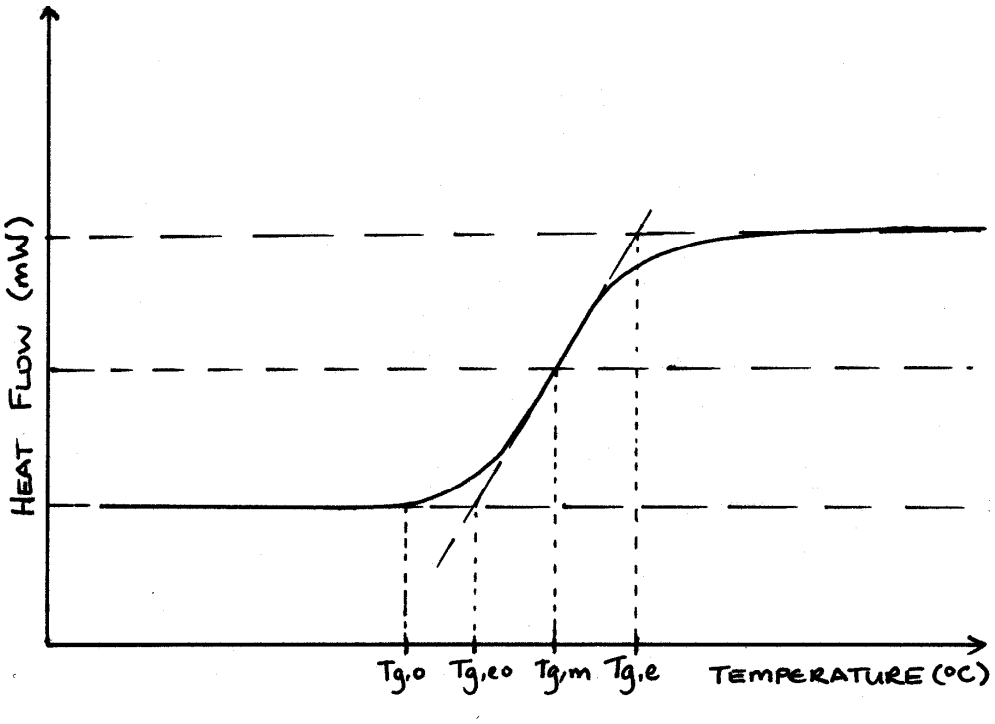

Figure 2.4 Differential scanning calorimetry curve following glass transition, taken from Foster (2002).

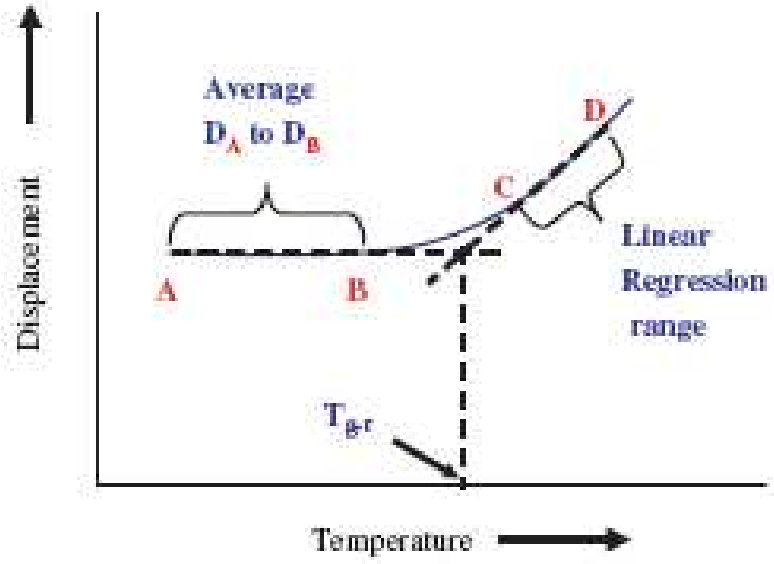

Figure 2.5 T_g analysis from the thermal mechanical compression test, taken from Boonyai *et al.* (2007).

Boonyai (2005) has developed a thermal mechanical compression (TMCT) test that involves the compression of a thermally controlled powder sample with a texture analyzer. It is based on the changes in the free volume and molecular mobility of the amorphous materials at glass transition. The results are obtained in the form of a displacement-temperature diagram (Figure 2.5) and the temperature at which the displacement of the compression probe significantly increases is taken to be the glass transition temperature. The technique is validated using skim milk powder and the resultant T_g has been shown to be in excellent agreement with the value obtained by DSC.

The glass transition temperature is a function of the moisture content and constituents present in a specific material. This dependence is best illustrated with the concept of molecular mobility, which is a measure of the translational and rotational motions of the constituent molecules in the amorphous powder (Fennema, 1996). As the temperature of an amorphous material is cooled, the translational and rotational movement of its molecules are slowed down accordingly, resulting in a high apparent viscosity. Below the glass transition temperature, the movement of molecules become sufficiently small and diffusion related local events are extremely slow. However, the molecular mobility will increase with a rise in a temperature, with the accompanying rise in the free volume of the polymer segments and decrease in viscosity. Alternatively, the molecular mobility can be increased by the addition of low-molecular weight component at the same temperature. In dairy powders, the amorphous regions usually consist of carbohydrates and proteins, both of which are know to undergo glass transition. However, the glass transition behaviour of dairy powders as a whole (the change in molecular mobility, specific heat capacity etc) is usually governed entirely by the low-molecular weight carbohydrate component. The resultant T_g of the powder is a direct function of the average molecular weight of its sugar component, reflecting the fact that small molecules are easier to diffuse and move about and have a higher molecular mobility than large molecules at the same temperature. Water is another low-molecular weight component that can enhance the

molecular mobility and depress the T_g of the amorphous powder. This is especially true for dairy powders containing significant amount of sugars such as lactose and sucrose, which are very hydrophilic. Macroscopically, the enhanced molecular mobility of the amorphous powders due to the presence of water and low-molecular components are manifested through the fluidity of the material such as the ability to form liquid bridges, especially at temperatures above T_g.

There are a number of models available for predicting the glass transition temperature of a material, taking into account the plasticizing effect of water and low-molecular weight components. The most popular model is the Gordon-Taylor equation (Equation 2.1), from which many other more complex equations are also developed.

$$T_g = \frac{w_1 T_{g1} + k w_2 T_{g2}}{w_1 + k w_2} \qquad (2.1)$$

where w_1 and w_2 are the weight fractions, and T_{g1} and T_{g2} are the glass transition temperatures of the solid and water respectively. *k* is an experimentally derived constant for the specific material. The commonly accepted value for the T_{g2} (water) is -135 °C and thus Equation 2.1 shows that the depressive effect water has on the overall glass transition temperature of the material is very significant, and more so when water is present in large amount. The Gordon-Taylor equation is only applicable for a binary mixture of solids and water. For more complex, multi-component mixtures, the Couchmann-Karasz equation or the numerical model developed by Foster (2005) based on the weighted addition of individual T_g of amorphous sugars at given water activity may be more appropriate.

2.3.3 Moisture Sorption Isotherm

According to Brooks (2000), determination of the moisture content of low-molecular weight sugars such as lactose in commercial dairy powder can be difficult due to the presence of other components such as fat, protein and ash. These components will affect the overall moisture content of the powders while the T_g is mostly controlled by the sugar alone. The author reasons that the water activity a_w is a better measurement to use, as it is easily measured and fairly constant among the various components of the dairy powders (Zuo, 2004). The moisture content and water activity of a food material is related through the moisture sorption isotherm, which is a plot of water content of a food versus its relative vapor pressure p / p_0 at constant temperature. The term water activity is used to account for the intensity with which water associates with various non-aqueous constituents in food and at ambient pressure it is the same as the relative vapor pressure.

$$a_w = \frac{p}{p_0} \tag{2.2}$$

where p is the vapor pressure of water in the substance, and p_0 is the vapor pressure of pure water at the same temperature.

Moisture sorption isotherms are typically prepared from resorption isotherms by equilibrating initially dry foods with air conditioned at certain temperatures and relative humidities and measuring the weight gain. There are a number of predictive models in literature for the moisture isotherms of various pure sugar component as well as multi-component dairy powders (Chen, 1997; 1998). The most common models for dairy powders include the Guggenheim-Anderson-de Boer (GAB) model (Equation 2.3) and the Brunauer-Emmett-Teller (BET) model.

$$M = \frac{M_o c f a_w}{(1 - f a_w)[1 + (c - 1) f a_w]} \qquad (2.3)$$

where M is the moisture content, M_o is the mono layer moisture content, c and f are constants and a_w is the water activity.

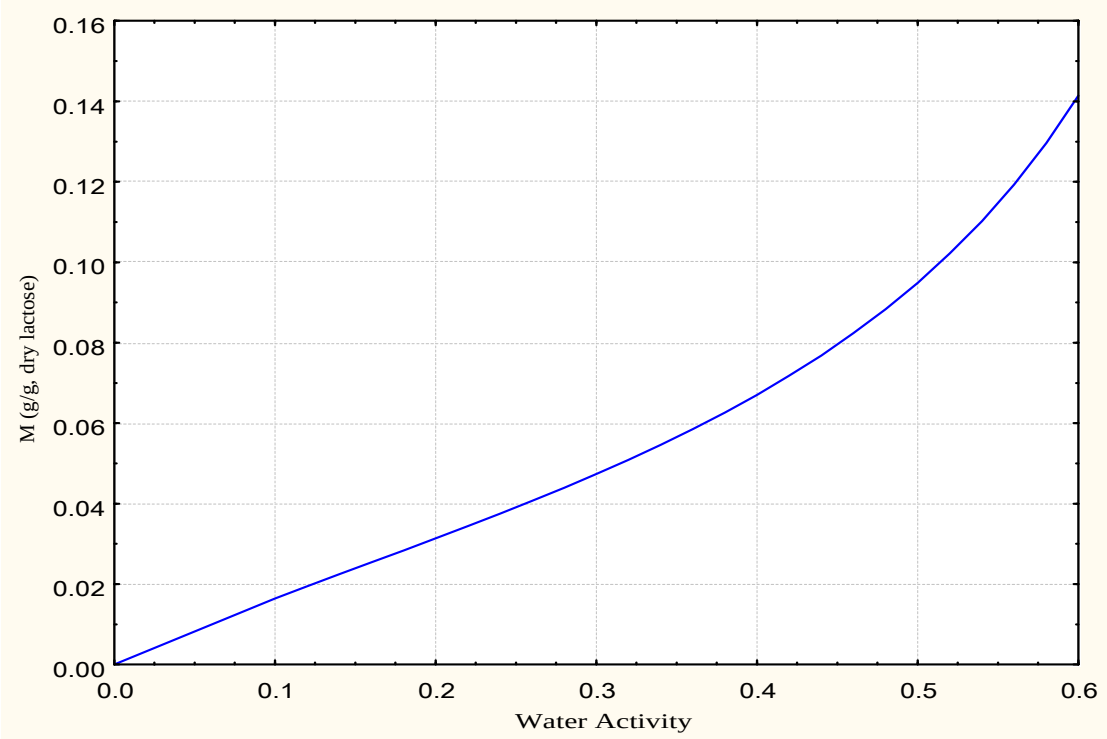

Figure 2.6 Moisture sorption isotherm for amorphous lactose, data from Bronlund and Paterson (2004).

Bronlund and Paterson (2004) obtained experimentally the moisture sorption isotherm for amorphous lactose and found no temperature dependence in the range of 20 – 40 °C. They found the GAB model fitted the experimental data very well and recommended a value of 0.0488 g/g for M_o, 1.16 for f and 3.23 for c. Figure 2.6 shows this moisture sorption isotherm for amorphous lactose.

Moisture sorption isotherms for foods are useful for many purposes. The physical and chemical stability of foods are often cited in terms of water activity. The survival rate of spoilage and pathogenic bacteria are often given in literature as a function of water

activity. In dehydration operations such as spray drying, the moisture sorption isotherm is used for estimating the final moisture content a specific material can be dried to. As mentioned previously, the water activity of a food powder is the same as the relative vapor pressure (relative humidity) at equilibrium. Thus, to achieve a specific final moisture content of the final dairy powders at the spray dryer outlet, the relative humidity of the drying air must be at the level dictated by the isotherm.

Brooks (2000) has done a comprehensive literature review of the moisture sorption isotherm and T_g/moisture content relationships for amorphous lactose. He has proposed a third-order polynomial equation (Equation 2.4) that can be used for the direct prediction of the T_g for amorphous lactose based on the measured water activity up to an a_w of 0.575. This approach is adopted by a number of researchers (Chatterjee, 2004; Zuo, 2004; Murti, 2006) and is also used in this study for the particle gun experiments to be addressed in later chapters.

$$T_g = -530.66(a_w)^3 + 652.06(a_w)^2 - 366.33a_w + 99.458 \qquad (2.4)$$

2.3.4 Sticky Point – the T-T_g Approach

It has been discussed previously that the molecular mobility of an amorphous material is intricately related with the glass transition temperature T_g. Experimentally the change in molecular mobility is usually taken to be synonymous with the concept of viscosity, which is very useful for explaining the sticking and caking phenomenon in dairy powders. The ability for two particles in contact to develop a liquid bridge and stick to each other is dependent on whether the viscosity of the interfacial material is sufficiently low and mobile enough to flow. Downton *et al.* (1982) proposed a model (Equation 2.5) for the critical viscosity needed for sticking to occur between the same materials.

$$\mu_{critical} = \frac{\kappa\sigma t}{Kd_p} \tag{2.5}$$

where κ is a constant in the order of unity, σ is the surface tension, t is the contact time, K is the liquid bridge diameter expressed as a fraction of the particle diameter (in the range of 0.01 – 0.001), d_p is the particle diameter and $\mu_{critical}$ is the critical viscosity. Among other things, Equation 2.5 shows that the critical viscosity required is proportional to particle contact time. Thus a much lower viscosity is required for particle sticking and deposition during spray drying, given the short residence time and contact time of the particles, compared to that during powder storage. Downton *et al.* (1982) predicted the critical viscosity for a sucrose/fructose mixture to be in the range of 10^6 – 10^8 Pa.s. Another similar model to Equation 2.5 is that Frenkel's equation.

$$\mu_{critical} = \frac{3}{2}\frac{\sigma t a}{x^2} \tag{2.6}$$

where σ and t are the surface tension and contact time as in Equation 2.5, a is the particle radius and x is the inter-particle liquid bridge radius.

The Frenkel's equation is used by Wallack and King (1988) for estimating the critical viscosity values of a sugar mixture and coffee extract. The same range of critical viscosity of 10^6 – 10^8 Pa.s was obtained for the sugar mixture as in the experiment of Downton *et al.* (1982), thus supporting its validity. Relatively short particle contact times were used in both works (in the range of 1 – 10 seconds), and therefore the critical viscosity obtained is applicable for the rate of the stickiness development as observed during spray drying.

The temperature dependence of molecular mobility and changes in food properties that depend strongly on molecular mobility are far greater in the temperature range

above T_g than those below T_g. This is also true for viscosity, which is typically on the order of 10^{12} Pa.s or higher at temperatures below T_g. In this range, all the molecular movements are very subdued and no surface tension driven viscous flow, i.e. stickiness, is observable. Above the glass transition temperature, the rate of change in viscosity with temperature becomes very intense and can be typically described by the Williams-Landel-Ferry (WLF) equation.

$$\log(\frac{\mu}{\mu_g}) = \frac{C_1(T - T_g)}{C_2 + (T - T_g)} \tag{2.7}$$

where μ is viscosity at product temperature, μ_g is viscosity at glass transition temperature, C_1 and C_2 are constants having values of -17.44 and 51.6, respectively. The WLF equation shows that the viscosity of the material decreases as the glass transition temperature is exceeded. The higher the actual temperature is in excess of T_g, the lower is the viscosity.

The WLF equations specifies the viscosity as a function of $T\text{-}T_g$ while the models of Downton *et al.* (1982) and Frenkel's equation show that the critical viscosity for sticking to occur is a rate-limiting process. In recognition of this, Paterson *et al.* (2005) combined the Frenkel and WLF equations and expressed the rate of stickiness development as a function of $T\text{-}T_g$ (Equation 2.8).

$$\log(\frac{x^2}{t}) = \log(\frac{3a\sigma}{2\mu_g}) - \frac{C_1(T - T_g)}{C_2 + (T - T_g)} \tag{2.8}$$

where x is the inter-particle bridge radius similar to the Frenkel's equation. If x is taken to be a general indicator of stickiness development, then Equation 2.8 shows that to achieve the same stickiness strength, a larger $T\text{-}T_g$ is required for a shorter time and vice versa.

2.4 DETERMINATION OF STICKY POINTS

In the literature a number of techniques have been developed over the years to study the stickiness development and particle deposition behavior of amorphous food powders. They all share the common principle of using $T-T_g$ as the key experimental variable and $T-T_g$ at which the powders start to show stickiness is termed the sticky point.

2.4.1 Propeller Driven Method

The propeller driven test was developed by Lazar *et al.* (1956) for testing the sticky point temperature of amorphous spray dried food powders. Its operation involves the stirring of a powder sample embedded in a test tube, either manually or mechanically with a propeller. To control and vary the temperature of the sample, the test tube is submerged in a heated water bath. During the experiment, the water bath temperature is increased slowly at a specific rate with the propeller continuously stirring the sample. Stickiness will develop with the heating and at one stage the powders start to interact with one another extensively and form a lump. When the force required to stir the sample increases sharply, the temperature at which this happens is recorded as the sticky point temperature. It has been realized that the sticky points obtained are an inverse function of the original moisture content of the powders, due to the plasticising effect of water. Thus, the entire experiment usually involves repeating the procedures for powders with different moisture content.

The original design of the technique by Lazar *et al*. (1956) has been continuously modified by other researchers to improve the reliability and reproducibility of the results. Hennigs *et al.* (2001) measured the sticky points of skim milk powders using an improved propeller driven method (Figure 2.7). The test tube in the original setup

of Lazar *et al.* (1956) was replaced with a hermetically sealed flask to minimize the moisture evaporation of the sample. The temperature of the sample is directly measured with a thermocouple when the water bath is heated. The stirrer is driven by a DC motor, rather than manually, to give consistent results. The sticky points are considered to be reached when the stirrer stops rotating and the voltage across the resistor in the system increases sharply. The authors plotted the sticky points of skim milk powders as a function of the moisture contents (Figure 2.8). They have also used the Gordon-Taylor equation (Equation 2.1) for the glass transition temperature of amorphous lactose with a *k* value of 7.40. It is found that the sticky points of skim milk powders are consistently above the T_g of amorphous lactose with a constant offset of 23.3 °C. This is also one of the first reported studies for the sticky point temperature for SMP. In this case, it is concluded that SMP will become sticky at conditions of $T - T_g \geq 23.3°C$.

Due to its design, the propeller driven method detects the stickiness behaviour of amorphous food powders through the onset of cohesion. It is useful as a guideline for specifying the safe drying zone and handling of food powders.

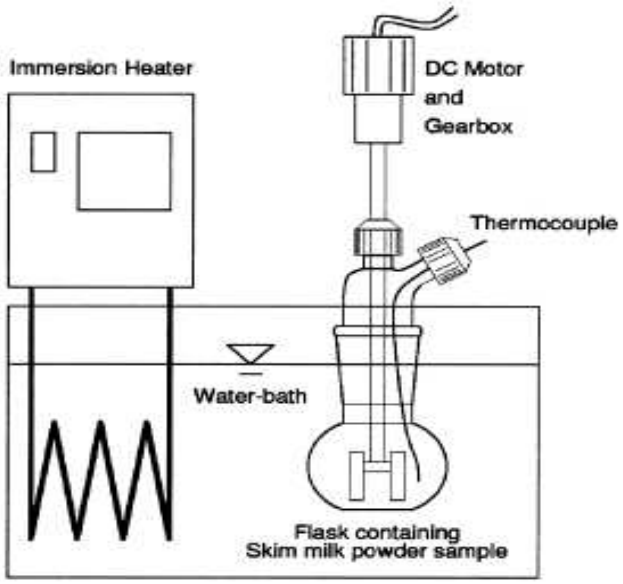

Figure 2.7 The improved propeller driven method by Hennigs *et al.* (2001).

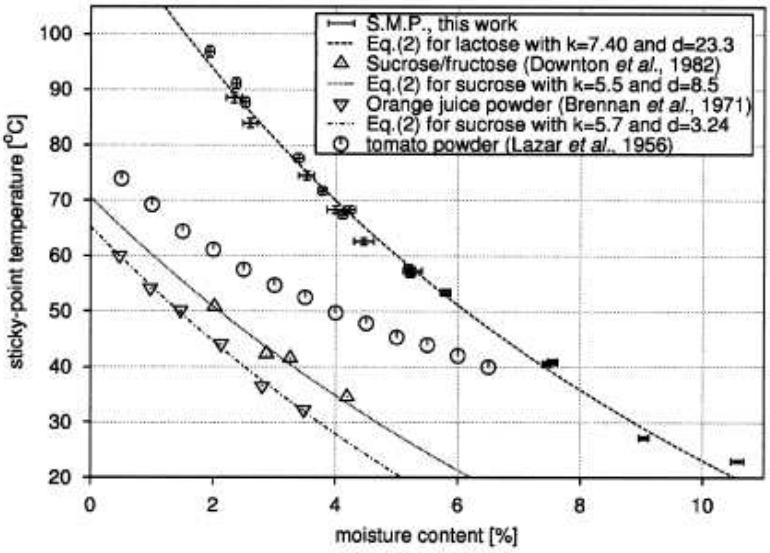

Figure 2.8 Sticky point temperature versus moisture content for skim milk powders, taken from Hennigs *et al.* (2001).

2.4.2 Fluid Bed Test Method

The propeller driven method discussed previously is a static mechanical method involving a fixed powder bed, whereas in spray drying and particle transport, the powders are suspended in the air flow. The fluid bed test is one of the pneumatic methods developed in recent years to study the stickiness development of dairy powders in an environment that is more similar to the actual spray drying process. Figure 2.9 shows the schematic diagram of the fluid bed rig developed at Massey University in conjunction with Fonterra Research Centre. Many other fluid bed test setups in literature are also similar.

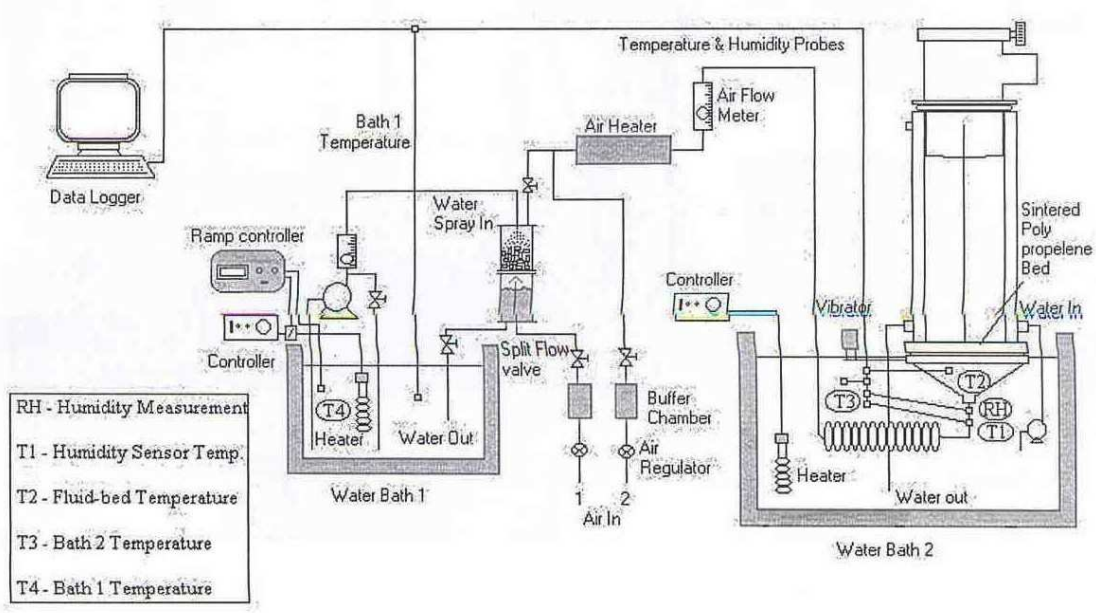

Figure 2.9 Schematic diagram of the fluid bed rig, taken from Chatterjee (2004).

The setup in Figure 2.9 consists of two thermally controlled water baths. Water from the first bath is pumped at a controlled rate to the top of a humidity column packed with tiny pieces of plastic tubing. The water is then sprayed or “atomized” and runs down the humidity column with air flowing up the column in the opposite direction. This step aims to humidify the laboratory air supply to saturation level and the plastic tubing is there to increase the contact area between the air stream and water droplets. The saturated air is then directed through an air heater and tubing immersed in a second water bath, which is essentially a two step heating process to raise the dry bulb temperature of the air. Such an arrangement makes it possible to produce a stream of air with controlled flow rate, dry bulb temperature and relative humidity. The conditioned air is passed through a sintered polypropylene disc embedded at the bottom of a glass fluid bed and used to fluidise the powder samples contained in it.

Chatterjee (2004) used this setup for determining the sticky point temperatures of a range of amorphous and crystalline dairy powders. The mass of the sample used is typically between 20 and 30 grams and the air flow rate is between 26 and 50 LPM,

corresponding to 0.22 and 0.42 m/s, respectively. Below the sticky point temperature, the powders are very free flowing and easily fluidized. The stickiness of the powders is induced by raising the temperature of water bath 1 at a slow and controlled rate (1 °C for every 5 minutes is recommended). This basically leads to a rise in the wet bulb temperature and relative humidity of the air stream, which in turn depresses the T_g of the particle surface. The endpoint of the test is reached when the complete seizure of the particle bed occurs, i.e. the powders are no longer fluidized. The temperature and RH in the fluid bed are continuously logged and by carrying out the experiments at a number of dry bulb temperatures, a graph similar to Figure 2.8 can be constructed.

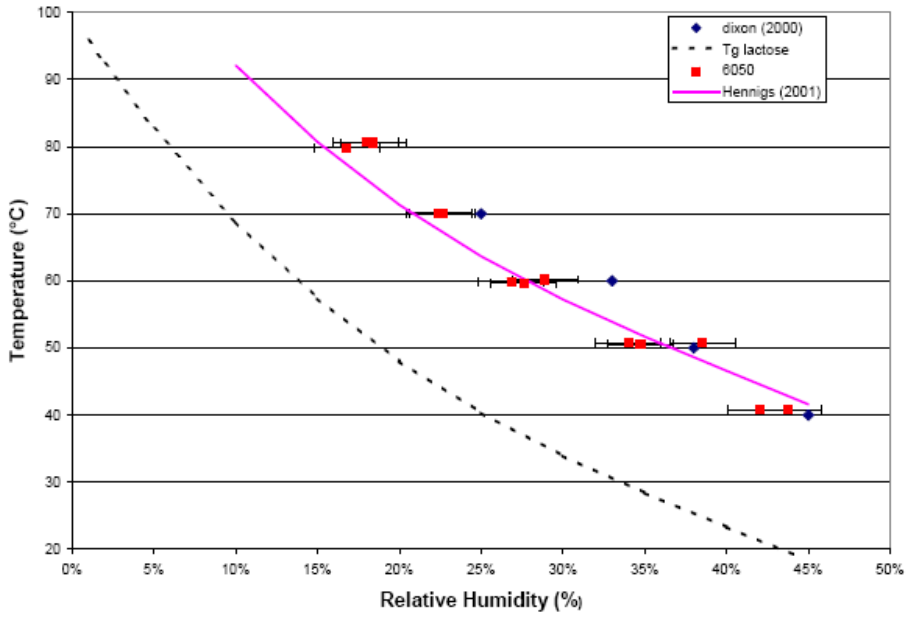

Figure 2.10 Sticky point curves for skim milk powder (red square-, pink line – Hennigs *et al.* (2001), dotted line, Tg line of amorphous lactose), fluidized bed method, taken from Pearce (2009).

Using the fluid bed rig, Pearce (2009) investigated the stickiness behaviour of a number of specifications of skim milk powders differing in lactose contents, protein content and preheat treatment. It was found that the sticky point curve expressed in terms of temperature versus relative humidity (Figure 2.10) for skim milk powder follows the lactose glass transition curve (predicted from Equation 2.4) very well,

with a constant offset of 24.4 °C. This also compares well with the T-T_g value of 23.3 °C obtained by Hennigs *et al.* (2001) with the propeller driven method. The authors also found that the stickiness of SMP generally increases with higher lactose content, which confirms the role of amorphous lactose in controlling the stickiness behaviour of the powders.

The fluid bed test has the advantage over the propeller driven method because it characterizes the stickiness behaviour of dairy powders in a dynamic air flow condition. However, it has the same limitation of using cohesion rather adhesion as the indicator of stickiness, which may not be directly applicable for predicting particle deposition behaviours. Also, the determination of the endpoint (on-set of stickiness) in this test is subjective and different results may be obtained with different operators of the rig. Chatterjee (2004) also found the test not appropriate for high fat powders which is difficult to fluidize due to significant surface free-fat content that acts as a bridge between particles (Kim *et al.*, 2005).

2.4.3 Cyclone Stickiness Test

Boonyai (2005) developed the cyclone stickiness test for characterising the stickiness behaviour of dairy powders such as skim milk powder. The author reasons that all other existing stickiness test methods do not relate well enough to the actual spray drying practices. In the cyclone stickiness test, test powders would be subjected to the same centrifugal movement and surface impaction as in spray drying and cyclonic collection. Thus this method is considered to yield more realistic results, in terms of the sticky point temperatures obtained. The setup of the method is shown in Figure 2.11.

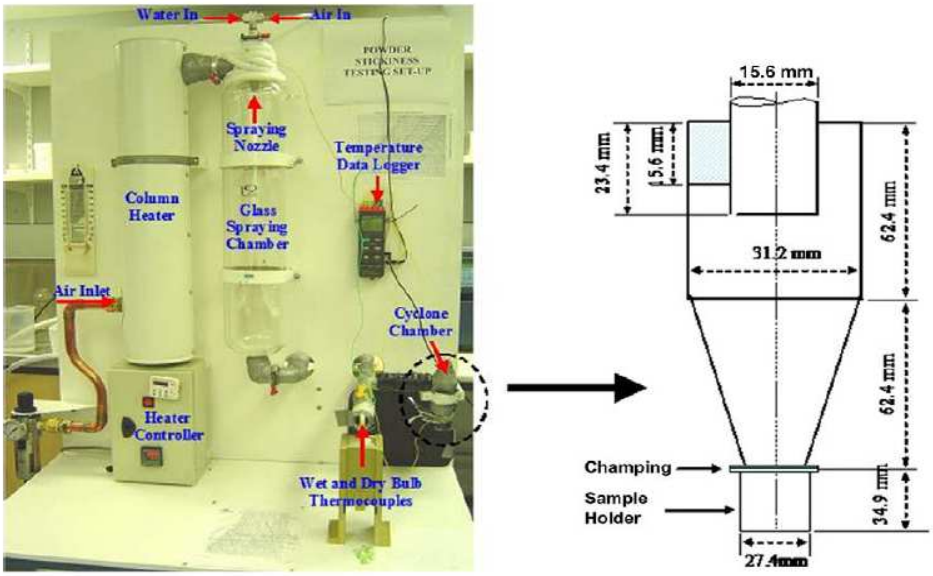

Figure 2.11 Components of the cyclone stickiness test apparatus, taken from Intipunya *et al.* (2009).

The operation of the system involves spraying water at a controlled rate to a stream of preheated hot air. To vary the temperature and humidity, the water feed rate and the inlet air temperature are varied accordingly. The conditioned air is then passed through a small, glass cyclone separator. The system is typically run for 10-15 minutes to stabilise before powder introduction. Usually about 0.1 gram of sample is used for sticky point determination and quickly introduced into the cyclone. If the condition is above the sticky point temperature, powders may become instantaneously sticky or a lag time of up to 10 seconds is required. Below the sticky point, the powders will remain free flowing and no cohesion and adhesion is observed. The endpoint of the test is subjective, similar to that in the fluid bed test. The operator of the rig has to see through the glass cyclone and decide if cohesion and adhesion of the samples are being seen. To obtain the complete sticky point curve, the test can be repeated for dry bulb temperatures up to 90 °C at various levels of RH.

Intipunya *et al.* (2009) modified the rig and made it more compact and easier to control. Testing of skim milk powders has been carried out by both Boonyai (2005)

and Intipunya *et al.* (2009). The resultant stick point curve (Figure 2.12) is found to fit the glass transition curve of skim milk powder with a constant offset of 11.4 °C. The authors attributed the differences in $T\text{-}T_g$ in comparison with results from other methods to the different techniques (air flow, amount of powder etc) used.

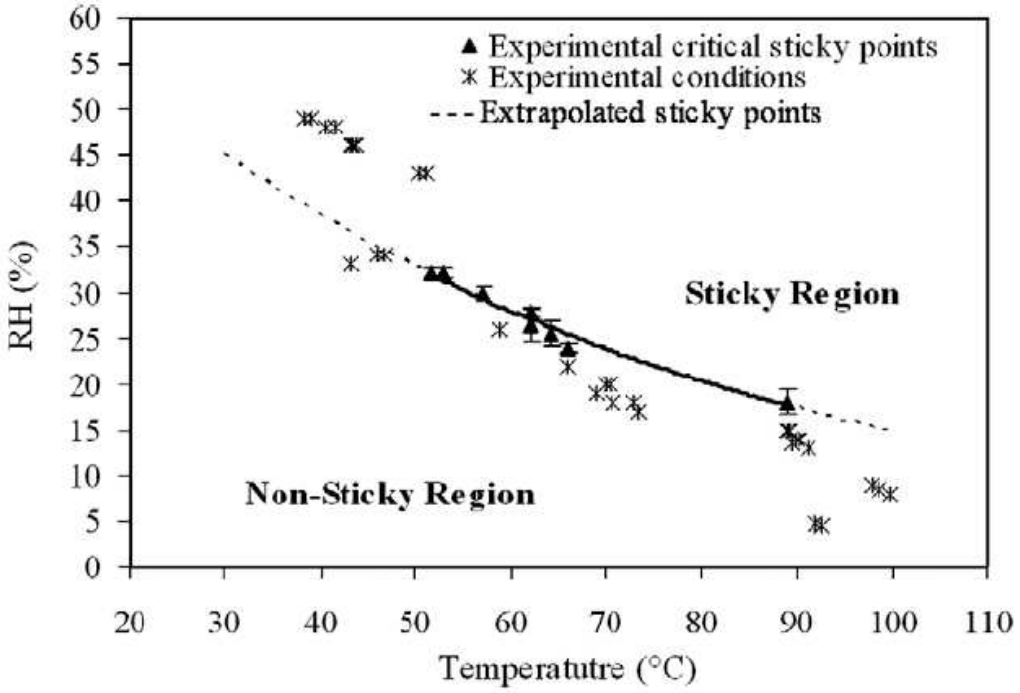

Figure 2.12 Sticky point curve obtained the cyclone stickiness test, obtained from Intipunya *et al.* (2009).

2.4.4 Blow Test

The blow test was developed by Brooks (2000) for quantifying the rate of stickiness development of a powder bed of amorphous lactose (Figure 2.13). It has an advantage over the sticky point tests discussed previously because its result is more quantitative and thus do no rely on the interpretation of the operator. In this test, powder samples pre-conditioned at a specific relative humidity are packed into a segmented distributor plate contained in a glass test chamber. An air stream conditioned at a specific

temperature and RH is passed through a small stainless tube and directed at one segment of the powder bed. The same procedure is repeated at discrete time intervals with different segments in an effort to monitor the development of stickiness. The strength of the powder bed stickiness is indicated by the air flow rate needed to blow a channel through the powder bed. The air flow rate generally increases with the equilibration time of the powders with the conditioned air, thus indicating stickiness development is indeed a time-dependent process.

Figure 2.13 The segmented distributor plate and blow tester, taken from Foster (2005).

Figure 2.14 and 2.15 shows the results of the blow test carried out at around $T\text{-}T_g$ = 10°C and 1°C.

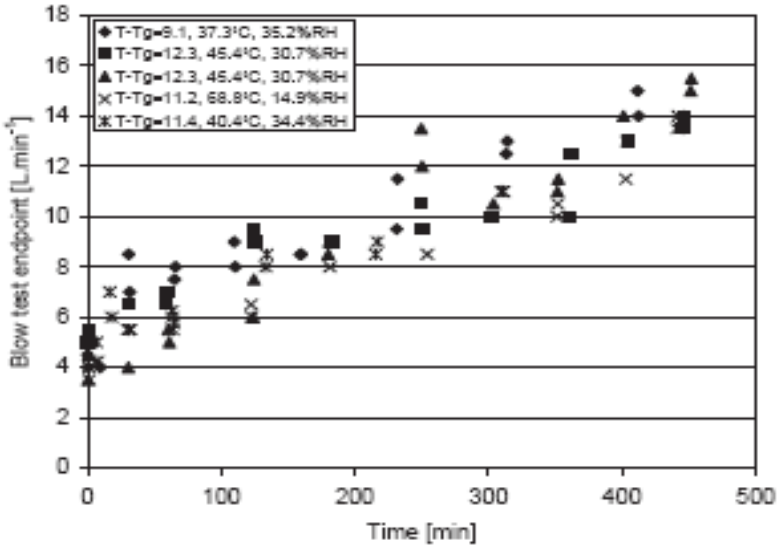

Figure 2.14 Blow test results for amorphous lactose at T-T_g = 10 °C, taken from Paterson *et al.* (2005).

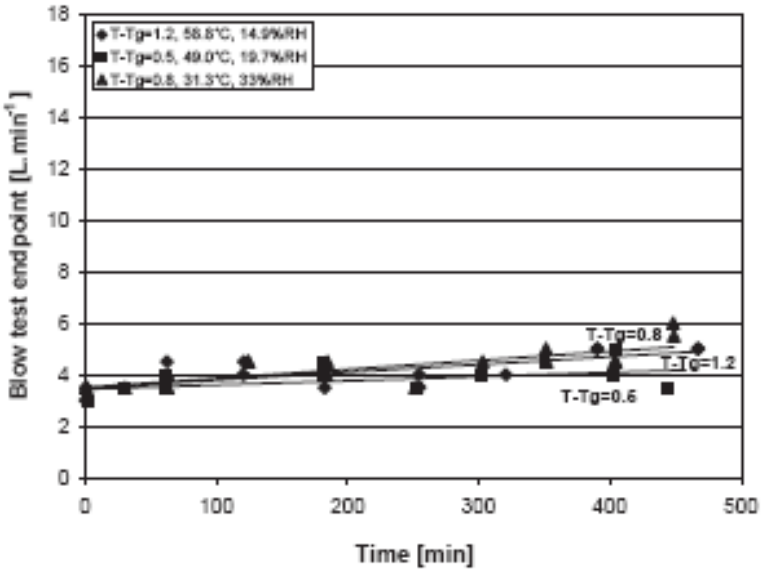

Figure 2.15 Blow test results for amorphous lactose at T-T_g = 1 °C, taken from Paterson *et al.* (2005).

Figure 2.14 shows that despite different combinations of temperature and RH being used to obtain a T-T_g ≈ 10 °C, the rate of stickiness development is similar. This confirms the stickiness development is a time-dependent phenomenon, as indicated by

the higher air flow rate required with increasing storage time. Also, the rate of stickiness development is dependent on the absolute value of the $T\text{-}T_g$, regardless of the specific combination of temperature and RH conditions (Paterson *et al*., 2005). Figure 2.15 shows the rate of stickiness development is much slower at $T\text{-}T_g = 1$ °C compared to Figure 2.14.

The blow test, in comparison with other methods, is quantitative and allows the progression of stickiness development to be monitored. However due to its setup, the results may be more appropriate for serving as a guideline for safe storage of powders. It does not taken into account the fluid dynamics the powders may be subjected to during drying and it also uses cohesion as the sole indicator of powder stickiness.

2.10.3 Particle Gun Test

The particle gun test was developed at Massey University by Crofskey (2000). The humid air supply system consists of a bubble column that is based on the two-pressure principle and is developed by O'Donnell *et al.* (2002). Its operation involves the firing of dairy powders equilibrated with conditioned air at a stainless steel collection plate. The percentage deposition at a specific $T\text{-}T_g$ level is quantified by weighing the deposited mass on the collection plate and dividing it by the original sample mass fed through the system.

The particle gun test is based on the adhesion phenomenon arising from the particle-surface contact dynamics, making it a unique test with clear advantages over other conventional stickiness testing methods like the blow test. Moreover, the particle gun test is more quantitative and allows the development of stickiness above the critical condition to be followed. It is also by far the only test method that studies the adhesion behaviour of sticky food powders. Moreover, the very nature of the test, i.e. the study of collision outcomes of test particles with the collection plate, is the

closest to the actual deposition phenomenon encountered during spray drying among all methods available.

Past works done with the particle gun rig have produced values of stickiness initiation point which are significantly higher than the results from the fluid bed rig (Zuo, 2004). With skim milk powder for example, the average value of 39°C obtained with the particle gun rig is approximately 13°C to 15°C higher than that obtained with the fluid bed rig. This difference has been attributed to the different impact time and force experienced by the particles. However, the application of particle gun result in milk powder plants has been slow because industrial experiences suggested that it is too optimistic. Plant experience indicates that at drying outlet temperature of around 39°C above the corresponding T_g, the drying environment would have been way past the actual stickiness point and the plant certainly would run into problems (Russell, personal communication, 2009). Thus, while the particle gun rig results have highlighted additional factors governing particle stickiness behavior, they seem to grossly overestimate the actual stickiness initiation temperature. The cause of this overestimation is not clearly understood and warrants a thorough investigation. The particle gun test is the method used in this thesis and review of past work done is presented more extensively in Chapter 3.

2.5 CONCLUSIONS

The development of stickiness in amorphous dairy powders, with special attention to amorphous lactose and skim milk powder, has been reviewed. Liquid bridge due to surface tension driven viscous flow is shown to cause this stickiness at conditions at or above the sticky point temperatures. The role of glass transition is found to be correlated closely with the viscosity and molecular mobility of the particles, especially at the surface. In the literature, there is an ongoing effort to develop new

stickiness testing methods that can incorporate the actual spray drying fluid dynamics. The advantages and limitations of various existing test methods have been discussed. Special attention will now be given to the particle gun test method in Chapter 3 and the experimental work done to investigate how air velocity and particle size affect milk powder deposition will be addressed in more details.

CHAPTER 3 - STICKINESS AND DEPOSITION BEHAVIOURS OF SKIM MILK POWDERS WITH THE PARTICLE GUN METHOD

3.1 INTRODUCTION

As discussed in Chapter 2, a number of tests have been developed to study the stickiness development of dairy powders and low molecular-weight sugar droplets. Ideally, the testing conditions should be as close to the actual process, i.e. spray drying, cyclonic separation or duct transport processes, as possible. A number of researchers have in fact studied the deposition propensity of droplets and powders during actual spray drying, often making use of a pilot-scale dryer (Ozmen and Langrish, 2003; Woo *et al*., 2008). However spray drying involves very complex heat and mass transfer between the products and the air stream. The air flow pattern in the spray dryer is also often highly transient (Fletcher *et al.*, 2006). Thus it is difficult to isolate important factors when studying particle deposition, as the temperature, relative humidity and particle trajectories are highly transient and non-uniform in a spray dryer, however small it is.

For these reasons, simpler experiments which focus on specific parameters have been favoured by past researchers (Adhikari *et al.*, 2001; Pearce, 2009). Many stickiness curves implemented in industrial plants in New Zealand and Australia, as well as CFD codes incorporating a particle deposition model, are based on the results from methods discussed in Chapter 2 (Harvie *et al.*, 2002; Pearce, 2009). Laboratory-scale

stickiness tests have been fairly successful in demonstrating the glass transition related stickiness behaviour of dairy powders. More specifically, a stickiness curve specific to the material of interest expressed in T_g + X can be obtained. However, a single stickiness curve is also the limitation of such tests. The use of observed cohesion of the test powders as the end point of the experiments suggest that there exists one and only one critical T- T_g for stickiness to occur. This conclusion is over simplistic in nature and while it serves as a very good general guideline for spray dryer operating condition, it fails to recognize many other potentially important factors.

For particles to deposit on a surface, in addition to its surface stickiness (adhesion), the actual contact mechanics between the particle and the target surface will play a significant role (Busnaina, 1995). The particle gun rig, which is essentially a two-phase impingement jet, is able to simulate the actual collision and deposition between the particles and target surface. It involves the simultaneous conditioning and transport of particles through a long Perspex pipe, followed by particle impacting on a stainless steel plate. The temperature, RH and velocity of the conditioned air can be independently controlled. The deposited particles on the collection plate are easily observable and can be quantified by weighing (Zuo *et al.*, 2007). The particle gun rig is an improved stickiness test rig that more closely represents the actual particle deposition process. It makes possible to study factors which have not been measured previously, e.g. the effect of particle impingement velocity (Chatterjee, 2004).

A typical plot of the particle gun raw data is expressed as percentage deposition against increasing air RH % at constant air temperature (Figure 3.1).

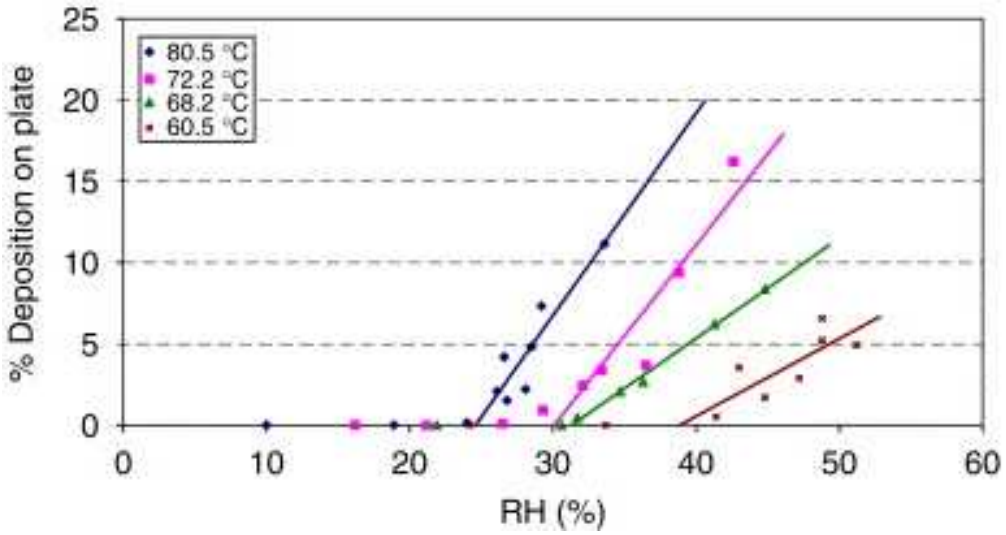

Figure 3.1 Particle gun raw data. The % deposition of WMP A plotted against relative humidity of the exit air at constant temperature (Paterson *et al.*, 2007).

Data show very little deposition as RH is increased at constant temperature until a critical RH is reached, where after deposition increased with increasing levels of RH. A plot of deposition level against T-T_g collapses the data into a single line, as shown in Figure 3.2.

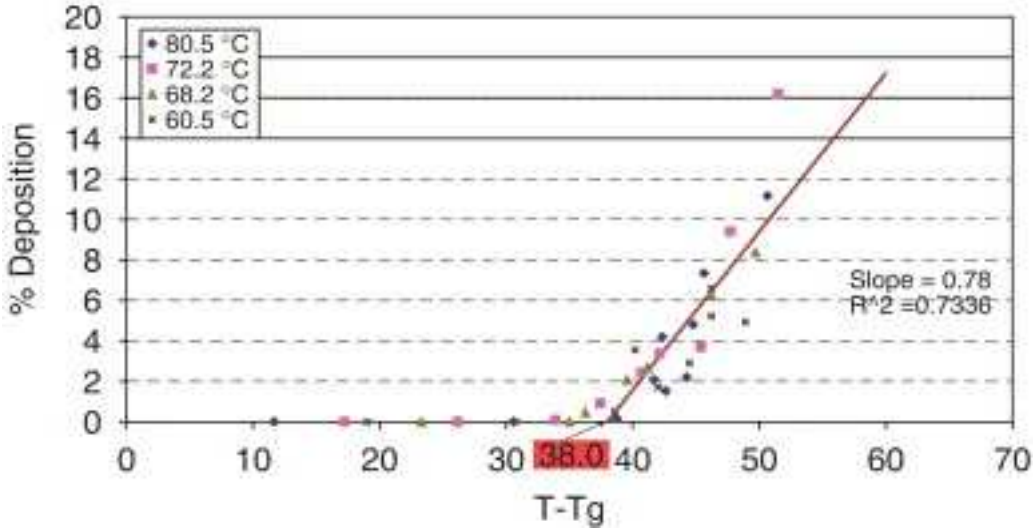

Figure 3.2 The % deposition of WMP A plotted against T-T_g where T_g has be calculated using the relative humidity of the exit air from the particle gun as the surface water activity of the particle. Four different temperature data sets have been plotted (Paterson *et al.*, 2007).

The equation for estimating the T_g for amorphous lactose (Brooks, 2000) has been presented in Chapter 2 in Equation 2.4.The percentage of deposition (% deposition) is obtained by weighing the deposited powders on the collection plate and dividing by the total mass fed into the system. As shown in Figure 3.2, % deposition is seen to increase with increasing $T\text{-}T_g$, indicating the particles are stickier and show a higher deposition propensity when the glass transition temperature is further exceeded.

The result of particle gun test is more objective than that of the fluid bed or cyclone stickiness test, as it is based on the actual quantification of the mass deposited. It also shows that there is a transition from the non-sticky to sticky region of operating conditions. The powders do not become sticky and deposit all at once, but show a gradual and somewhat linear rate of stickiness development with increasing $T\text{-}T_g$.

Past works have been focused on the quantification of the $(T\text{-}T_g)_{critical}$ and slope the deposition curve. The $(T\text{-}T_g)_{critical}$ is obtained by extending the deposition curve to the point where % deposition is zero and it has been described as the “initiation point of stickiness”. This has been often compared to sticky points measured by the fluid bed test and cyclone stickiness test. The slope of the deposition curve has been taken to be an indication of the rate of stickiness development and some works have been done to investigate what affects this rate (Murti, 2006). However, a fundamental problem that has received little attention still exists: at the same level of stickiness ($T\text{-}T_g$), what makes some fractions of the particles sticky and deposit while others do not? This observation suggests that in addition to the effect of temperature and relative humidity, there exist some other factors which may be important in governing the stickiness and deposition behaviours of dairy powders. Controlling these potentially significant factors may present another viable route to controlling the deposition problem encountered industrially.

3.2 MAIN FINDINGS FROM PREVIOUS WORKS ON SKIM MILK POWDER

The particle gun rig has been used to study the stickiness and deposition behaviour of a range of dairy powders (Chatterjee, 2004; Zuo, 2004; Murti 2006). The testing of skim milk powder has received considerably more attention. This is because skim milk powder is one of the main products spray dried regularly in Fonterra and it is known to cause many of the daily operational problems related to deposition. In addition, a lot of fundamental knowledge related to the glass transition of lactose and moisture sorption isotherm of skim milk powder is available in the existing literature, which serves as a good basis for further studying the stickiness development and deposition of skim milk powder.

3.2.1 Lactose and Fat Based Powders

Chatterjee (2004) has used the rig for testing a number of fat-based powders, including nutritional powder, cream powder and snack cheese powder. The significant amount of surface fat on these powders has made it difficult to test them in the conventional fluid bed rig due to the difficulty in fluidization. In addition, amorphous lactose, skim milk powder (SMP) and whole milk powder (WMP) have been tested using the particle gun rig and fluid bed rig, and a comparison of the results was made.

While testing skim milk powder, Chatterjee (2004) has used the dry bulb air temperature ranging from 28 °C to 52°C. In each particular experimental run at a fixed temperature, the relative humidity of the air was successively increased from 40% to 80%. At a particular combination of temperature and relative humidity in all experimental runs, the author has observed a dramatic increase in the amount of

powder deposited on the plate, indicating the initiation of stickiness development for skim milk powder under such conditions. The author then fitted these critical points with "T_g + X" fits with both Cubic and Gordon-Taylor T_g equations for amorphous lactose, and concluded that the Cubic equation (Brooks, 2000) provided a much better fitting of the data. The resultant critical value for $(T-T_g)_{critical}$ was found to be 41.1°C for skim milk powder. In other words, skim milk powder is expected to be non-sticky and should not cause deposition when the operating air condition is below a $T-T_g$ value of 41.1°C. However, this value has far exceeded that obtained with the fluid bed rig, which is 23.2°C for the same type of skim milk powder. This marked difference in $(T-T_g)_{critical}$ has been attributed to the difference in operating air velocity in the particle gun rig (20 - 50 m/s) and fluid bed rig (0.22 – 0.42 m/s). Chatterjee (2004) postulated that as a result of this, the kinetic energy experienced by the test powder in the particle gun rig will be much higher than that in the fluid bed rig, making them less sticky at similar levels of $T-T_g$.

In the opinion of the current author, another difference between the setup of both rigs also contributes significantly to the difference in the results. The particle gun rig involves firing powders through the system at a specific mass flow rate. As a result, the obtained mass of powders collected on the target plate is a result of the interaction between individual particles and the stainless steel surface. In contrast, the fluid bed rig takes the experimental end point as when the powders have developed significant liquid bridges with one another and form a lump. In this sense, the particle gun rig is actually simulating adhesion, when small samples are tested, while the fluid bed rig simulates cohesion.

3.2.2 Plant Exhaust Temperature Particle Gun Studies of SMP

Chatterjee (2004) operated the particle gun rig in the temperature range from 28 °C to 52°C when studying skim milk powder deposition. The exhaust temperature in a typical milk powder plant when spray drying skim milk powder is in the range of 75°C to 90°C. Zuo (2004) realized this discrepancy and repeated some of the experimental works for skim milk powder while using dry bulb temperatures in the range of 60.5°C to 80.5°C.

Results from Zuo (2004) in general agreed with that of Chatterjee (2004). The % deposition was found to be a strong function of the temperature and relative humidity the powders have been exposed to before deposition. At a particular temperature, there exists a critical relative humidity at which the % deposition is observed to increase dramatically. Zuo (2004) transformed the temperature and RH data using Equation 3.1 to obtain the corresponding $T\text{-}T_g$ values and fitted them with the Cubic equation for the glass transition temperature of amorphous lactose. In addition, Zuo (2004) also combined the experimental data from various temperatures into a single $T\text{-}T_g$ plot and fitted them with a linear regression plot. The intercept of the regression line was interpreted as the initiation of stickiness for SMP and the slope of the line was taken as the rate of stickiness development. Zuo (2004) carried out experiments for two types of instant skim milk powders and a medium heat skim milk powder and the results are summarized in Table 3.1.

The values of $(T\text{-}T_g)_{critical}$ obtained with both the cubic equation fitting method and linear regression method agreed with each other very well. These $(T\text{-}T_g)_{critical}$ values range from 37 °C to 41.7 °C, which seems to be in line with the 41.2°C obtained by Chatterjee (2004). The slopes for instant SMP 1 and medium heat SMP are fairly close to each other (3 and 3.3), while the slope for instant SMP 2 is very low in comparison. The instant SMP 2 had a much lower slope because its maximum %

deposition was only about 8% at a T-T_g of 55 °C, whereas the % deposition for instant SMP 1 was well over 40% at a T-T_g of 55 °C. The author has cited the difference in particle size or density as the possible explanation for the discrepancy. However, no particle size distribution has been reported for the tested powders.

Table 3.1 $(T-T_g)_{critical}$ and rate for stickiness development for skim milk powders tested by Zuo (2004).

Skim Milk Powders	Fat (TS%)	Lactose (TS%)	Protein (TS%)	Critical "X" Cubic Equation	Slope	Critical "X" Regression Line
Instant SMP 1	0.62	57.84	34.27	37.9	3.04	37.3
Instant SMP 1 (Replicate)	0.62	57.84	34.27	40.9	2.95	41.7
Instant SMP 2	0.79	52.98	38.19	39.7	0.34	38.1
Medium Heat SMP	0.83	53.01	38.05	40.2	3.3	40.3
Chatterjee (2004) SMP	0.8	57.56	34.63	N/A	N/A	41.2

3.2.3 Experimental Parameters Affecting Particle Gun Study Results

It is of value to understand whether the stickiness initiation point and slope of the % deposition curve is any different for a range of contact velocities, impingement angles, ambient air RH and particle sizes. This is because spray dried powders are likely to encounter a wide range of carrier phase velocities, impingement conditions, RH values and particle sizes, and any one type of experimental protocol is unlikely to be representative of all possible scenarios.

Zuo (2004) has shown that the stickiness initiation point and slope of the % deposition curve are two useful parameters for characterizing the stickiness development of lactose-based dairy powders such as skim milk powder. The particle gun rig has been shown to be fairly successful in measuring these two parameters, although there seems to be a certain degree of variability in the results obtained. Past workers on the subject before Murti (2006) carried out experiments at 20 - 50 m/s air velocity.

Murti (2006) has undertaken an extensive set of experiments, using only skim milk powder, to investigate what affects the reproducibility of the particle gun test under testing conditions. Using the $(T\text{-}T_g)_{critical}$ and the slope of the % deposition curve as the two response variables, Murti (2006) evaluated contributions from a range of factors including the ambient air RH, powder initial water activity/moisture content, powder feed rate, air velocity, impingement angle and collection plate material. Particle size is also likely to be a factor but it has not been studied.

3.2.3.1 Factors affecting $(T\text{-}T_g)_{critical}$

Among the factors investigated, Murti (2006) found that ambient air RH in the room of the test rig is significant in affecting the onset of stickiness for skim milk powder. Under standard testing conditions room ambient air RH was varied from 40% to 70% and results from this work are presented in Figure 3.3. It is shown that the $(T\text{-}T_g)_{critical}$ is very sensitive to change in ambient air RH, and there is a difference of around 20°C between the tests done at the lowest and highest RH. Moreover, skim milk powder is shown to be stickier (lower $(T\text{-}T_g)_{critical}$) if it has been in contact with ambient air of higher RH.

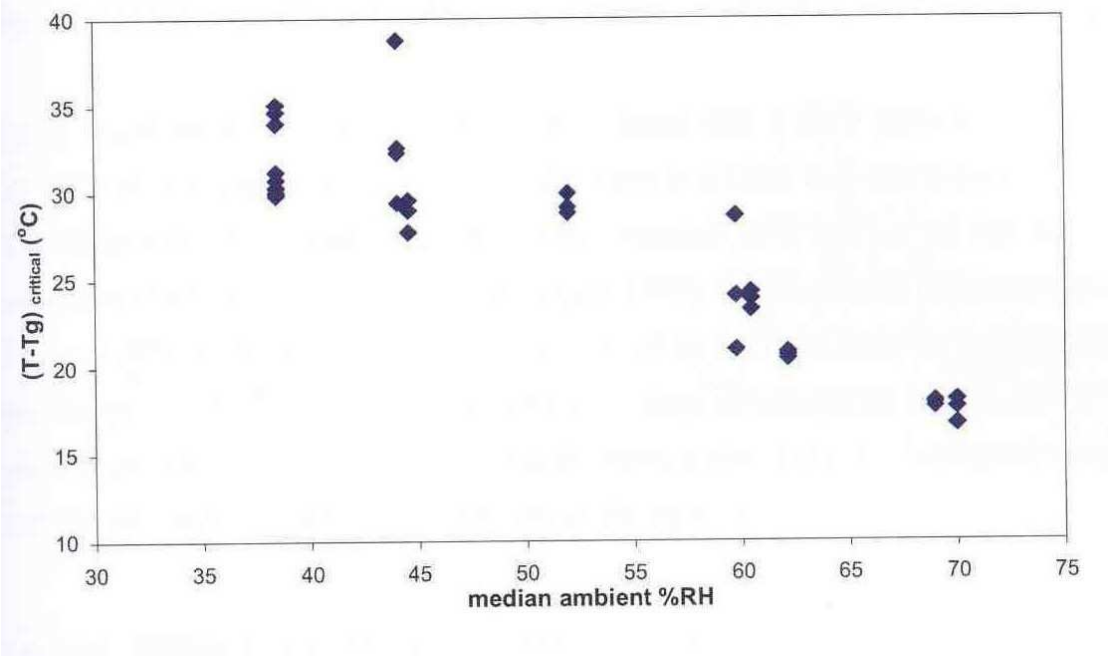

Figure 3.3 Effect of ambient air RH on $(T-T_g)_{critical}$, adapted from Murti (2006).

Murti (2006) has suggested that the previous assumption that particle surface stickiness is entirely responsible for the observed deposition may not be valid. A sample calculation based on a particle size of 83 μm and moisture diffusivity of 2.33×10^{-14} m/s has shown that only 0.17 - 0.28% of the particle volume is affected by the air conditions in the particle gun whereas 5.8 – 16.75% of the particle volume would be conditioned by the ambient air RH, depending on the length of time the powders are in contact with the ambient air before entering the system.

3.2.3.2 Factors affecting the slope of % deposition versus $T-T_g$ curve

Murti (2006) also found that the slope of % deposition versus $T-T_g$ curve is very sensitive to the initial powder water activity (a_w) but not significantly affected by the ambient air RH. Figure 3.4 shows the results in support of this finding.

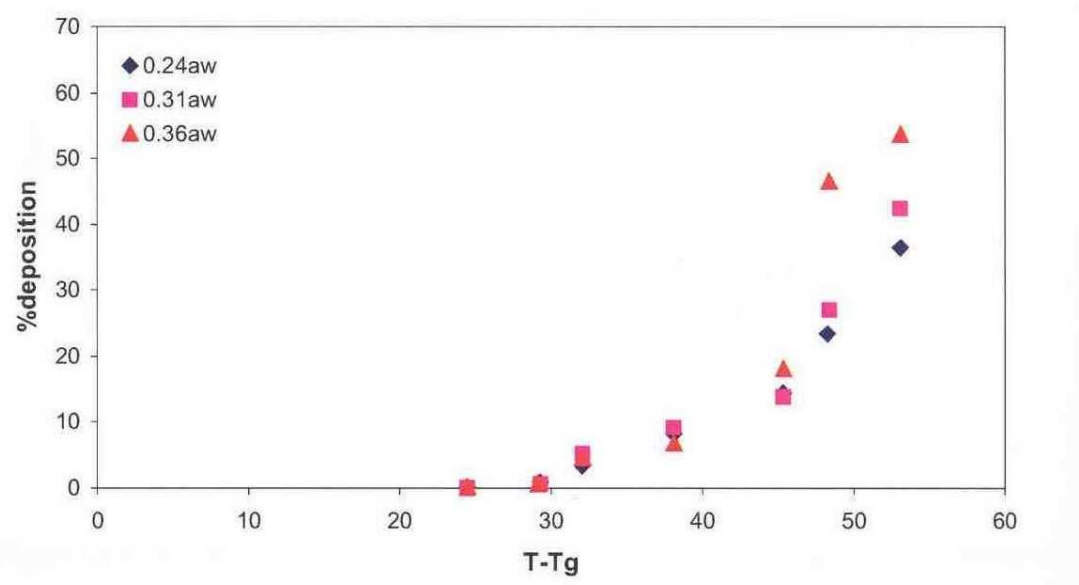

Figure 3.4 Effect of initial powder water activity on the slope of the deposition curve, adapted from Murti (2006).

Murti (2006) has carried out the experiments with skim milk powders at water activity level of 0.24, 0.31 and 0.36 while keeping all other conditions the same. It is shown in Figure 3.4 that % deposition starts to increase from zero at similar level of $T\text{-}T_g$. The % deposition for the three experimental runs remains more or less the same up to a $T\text{-}T_g$ of 40°C, and then powders with a higher initial a_w starts to show a higher rate of development of % deposition.

Murti (2006) has attributed the increases rate of stickiness development for powders of higher initial a_w to the fact that powders with higher moisture content would be softer and more plastic in nature. This would have resulted in greater plastic deformation of the particle surface and increases in surface area for adhesion to develop upon impact.

3.2.3.3 Effect of air velocity and distance between gun exit and collection plate

The difference in air velocity has been cited as the single most important reason for the large discrepancy in the sticky point curves obtained with the particle gun rig and fluid bed rig (Chatterjee, 2004; Zuo, 2004). For particles in the micrometer range such as skim milk powders, the carrier phase velocity will directly influence their velocity distributions and kinetic energy upon impact due to their small particle response times. The fact that the slope of the deposition curve is sensitive to powder initial water activity indicates that in addition to surface stickiness, the mechanical property of the particles also play a significant role in deciding the fate of impinging particles.

As a departure from the standard operating condition, Murti (2006) reports to have varied the air velocity at particle gun exit from 10 to 30 m/s. The resultant $(T\text{-}T_g)_{critical}$ was found to be highly dependent on the velocity condition, increasing from 32°C at 10 m/s to 38°C at 30 m/s. In addition, the rate of stickiness development was found to be higher at lower air velocity. Murti (2006) concluded that in addition to the viscous flow at the particle surface as previously thought, viscoelastic deformation may be a more important factor in controlling the particle deposition behaviour. The author cited the work of Palzer (2005), who has postulated that the $(T\text{-}T_g)_{critical}$ observed experimentally is an inverse function of the contact time between the particles and deposition target.

Murti (2006) has also investigated the effect of distance between the gun tip and the collection plate on the resultant % deposition. It was found that at normal impingement (90° angle of impact), increasing the distance would lead to high amount of deposition. However, at 29° angle of impact, the trend was reversed. The author has not given any reason for these observations and for reproducibility of the results, all standard tests were carried at a distance of 160 mm.

3.2.4 Summary and discussions of previous works

All of the previous works have shown that the particle gun rig offers an alternative testing method for studying the stickiness behaviour of dairy powders. In addition to the sticky point curve that can be obtained with other conventional test rigs, the particle gun rig has the extended capability of measuring the rate of stickiness development. In contrast to the conclusions drawn by Chatterjee (2004) and Zuo (2004), Murti (2006) has shown that deposition is not solely influenced by the surface conditions of the impinging particles. On one hand, this finding has made the industrial application of particle gun rig results complicated; on the other hand, it indicates that there exist other controllable factors available to the industry to deal with the particle deposition problems. A closer examination of the additional factors uncovered by Murti (2006) indicates that they are all related to the kinetic energy of the impinging particles and energy dissipation mechanisms. An energy balance constructed on a single impinging particle can be described as

$$E_r = E_i - (E_{ad} + E_{pd}) \qquad (3.1)$$

Where

E_i : incoming kinetic energy of the particle (J)

E_{ad} : kinetic energy lost due to surface adhesion (J)

E_{pd} : kinetic energy lost due to plastic deformation (J)

E_r : available kinetic energy for particle rebound (J)

Equation 3.1 can be expanded to include additional terms such as the kinetic energy loss due to frictional forces and rotational forces. For simplicity, only the most dominant contributors have been included. The incoming kinetic energy of the particles, E_i, can be expressed as

$$E_i = \frac{1}{2} m V^2 \qquad (3.2)$$

Equation 3.2 shows that the kinetic energy of the impinging particles is directly influenced by the velocity and mass of the particles. While Murti (2006) has found the velocity to be an important factor, she has not investigated the effect of particle size on the results of the particle gun rig. An important yet still unanswered question relates to the observation of the "% deposition" itself. In a single experimental run, if all variables are held constant, there still exists a distribution of sticking propensity among the test powders. It is known that the particle size distribution encountered industrially is far from uniform, and it is highly possible that the particle sticking propensity is size dependent.

The test velocities reported by Chatterjee (2004), Zuo (2004) and Murti (2006) for standard tests are 20 m/s. Unfortunately Zuo (2004) and Murti (2006) give no indication of the instrument and method used to measure the velocity at the gun tip. Chatterjee (2004) states the velocity average was obtained using an anemometer at the gun tip. However the diameter of the anemometer is not given, nor is the distance from the tube end. He later contradicts himself by saying that to get 20 m/s average velocity the average flow rate through the particle gun tube obtained from reading a rotameter with appropriate temperature and pressure corrections, is 150 LPM. Since the particle gun tube is 8 mm diameter this flow rate corresponds to an average gun tip velocity of 49.7 m/s. This discrepancy is likely to be caused by the anemometer averaging the air velocity over an area greater than the tube diameter. Zuo (2004) and Murti (2006) may have made similar velocity measurement errors considering all three researchers performed the work at the same University around the same time. The average velocities recorded by these researchers may actually be 2.5 times higher than those reported, especially since velocity was initially not considered to be a highly significant effect. Repeating work at different velocities is, therefore, an area of

interest and worth.

Both the ambient air RH and powder initial water activity are related to the moisture content and softness of the particles. While the exact function is unknown for skim milk powder, it is known that a wetter particle will be more plastic in nature and tends to dissipate more kinetic energy than drier particles. Their relevance may be described by the plastic deformation term, E_{pd} , in Equation 3.1.

It will be useful if one can quantify the exact contributions from each of the variables and come up with a general relationship describing the sticking propensity of skim milk powders. Such a relationship will not be confined to any particular set of experimental conditions but will have some universal properties which could be applied given any conditions.

3.3 EXPERIMENTAL METHODS AND MATERIALS

3.3.1 Particle Gun Setup

The particle gun test rig developed by Dr Tony Paterson from Massey University in conjunction with Fonterra Research Centre (Chatterjee, 2004) was used in this thesis. Figure 3.5 shows the schematic diagram of the rig, taken from Zuo (2004).

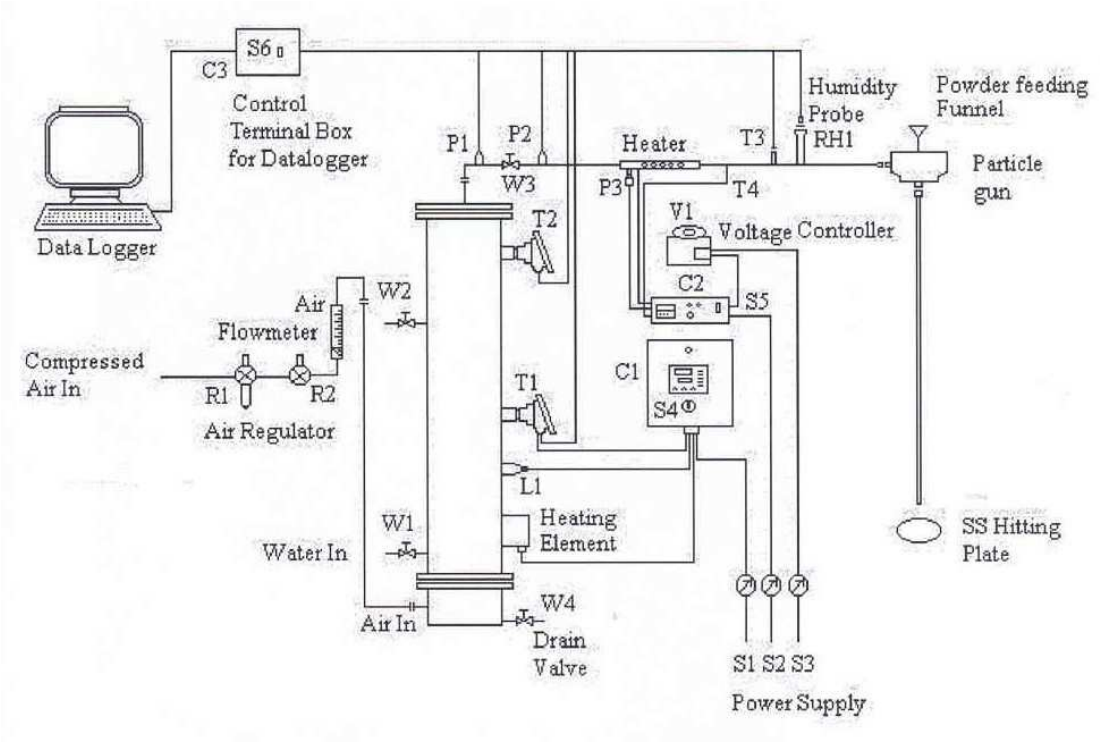

Figure 3.5 Schematic diagram of the particle gun rig, adapted from Zuo (2004).

Similar to other stickiness testing rigs, the particle gun has the same essential feature of being able to produce air stream of controllable temperature and humidity content. Laboratory compressed air enters the system through two pressure regulators. The first regulator, R1, has a similar function to a receiver tank, i.e. to even out the

pressure fluctuations in the compressed air from the main. The second pressure regulator, R2, is used to adjust the system pressure in the bubble column. After passing through the two pressure regulators, compressed air enters the bubble column at the bottom and flows upwards. The stainless steel bubble column is fitted with two valves to regulate the water level. Valve 1 (W1) at the bottom is connected to the water main in the laboratory while valve 2 (W2) acts as an overflow valve. When being filled up, both valves are opened, and the water supply is cut off when water starts to flow out from valve 2. Moisture-laden compressed air then passes through a third pressure regulator (W3), and its pressure is turned down to the final value to give the desired air flow rate and relative humidity in the system downstream.

The principle of achieving a specific RH by varying the pressure ratio before and after the pressure regulator has been described in detail by O'Donnell *et al.* (2002). Relative humidity can be defined as ratio of the partial pressure of water vapor in the mixture to the saturated vapor pressure of water at a same temperature.

$$RH = \frac{P_{vap}}{P_{sat}} \times 100\% \tag{3.3}$$

Before going through the expansion valve, the compressed air is assumed to be saturated at whatever pressure it has been conditioned at in the bubble column. The total pressure of the compressed is reduced after the expansion valve, which also reduces the vapour pressure of the water according to Dalton's Law of Partial Pressure.

$$P_{total} = P_{air} + P_{vap} \tag{3.4}$$

However, saturation pressure of the air is unchanged, since it is only a function of temperature. Thus the net effect of pressure turndown, according to Equation 3.3, is to

reduce the water vapour pressure and thus relative humidity of the air. The resultant relative humidity can be predicted from the pressure ratio (Equation 3.5). In practice, the exact RH is more precisely determined by the measuring the actual value with the humidity sensor inside the rig.

$$RH = \frac{P_{total,after}}{P_{tottal,before}} \times 100\% \qquad (3.5)$$

A 400 W inline air heater is located after valve 3, to raise the dry bulb temperature of the air. After the air has been conditioned to the required temperature, humidity and flow rate, it goes through a Venturi feeder. The Venturi feeder essentially accelerates the airflow by partially restricting the cross-sectional area of the flow passage. The increase in the velocity pressure of the flow contributes to a slight lowering in its static pressure, relative to the ambient pressure. Skim milk powder is fed into the system through a nylon funnel. The venturi powder feeder has been designed in such a way that the milk powders almost enter the system by gravitational settling and not by strong vacuum suction. This has the benefit that the conditioned air retains whatever temperature and humidity it has been conditioned upstream. During the setup of the rig it was realized that too strong a suction will introduce strong secondary flow into the system, which made the rig extremely difficult to operate.

In the original setup of the rig, the conditioned air makes a 90 degree turn and the particle-laden flow was directed downwards through a 108 mm Perspex pipe. A stainless steel disc of 75 mm in diameter was placed at 160 mm below the pipe exit and acts as the deposition target. It has been decided to change the orientation of the particle-laden flow to a horizontal one. Skim milk powders are relatively large compared to submicron particles and it is expected that gravity will have some influence on their deposition behaviour. It is hoped that the horizontal orientation of the rig will eliminate the contribution to deposition from gravity. In addition to the change in the rig orientation, the deposition target also has been changed from a round

75mm diameter disc to a rectangular stainless steel plate (164 mm × 136 mm). Very interesting deposition morphologies have been observed as a result of this change, which will be discussed later in this chapter and more extensively in Chapter 5. Figure 3.6 shows the setup of the current particle gun rig.

Figure 3.6 Picture of particle gun rig and Perspex pipe.

The water temperature in the bubble column and air temperature are controlled by heating elements separately controlled by two Shinko GC3000 temperature controllers. Table 3.2 shows the complete instrumentation and control of the particle gun rig. Pressure of compressed air before and after turn-down at W3 is measured by two pressure gauges. Relative humidity of the air is measured by a Vaisala HMT 330 humidity sensor. All temperature measurements are made by Pt100 type sensors. An Opto22 data logger connected to a PC simultaneously logs and displays all variables of interest during the experiment. The velocity and temperature of the conditioned air are also measured at the exit of the pipe, as recommended in previous works (Murti, 2006). Air velocity is measured with a Kestrel 3000 vane anemometer, which has a

25 mm impeller (Nieslsen-Kellerman, USA). The average anemometer velocity is corrected with the aid of Particle Image Velocimetry (PIV) analysis of the particle gun. A linear correction factor of 2.3 has been applied to the average anemometer reading to better represent actual average velocity at the gun tip. More detailed information regarding the operation of the rig can be found in previous works by Chatterjee (2004), Zuo (2004) and Murti (2006).

Table 3.2 Control and measurement points in the particle gun rig.

Abbreviation	Description	Type of Sensor	Measurement Output
R1	Pressure Regulator	Manual Control	-
R2	Pressure Regulator	Manual Control	-
W1	Water Inlet	Manual Control	-
W2	Water Overflow	Manual Control	-
L1	Water Level Sensor	Feedback to Shinko 1	Directly Read by Shinko 1
T1	Water Temperature	Feedback to Shinko 1	Directly Read by Shinko 1
T2	Air Temperature	Measurement	4-20mA/0-100 DegC
P1	Pressure Gauge	Measurement	4-20mA/0-10 Bar gauge
W3	Pressure Regulator	Manual Control	-
P2	Pressure Gauge	Measurement	4-20mA/0-10 Bar gauge
P3	Pressure Gauge	Feedback to Shinko 2	Directly Read by Shinko 2
T3	Air Temperature	Measurement	4-20mA/0-100 DegC
T4	Air Temperature	Feedback to Shinko 2	Type K, Directly Read by Shinko 1
RH1	Relative Humidity Sensor	Measurement	4-20 mA/ 0-100 %RH

The measurement accuracy of the temperature sensors are given by the manufacturer to be within ± 0.5 °C. The Vaisala humidity sensor is calibrated at Fonterra Te Rapa and is accurate to within ± 0.1 % RH. The Kestrel 3000 vane anemometer is calibrated in a subsonic wind tunnel by the manufacturer and has a maximum uncertainty of ±0.6% within the air speed range of 3 – 40 m/s.

The air velocity covered in the experiments is 10.3 m/s, 14.8 m/s, 19.4 m/s and 45.6

m/s respectively (or 4.5 m/s, 6.5 m/s, 8.5 m/s and 20 m/s measured using the anemometer), in line with the recommendation to use velocity below 20 m/s by Murti (2006). The distance from the Perspex pipe exit to the plate, H, is maintained at 44 mm. This gave a H/D ratio of 4, with a pipe diameter D of 11 mm. The temperature at the gun exit is maintained within the range of 73 – 80 °C. This is achieved with the inline air heater set about 105 °C and in general the exit temperature tends to increase for a higher air velocity. The plate temperature is also measured using a K-thermocouple and the temperature ranged from 45 ^{o}C at the centre to 30 ^{o}C at the periphery of the plate. In all experiments, even at high RH, condensation did not arise on the plate.

No attempts have been made to vary the initial powder activity of the skim milk powders. The test powders have a typical a_w of 0.15 at a room temperature of 18 °C. This is measured by inserting the Vaisala humidity sensor into a sealed bottle of skim milk powders, as recommended by Murti (2006). A typical equilibration time of one hour is used.

3.3.2 Particle Sieving and Size Measurement

Particle sieving is carried out using Endecotts brass sieves (Endecotts, UK) and a mechanical sieve shaker. The skim milk powder used in this study is non-agglomerated and tends to clump together and thus not easily separated. As recommended by GEA Niro Method No. A 8 a, about 2% of the free flowing agent is mixed well with the powder before sieving. Two particular sieve fractions of the powders are used for the experiment: d_p< 45 μm and 45 μm < d_p < 63μm. It is common knowledge the particle size distribution encountered in the exhaust ducts of the spray is generally much smaller than the bulk particle size. A standard sieving time of 5 minutes is adopted for all trials. To prevent moisture uptake of the powders

during sieving, a compressed air gun is used to create a relatively dry environment around the sieves.

The two fine fractions are thus chosen in an effort to better represent the stickiness behaviours of the smaller particles. Due to time constraints, the actual particle size distribution from Fonterra exhaust ducts has not been obtained and this can be a focus of future studies. The sieved particles are analysed with a Malvern Mastersizer 2000 and a wet dispersion unit. The dispersion agent used is reagent grade isopropyl alcohol as recommended by Písecký (1997). Figure 3.7 shows the particle size distribution for the three fractions of test powders used in this study and Tables 3.3 summarises their averaged sizes for easy comparison.

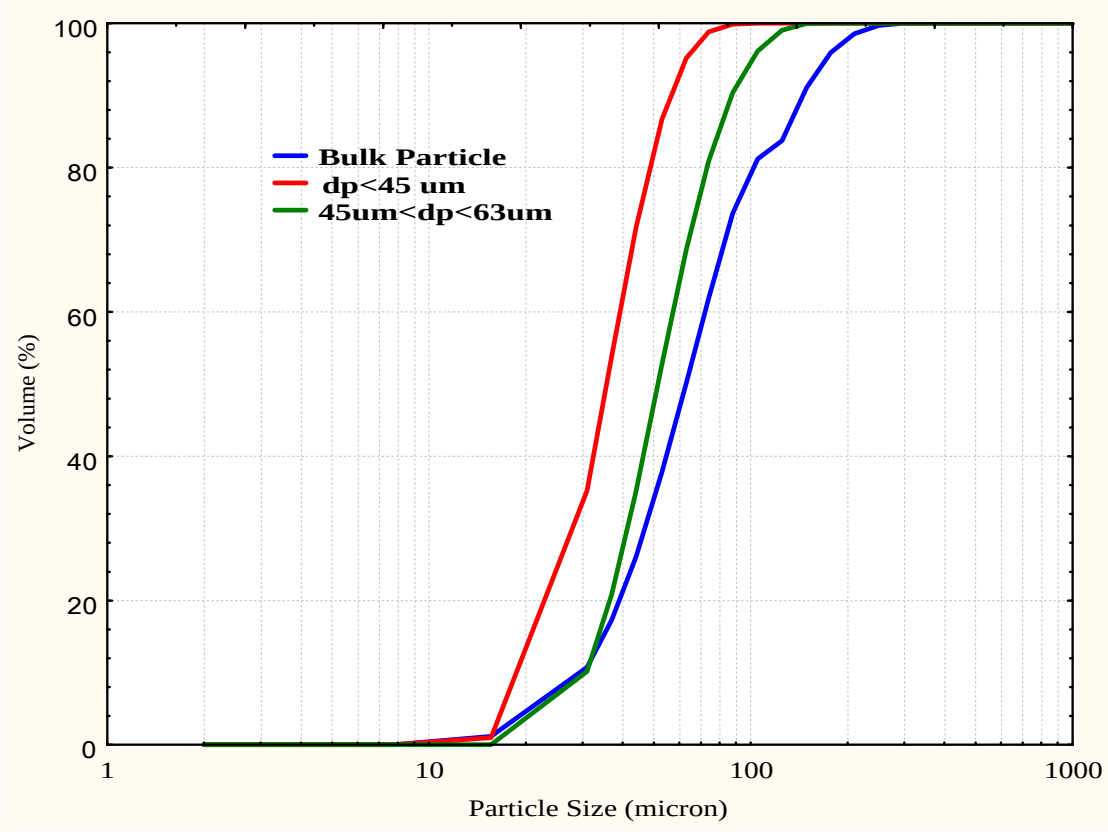

Figure 3.7 Particle size distributions for skim powders used in the particle gun study.

Table 3.3 Average particles of skim milk powder in different size fractions.

Skim Milk Powder Fraction	d (0.1)	d (0.5)	d (0.9)
d_p< 45 μm	18 μm	30 μm	57 μm
45 μm < d_p <63 μm	31 μm	51 μm	87 μm
Bulk	32 μm	61 μm	140 μm

The nominal mesh sizes of 45 μm and 63 μm provide the smallest aperture sizes that particles can pass through. In practice, milk powders are not exactly spherical and there are variations among their width, length and height. As a result, particles having average diameters greater than the mesh size but with a smaller size in one particular dimension are still able to pass through the holes in the sieve. On the other hand, due to the sticky and cohesive nature of skim milk powders, sometimes smaller particles adhering to large primary particles are not separated and will remain in the un-sieved fractions. Figure 3.7 and Table 3.3 show that the sieving protocols have been fairly successful, with the resultant finer fractions significantly smaller than the bulk particle size distribution. There is a degree of overlapping in the size distributions of the two finer fractions, but the differences in the average particle sizes achieved are sufficient for evaluation of the size dependency in particle deposition.

3.3.3 Particle Feeding

Murti (2006) has improved the particle feeding method in the particle gun rig by placing a mechanical vibratory feeder above the funnel connected to the rig. Different feed rates could be achieved by placing a second funnel above the vibratory feeder and varying the depth of insertion of this funnel into the feeder. Murti (2006) has also set up a plastic enclosure around the vibratory feeder and funnel. This allows the independent control of the RH the test powders are in contact with, which would have a significant effect on the particle gun results.

A mechanical vibratory feeder is also available for use in this study. While the device is capable of feeding the particles at a constant rate similar to that used by Murti (2006), i.e. 0.3-0.6 g/s, it is found that this range of feed rate is too high for the current setup. This is mainly due to the lower velocity range employed in this study, and the particles are not conveyed efficiently at high feedrates and sometimes extensive agglomeration of the particles inside the particle gun is observed. To overcome this problem, an alternative feeding method is used.

Figure 3.8 Glass bottle used for storage and feeding of test powders.

Figure 3.8 shows the glass bottle used for the storage of the test powders before the experiment. A 3 mm hole is drilled into the lid of the bottle, which allows the passage of the test powders. The bottle is simply inverted during the experiment and the powders are fed into the funnel of the venturi feeder by gentle tapping. The feed rate achieved this way averages about 0.05 g/s and the resultant conveying of the powders is much more efficient. It is realized that the variation in feed rate by manual feeding is likely to be higher than that of the vibratory feeder. However Murti (2006) has found no significant effects of the feed rate on the particle gun results and manual feeding has also been used by previous operators of the particle gun rig. Another advantage of this method is that the powders are not exposed to the ambient air RH

before entering the system. The water activity has been tested for the powders in the bottle before and after the experiment, and there is no evidence of moisture uptake. The amount of powders fed into the system is standardized at 3 g for all experiments.

3.3.4 Experimental Protocol

A step by step experimental procedure for the operation of the particle rig developed by Chatterjee (2004) was followed. A brief summary of the method used is:

- The external power source to the data logger, computer, water heater and air heater and all measuring instruments was turned on.
- The Variac connected to the air heater was set to at or below 100 V.
- The Opto 22 data logger icon -> I/O Boxes -> Auto Detect was clicked on.
- This enabled importation of the corresponding driver file for the particle gun rig -> Operate -> Start Scanning
- The compressed air was then turned on and the pressure at R1 was set to 3 Bar. To change the pressure of the system, R2 was used.
- The water temperature in the bubble column was set to 75 °C through the Shinko controller.
- The temperature of the air heater was initially set to 80 °C and at the same time the gun exit velocity was measured with the vane anemometer. W3 was used to adjust the velocity at the gun exit.
- Once the desired velocity at the gun exit was achieved, the gun exit temperature was measured with a Pt100 sensor. The air heater temperature was adjusted until the desired gun exit temperature was reached.
- The RH of the air was adjusted by regulating the pressure through R2. R2 can be operated without affecting W3 and the already fixed velocity.
- The experiments were started once the temperature and RH reached steady state.

Valve labels (R1, R2 and W3) correspond to Figure 3.5.

3.4 RESULTS AND DISCUSSIONS

3.4.1 Deposit Morphology

A common and interesting feature of all experiments is the morphology of the powder deposits formed on the stainless steel collection plate. Shown in Figure 3.9 are photographs of the typical morphology observed from a set of experimental tests for skim milk powder (SMP) at constant air velocity and particle size. The corresponding $T\text{-}T_g$ versus % deposition data are presented in Figure 3.10. Additional morphology photographs for other conditions are presented in Appendix 1.

The % deposition on the collection plate is typically a linear, increasing function of $T\text{-}T_g$, with all other experimental variables held constant (Figure 3.10). At non-sticky conditions, the plate remains very clean after an experimental run. In this case, most of the powders would have rebounded after collision. At a critical condition of $T\text{-}T_g$, some powder deposits start to show up at the periphery of the collection plate with a large round clear zone (plate a). This also roughly corresponds to the $(T\text{-}T_g)_{critical}$ on the deposition curve, where the % deposition is observed to start increasing from zero. With increasing $T\text{-}T_g$, more powder deposits are formed on the plate and the centre round clear zone gets gradually smaller (plates b & c). The disappearance of the centre ring is preceded by the formation of a striped deposit ring, which starts to grow both inwards and outwards (plate d). The intensification of the deposit structure towards the centre of the plate at elevated $T\text{-}T_g$ is accompanied by the decline in deposition at the periphery. At extremely sticky conditions, skim milk powders are seen to deposit at the very centre of the collection plate (plate e & f), with the diameter of the morphology corresponding to that of the particle gun rig Perspex pipe.

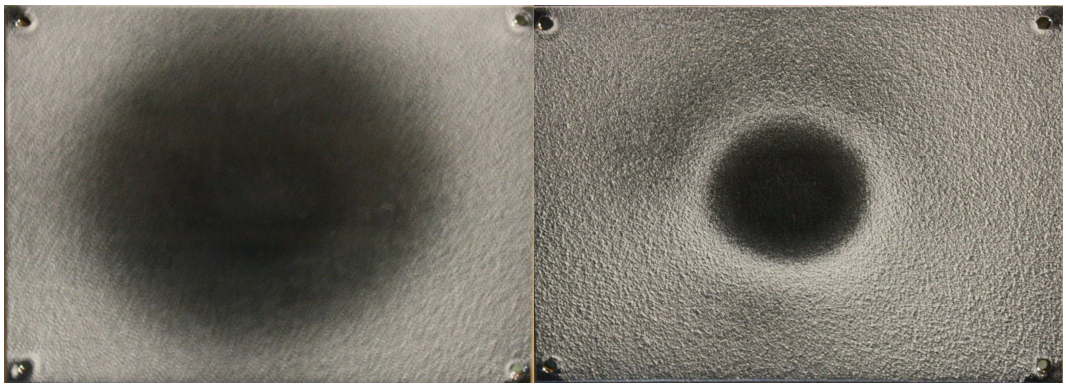

(a) T-Tg = 17.0^{o}C, Dep % = 6.4 (b) T-Tg = 25.1^{o}C, Dep % = 14.3

(c) T-Tg = 31.9^{o}C, Dep % = 32.1 (d) T-Tg = 37.6^{o}C, Dep % = 34.1

(e) T-Tg > 45^{o}C, Dep % = not measured (f) T-Tg > 50^{o}C, Dep % = not measured

Figure 3.9 Deposit morphology for SMP, shown in increasing order of T-T_g, air jet 90^{o} to plate, jet air velocity 10.3 m/s and particle size 45μm<d_p<63μm.

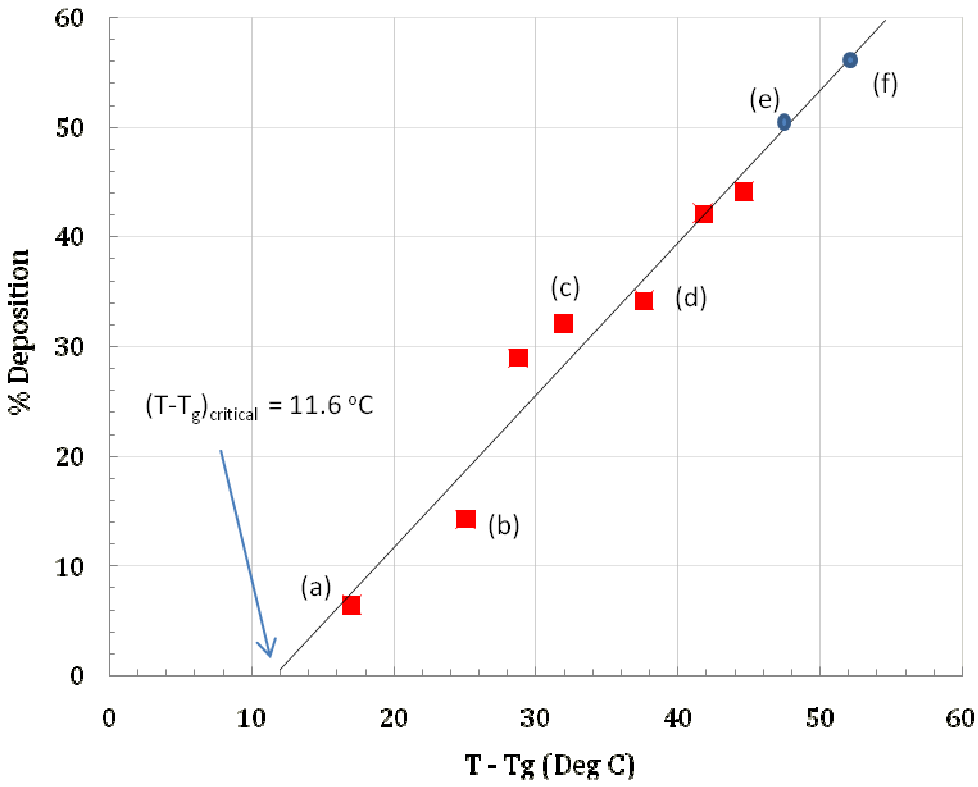

Figure 3.10 Effect of air RH (expressed as T-T_g) on % deposition SMP for air jet 90^o to plate, air velocity 10.3 m/s and particle size 45µm<d_p<63µm. Data points for (e) and (f) are estimates.

Understanding how these series of deposit morphology have been formed will help to understand some of the underlying mechanisms the particle gun rig simulates and also indicate how the subsequent results should be analysed. The powders will exit the gun tip with sufficient inertia so that they are able to traverse the boundary layer wall jet close to the target plate. In doing so, their momentum will be slightly affected, as the normal velocity distribution will start to change in the radial direction. However, considering the close spacing between the gun tip (Perspex pipe end) and the stainless steel collection plate (44 mm), the impingement jet would have expanded only slightly and the radial dispersions of the particles would be minimal. Particles in their flight towards the collection plate would have mostly stayed in their original paths and the most probable zone of first collision would be relatively small compared to

the size of the plate. To investigate this further Computational Fluid Dynamics (CFD) has been used to model particle deposition in an impingement jet and the results of this study are presented in Chapter 5.

In the past, researchers have interpreted results from the particle gun rig in a manner as if the % deposition measured is the result of a single collision event between the particle and the target plate. In this sense, individual particles have been thought to only collide with the target surface once and depending on their stickiness conditions, they either deposit or rebound from the surface. The location of the deposits as seen on the photographs, especially for those with less sticky conditions, indicate that the particles would impinge at the centre of the plate and then travel considerable distances radially. These final deposit structures are thus the net results of a combination of secondary, tertiary and even higher number of particle-surface collisions of varying velocity and angle of impact. The effect of the conditions previously reported of, say, air velocity of 10.3 m/s and normal impingement angle, would only hold true for the first collision event. Having said that, their effects on subsequent events are not removed.

While researchers from Massey University have not reported observations of the deposit morphology, it is expected they would have come across similar findings. Past investigations with the particle gun rig have used a round target disc of 75 mm in diameter. It is expected the larger rectangular collection plate (164 mm ×136 mm) used in this study will lead to slightly different results with regard to the onset of stickiness initiation ($(T\text{-}T_g)_{critical}$) and slope of the deposition curve. In light of the current improved understandings of the particle gun rig, new meanings can be given to these two parameters.

The $(T\text{-}T_g)_{critical}$ has been conventionally used to indicate the critical combination of air temperature and RH which make a portion of the test powders sticky. Experimentally, this is indicated by the initiation of powder deposits build-up on the

sides of the collection plate. The other portion of the test powders may have also reached the same location on the collection plate but their surface conditions and kinetic energies are such that deposition is still not favoured. Alternatively, the other portion of test powers may have escaped the capture of the radial jets early on in the process and thus have not moved very much sideways parallel to the plate. The slope of the % deposition versus $T-T_g$ has been taken to indicate the rate of stickiness development. Experimentally, it is signified by the reducing proximity of the deposition location in relation to the impingement centre. It is also an indication of the number of rebounds before which the test powders will come to rest on the target plate.

While not geometrically similar to a spray dryer or the exhaust ducts in a milk powder plant, the particle gun rig in fact simulates the a series of complicated events including first-time collision, rebound and re-collision. The effect of airflow is not removed as it affects the trajectory of particles at all stages. Airflow may also contribute to re-entrainment of already deposited particles. All these features are inherent in all particle deposition process, regardless of the particular stages in the spray drying process of dairy powders.

3.4.2 Effect of Distance between the Gun Tip and Target Plate

Murti (2006) has varied the distance between the gun tip and collection plate from 120 mm to 160 mm and concluded that at normal angle of impingement, % deposition in general increases with increasing distance. In most of Murti's experiments, the particle impingement velocity has been assumed to be at 20 m/s, which is the same as the air velocity at the particle gun exit. Although the actually average velocity may be as high as 50 m/s. Thus, it is intriguing to see even at supposedly the same particle impingement velocity, there are still differences in % deposition due to the distance effect. Murti (2006) has attributed this to the differences in air flow close to the target

plate. Treating the particle gun setup as an impingement jet, 160 mm would translate into an H/D ratio of 20, given the diameter of the Perspex pipe used in their study is 8 mm. It is known at this large H/D ratio, the jet would have decayed and expanded significantly. It is desirable to choose an H/D ration such that the jet does not develop and particles do not experience deceleration. An H/D ratio of 2 (H = 22 mm, D = 11 mm) and 10 (H = 110 mm, D = 11 mm) is investigated at the beginning of this study. For the lower ratio, it is found that a significant portion of the particles are seen to rebound from the target plate and get stuck at the gun tip. Some of these stuck powders will come loose and collide again with the plate. Due to the high air flow rate, at high $T-T_g$ levels some particles are seen to deposit briefly on the plate but will subsequently get re-entrained into the airflow. Murti (2006) has also observed rolling off of large particle agglomerates, although in this study it is found that smaller particles are subjected to the same mechanism. Re-entrainment of the deposits is more prominent at higher velocity and therefore must be related to the higher shear stress caused by the stronger air flow at the target plate surface.

Towards the higher end of the H/D ratio, and at high levels of relative humidity, condensation has been observed at the peripheries of the target plate. This is obviously undesirable as one is only interested in the particle deposition caused by the formation of immobile liquid bridges between the test powders and the plate, not humidity-assisted adhesion due to capillary pressure. On the other hand, this observation shows that the temperature of the hot air jet is not constant once it leaves the tip of the gun. The development and the accompanied flattening of the jet would have entrained slower moving air at the shear layer. In the meantime, the temperature of jet would also have been decreased due to this mixing of cold ambient air in the laboratory. It is believed at intermediate ratios of H/D, while no condensation has been observed, the cooling of the jet would still take place to a certain extent. From a typical sticky point curve for dairy powders, it is known that this drop in temperature would lead to an increase in relative humidity of the air, which would in turn make the actual $T-T_g$ condition experienced by the particles at the point of deposition higher

than that at the exit of the particle gun and reported in the results.

Thus, the observed decrease in $(T-T_g)_{critical}$ and increase in the slope of the deposition curve with increasing H/D ratio reported by previous researchers could be attributed to the decrease in particle impingement velocity (kinetic energy), reduced velocity magnitude of the air close to the plate and a possible increase in the actual $T-T_g$ of the particles at the point of collision. It has been decided that all subsequent experiments would be carried out at a standard H/D ratio of 4 (44 mm). This helped to eliminated the problem of particle rebound into the rig itself, as well as ensuring the $T-T_g$ values at the point of particle collision is in close range of those measured at the exit of the particle gun.

3.4.3 Effect of Air Velocity

The lowest velocity past workers have reported to operate the particle gun rig is 10 m/s (Murti, 2006), however the actual air velocity may be closer to 25 m/s (see Chapter 3.2.4). Below this velocity, Murti (2006) has found that extensive agglomeration of the test powders were taking place inside the Perspex pipe. Since the feed rate of the powder has been kept constant at 0.3 g/s in that study, a reduced conveying velocity would effectively increase the particle concentration in the pipe and enhance the particle-particle interactions. Due to the modified powder feeding method adopted in this study, a powder feed rate of 0.05 g/s has been achieved. As a result, the rig is able to be operated at a lower velocity range without interferences of powder agglomeration. An investigation of the effect of velocity on the deposition behaviour of standard, un-sieved skim milk powder (bulk) has been carried out at a range of values and the result is shown in Figure 3.11 and Table 3.4.

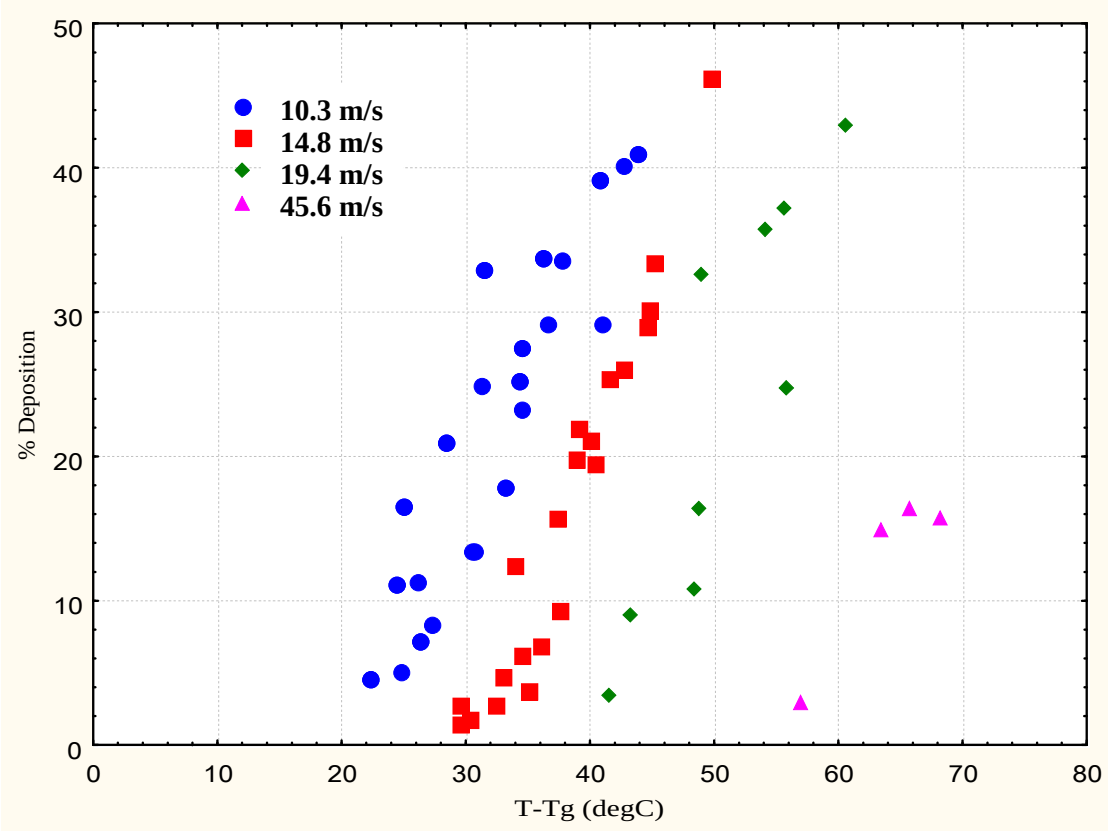

Figure 3.11 Effect of air velocity on particle gun results for SMP, bulk size range and air jet 90° to plate.

Table 3.4 Effect of air velocity on $(T\text{-}T_g)_{critical}$ and slope.

Size Fraction	Velocity (m/s)	$(T\text{-}T_g)_{critical}$	Slope %Deposition/ °C	R^2 of slope
Bulk	10.3	18.6	1.67	0.82
Bulk	14.8	30.1	2.17	0.93
Bulk	19.4	39.0	2.02	0.78
Bulk	45.6	53.4	1.23	0.87

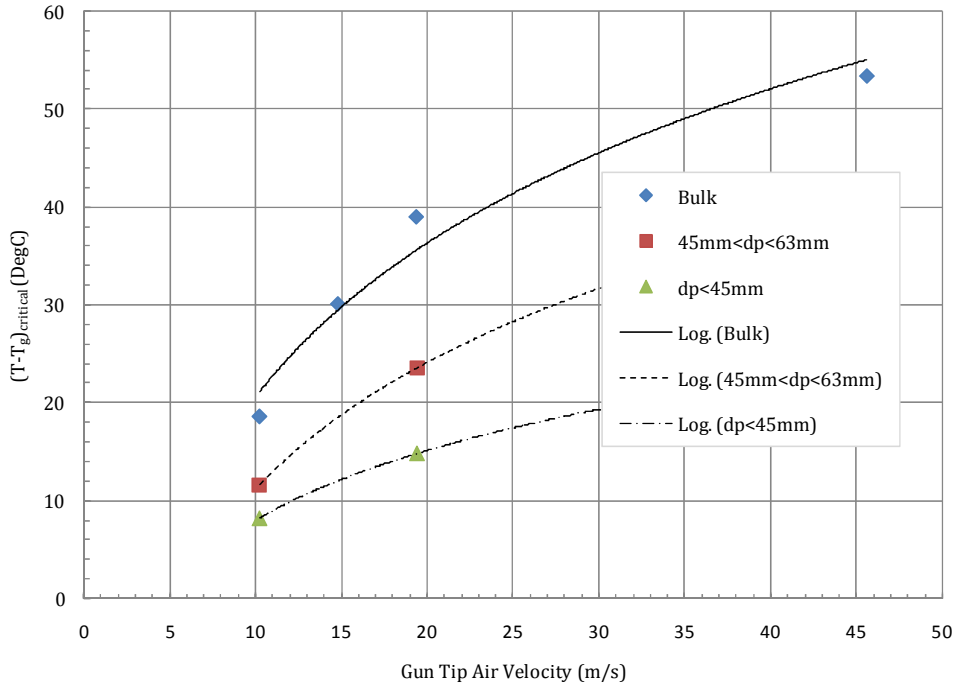

Figure 3.12 Effect of gun tip air velocity on the $(T-T_g)_{crtical}$ for SMP at three particle size ranges and air jet 90^o to plate.

Figure 3.11, Figure 3.12 and Table 3.4 show that the $(T-T_g)_{critical}$ is a strong function of the conveying air velocity, increasing from 18.6 °C to 53.4 °C as the velocity is increased from 10.3 m/s to 45.6 m/s for the bulk SMP. The same trend has been identified at small particle size distributions (Figure 3.13) and by Murti (2006) to a lesser extent, confirming the velocity dependency of the particle gun rig results. However, in this study the test powders appear to be much less stickier than that found by previous studies, e.g. $(T-T_g)_{critical}$ of 53.4 °C compared to 33.6 °C by Murti (2006) and an average of 39°C by Zuo (2004). This difference is most likely due to the very short spacing between the gun tip and the collection plate (H/D ratio = 4) adopted in this study, which would have caused the air velocity and, therefore, particle velocity to be considerably higher at impact than that in previous studies (H/D ratio = 20). Better understanding of the actual flow field around the plate at different air jet velocities and H/D ratios is need to draw further conclusions about the effect of jet

velocity on deposition.

It is interesting to note that the $(T\text{-}T_g)_{critical}$ of 18.6 °C at 10.3 m/s is very close to the range of sticky point values obtained by the fluid bed rig test (Murti, 2006). Previous researchers have explained the differences in results with the different velocity magnitudes employed. However, 10.3 m/s used in this study is still high compared to the average of 0.23 m/s employed in the fluid bed test. Also, the fluid bed measures cohesion while the particle gun measures mainly adhesion. As previously pointed out, the deposit morphology observed at around stickiness initiation point indicates that particles do not deposit upon the first impact. The deposits are concentrated around the periphery of the collection plate and they may have resulted from multiple collisions and rebounds before finally coming to rest. Thus, the final collision velocity at which the particles are captured by the plate is likely to be much lower than 10.3 m/s and closer to the velocity in the fluid bed. If this is the case, then the same sequence of events would hold true for experiments at other velocities. The differences observed between data in Figure 3.11 will be due to the differences in average kinetic energies of ensembles of the test powders.

The rate of stickiness development obtained in this study is much lower compared to previously reported slopes (3.1% deposition/ °C). Furthermore, there is no discernible overall change in the slopes as the velocity is increased. This means that with an increase in the average velocity of the particles, the % deposition at each level of $T\text{-}T_g$ is reduced by more or less the same percentage.

3.4.4 Effect of Particle Size Distribution

It has been shown that a change in kinetic energy of particle collisions due to changing velocity has a marked effect on the $(T-T_g)_{critical}$ and % deposition at all subsequent levels of $T-T_g$. It is known that in addition to the effect of velocity, the mass of the impinging particles also contributes to their kinetic energies. Preliminary studies with the fluid bed test (Pearce, 2004) has shown that the sticky point curves for skim milk powders are size dependent, with finer particles shown to be stickier than coarse particles. However, most of the current sticky point curves implemented in industry are obtained from bulk particles. Particles encountered in the exhaust ducts of spray dryers are typically referred to as “fines” due to their smaller average sizes compared to the bulk products. If there are significant differences in the stickiness and deposition tendency between bulk particles and fines, then sticky point curves based on bulk particles will be over conservative and underestimate the actual deposition propensity in the dryer exhausts.

Bulk skim milk powders are sieved to yield samples of narrower size distributions. As previously explained, two fine fractions (d_p< 45 μm and 45 μm < d_p <63 μm) and bulk particles have been used in this study. The effect of particle size distribution on the stickiness and deposition of skim milk powders is clearly shown on Figure 3.13 and 3.14. With the air velocity held constant, it is seen that particles with smaller average sizes are always stickier, as supported by the reduced $(T-T_g)_{critical}$. At 10.3 m/s, there seems to be some overlapping in the deposition curve between the bulk particle fraction and the fraction having particle size range of 45 μm < d_p <63 μm. On the other hand, the particle size effect seems to be stronger at a higher conveying air velocity of 19.4 m/s, possibly due to an interaction effect between particle size and impinging velocity.

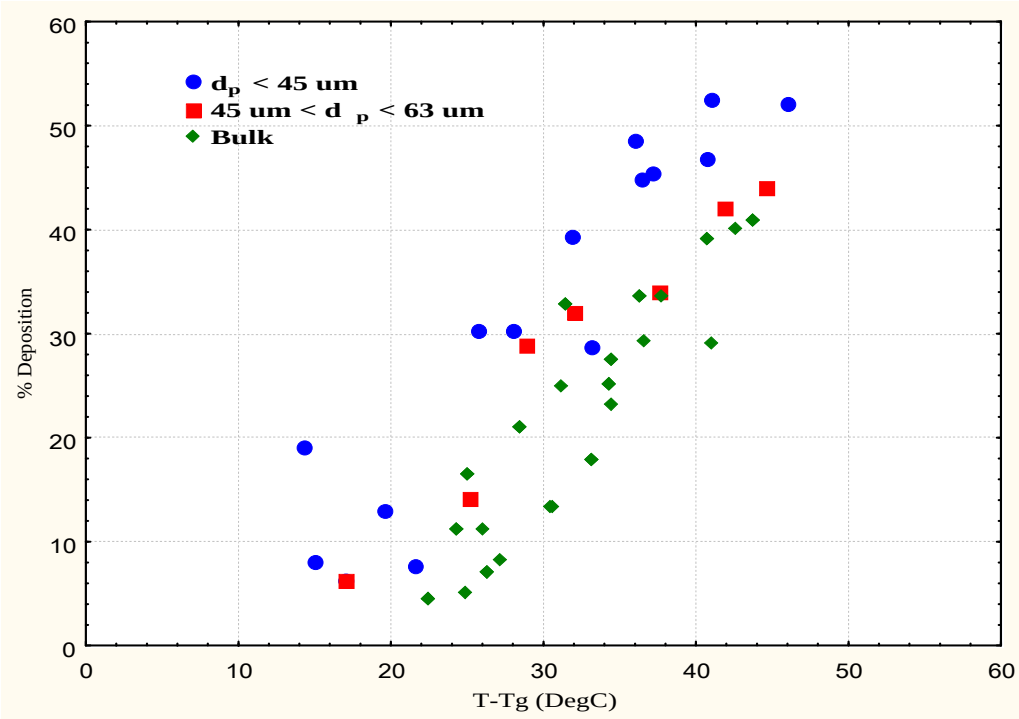

Figure 3.13 Effect of particle size distributions on the particle gun results at 10.3 m/s of air velocity and air jet 90^o to plate.

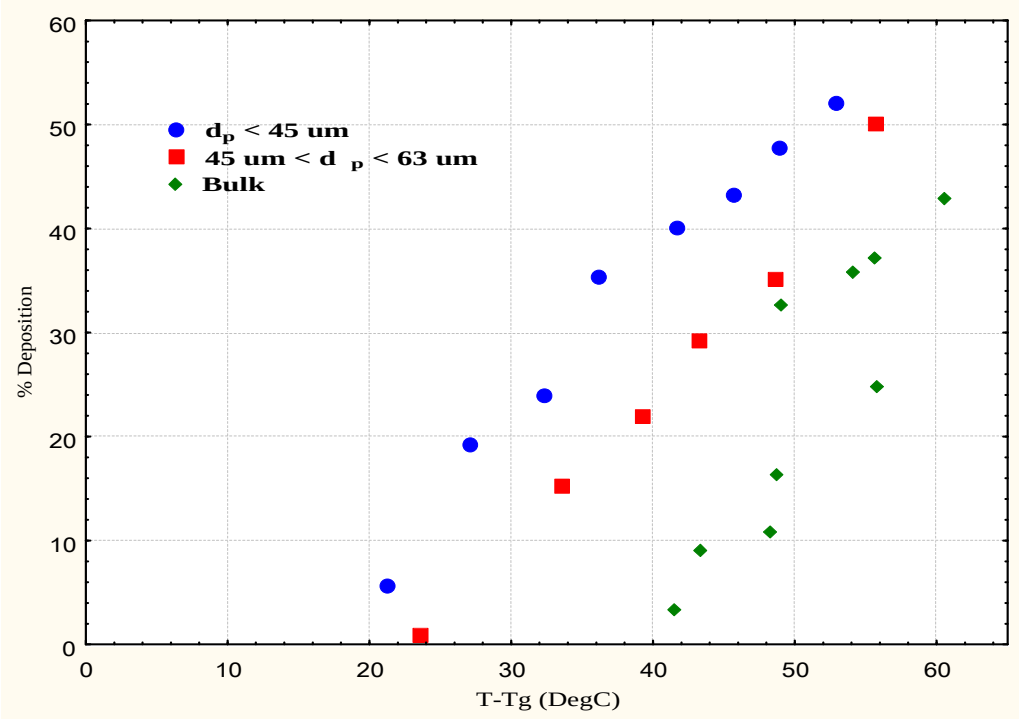

Figure 3.14 Effect of particle size distributions on the particle gun results at 19.4 m/s of air velocity and air jet 90^o to plate.

Table 3.5 summarises the $(T\text{-}T_g)_{critical}$ and slope of the deposition curve for the results obtained. A near straight line correlation is found between $d(0.5)^2$ of the size distribution and $(T\text{-}T_g)_{critical}$ and this is shown in Figure 3.15.

Table 3.5 Effect of particle size distribution on $(T\text{-}T_g)_{critical}$ and slope.

Size Fraction	Velocity (m/s)	$(T\text{-}T_g)_{critical}$ °C	Slope %deposition/°C
d_p< 45 µm	10.3	8.2	1.50
45 µm < d_p <63 µm	10.3	11.6	1.39
Bulk	10.3	18.6	1.67
d_p< 45 µm	19.4	14.8	1.43
45 µm < d_p <63 µm	19.4	23.5	1.49
Bulk	19.4	39.0	2.02

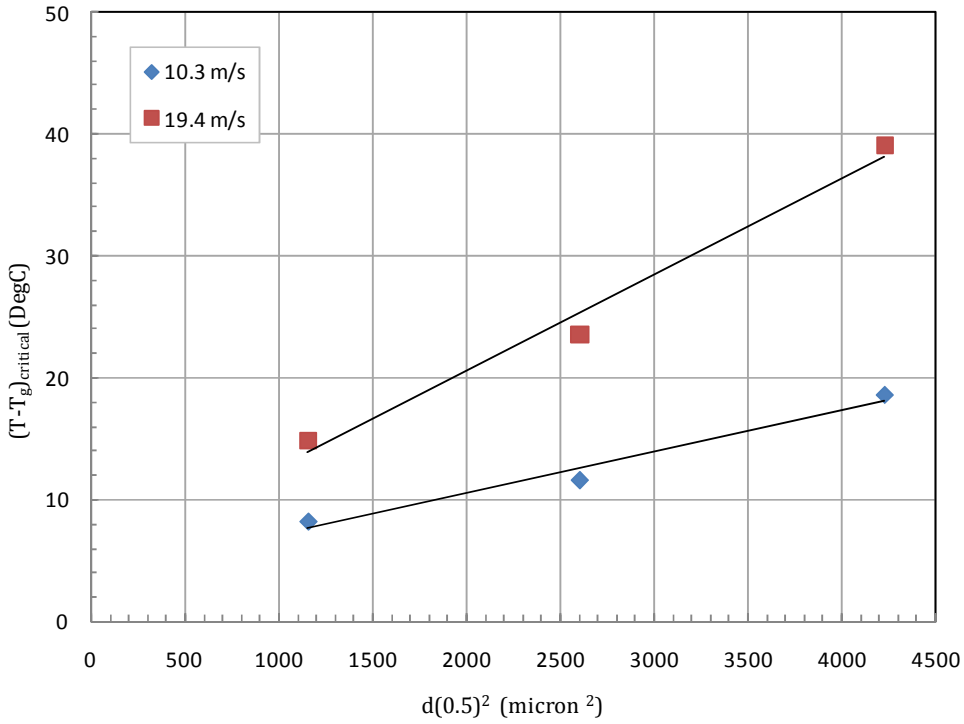

Figure 3.15 Effect of particle size expressed in $d(0.5)^2$ versus $(T\text{-}T_g)_{critical}$.

As shown in Table 3.5 and Figure 3.15, the $(T\text{-}T_g)_{critical}$ increases with increasing particle size distributions, even at the same conveying velocity. This observation confirms the hypothesis that the onset of stickiness for skim milk powders is controlled by the specific contact dynamics between the impinging particles and the collection plate. This contact dynamics are in turn a strong function of the kinetic energy of the impinging particles, in which both the velocity and particle sizes play an important part. Although no discernible trend exists for the slope of the deposition to vary with particle size distributions, Figure 3.13 and 3.14 show that the deposition propensity for smaller particles is always higher than that of the larger particles at a given level of $T\text{-}T_g$. This finding has important relevance for the adoption of the $(T\text{-}T_g)_{critical}$ concept in plant, as smaller particles encountered in the exhaust ducts and cyclones will have a higher deposition tendency for deposition than the bulk particles.

Murti (2006) has found that the initial water activity of the particles has a significant effect on the rate of stickiness development (slope of the deposition curve). This has been attributed to the rate of moisture transfer into the particles as a rate-limiting step. It has been shown that up to a $T\text{-}T_g$ of around 40°C the rate of stickiness development remains the same for powders with different initial moisture content and then starts to differentiate. Murti (2006) has used Equation 3.7 from Perry and Green (1997) for estimating the fraction of the particle volume affected by the air conditions in the particle gun.

$$F_A = \frac{6}{R}\sqrt{\frac{Dt}{\pi}} \tag{3.6}$$

where R is the radius of the particle, D is moisture diffusivity in amorphous lactose (m^2/s) and t is time. It is seen in Equation 3.6 for the same water diffusivity and duration in the particle gun chute, the particle volume affected (F_A) is inversely proportional to the particle size. In other words, large particles would have been

conditioned to a less extent than smaller particles for the same conditions in the particle gun. The change in slope after a $T-T_g$ value of 40 °C reflects the fact that for larger particles to deposit, the interior moisture content is as equally important as the surface condition. Smaller particles only require their surface to be sticky for deposition to occur, possibly due to their lower kinetic energy at collision and thus less energy to be dissipated.

3.4.4 Plate Temperature Considerations

The affect of plate temperature on % deposition and $(T-T_g)_{critical}$ has not been considered in this work, nor has it been considered a significant factor by past researchers. This work has assumed that a particle impacting on a dry plate will have insufficient time to change surface conditions to any significant degree. However, this is an area of possible future research. For the record the plate temperature was measured using a K type thermocouple and found to have a temperature at the centre of 45 °C and a temperature at the periphery of 25 °C for an average air jet temperature of 75 °C used in this study.

3.5 CONCLUSION

This chapter has reviewed the past works done with the particle gun rig. Comparison with other test rigs for testing stickiness behaviour shows that the particle gun test has the extra advantage of being able to simulate the actual particle adhesion and collision dynamics. Murti (2006) has shown the effect of air velocity has a profound impact on the test results. In this study, lower velocity range and a lower H/D ratio than that used by previous researchers has been used and the $(T-T_g)_{criticial}$ is reduced from 53.4°C to 18.6°C as velocity is reduced from 45.6 m/s to 10.3 m/s. Moreover, it has been

demonstrated that the particle size also affects the test results. It has been postulated that the particle deposition mechanism of skim milk powder is ultimately controlled by the kinetic energies of the particles during impact. The deposit morphology observed at various $T\text{-}T_g$ suggests that the deposited particles on the collection plate results from a series of collision/rebound events. To better study this phenomenon, it is desirable to make use of Computational Fluid Dynamics. In the next chapter, the basic principles of CFD and particle deposition from a fluid mechanic point of view are discussed. In Chapter 5, CFD will be employed to simulate the particle gun test in more details.

CHAPTER 4 - COMPUTATIONAL FLUID DYNAMICS AND PARTICLE DEPOSITION MECHANISMS

4.1 INTRODUCTION

It has been realized from the start of the project that particle deposition is a two-step process that involves the particles first arriving at the wall surface and the subsequent interaction results in either stick or rebound of the particles. Experimental results from Chapter 3 show that the deposition of skim milk powder is dependent on stickiness of the particle and the underlying fluid mechanics. It is desirable to use Computational Fluid Dynamics (CFD) method to further study the mechanisms of particle deposition observed experimentally with the particle gun test. This chapter gives an overview of CFD modelling, with a specific emphasis on the modelling of particle deposition. A test case is also performed at the end of the chapter to increase the confidence in the modelling approach later used in Chapter 5.

4.2 COMPUTATIONAL FLUID DYNAMICS

4.2.1 Overview

Computational Fluid Dynamics refers to the numerical modelling of fluid flow and related phenomenon such as heat transfer and particle deposition. With the rapid increase in computational power and reducing cost, CFD has become an indispensable tool in the design and modelling of industrial processes. Commercial CFD codes such

as Fluent and CFX are also based on the sophisticated numerical algorithms but are user-friendly. They are suited for engineers and researchers who have a good understanding of the fluid mechanics of the problems at hand but do not want to get trapped in the intricacies of developing their own codes. In this study, the commercial code Fluent 6.3 and 12, and its pre-processer Gambit 2.4 are used for all the modelling.

4.2.2 Conservation of Mass and Momentum

Figure 4.1 shows an infinitely small fluid particle located in a Cartesian coordinate, with its centre at the position (x, y, z).

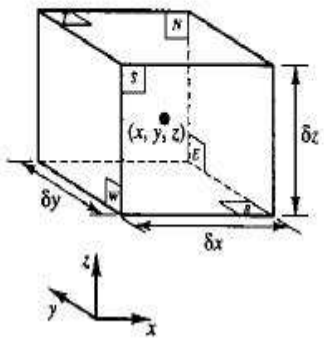

Figure 4.1 Fluid particle for derivation of laws of conservation of mass and momentum.

It can be shown that a mass balance around the eight surfaces of the fluid elements leads to

$$\frac{\partial \rho}{\partial t} + \frac{\partial (\rho u)}{\partial x} + \frac{\partial (\rho v)}{\partial y} + \frac{\partial (\rho w)}{\partial z} = 0 \qquad (4.1)$$

where ρ is the fluid density, t is time and u, v, and w are the three components of the velocity vector. In vector form, Equation 4.1 can be expressed as

$$\frac{D\rho}{Dt} = \frac{\partial \rho}{\partial t} + \nabla \cdot \rho \mathbf{V} = 0 \tag{4.2}$$

where $D(\rho)/Dt$ is the material derivative of density. Equation 4.2 is the unsteady, three-dimensional continuity equation for a compressible fluid. It is also one of the key equations to be discretized and solved numerically in CFD. For incompressible fluid where the density remains constant with time, Equation 4.2 is reduced to

$$\nabla \cdot \mathbf{V} = 0 \tag{4.3}$$

The conservation of momentum is derived from Newton's second law which states that the rate of change of momentum of a fluid particle equals the sum of the forces acting on the particle. There are two types of forces acting on a fluid particle: surface force and body force. Figure 4.2 illustrates the surface force, which consists of both pressure force, normal viscous force and shearing viscous force.

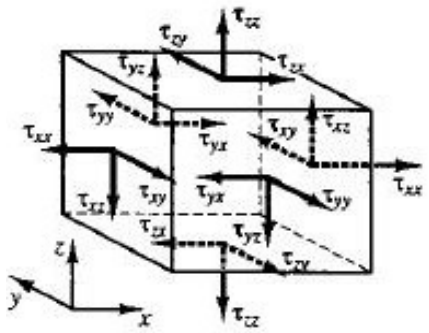

Figure 4.2 Stress components acting on the fluid element.

A force balance around the fluid element shown in figure 4.2 leads to

$$\rho \frac{Du}{Dt} = \frac{\partial(-p+\tau_{xx})}{\partial x} + \frac{\partial \tau_{yx}}{\partial y} + \frac{\partial \tau_{zx}}{\partial z} + S_{Mx} \tag{4.4a}$$

$$\rho \frac{Dv}{Dt} = \frac{\partial \tau_{xy}}{\partial x} + \frac{\partial(-p+\tau_{yy})}{\partial y} + \frac{\partial \tau_{zy}}{\partial z} + S_{My} \tag{4.4b}$$

$$\rho \frac{Dw}{Dt} = \frac{\partial \tau_{xz}}{\partial x} + \frac{\partial \tau_{yz}}{\partial y} + \frac{\partial(-p+\tau_{zz})}{\partial z} + S_{Mz} \tag{4.4c}$$

where p is pressure, τ is the viscous stress and S_M is a general term including all the body forces. Equation 4.4 a, 4.4 b and 4.4 c represent the x, y, and z-component of the momentum equations, respectively.

4.2.3 Navier-Stokes Equations

The normal and shearing viscous stresses can be expressed as

$$\tau_{xx} = 2\mu \frac{\partial u}{\partial x}$$

$$\tau_{yy} = 2\mu \frac{\partial v}{\partial y}$$

$$\tau_{zz} = 2\mu \frac{\partial w}{\partial z} \tag{10.3}$$

$$\tau_{xy} = \tau_{yx} = \mu\left(\frac{\partial u}{\partial y} + \frac{\partial v}{\partial x}\right)$$

$$\tau_{xz} = \tau_{zx} = \mu\left(\frac{\partial u}{\partial z} + \frac{\partial w}{\partial x}\right)$$

$$\tau_{yz} = \tau_{zy} = \mu\left(\frac{\partial v}{\partial z} + \frac{\partial w}{\partial y}\right)$$

Substitution of Equation 10.3 into Equation 4.4 leads to the Navier-Stokes Equation in its most useful form.

$$\rho \frac{Du}{Dt} = -\frac{\partial p}{\partial x} + \nabla \cdot (\mu \nabla u) + S_{Mx} \quad (4.6a)$$

$$\rho \frac{Du}{Dt} = -\frac{\partial p}{\partial y} + \nabla \cdot (\mu \nabla v) + S_{My} \quad (4.6b)$$

$$\rho \frac{Du}{Dt} = -\frac{\partial p}{\partial z} + \nabla \cdot (\mu \nabla w) + S_{Mz} \quad (4.6c)$$

4.2.4 Turbulence Modelling and Reynolds Averaged Navier-Stokes Equations

For laminar flows, the continuity equation and the Navier-Stokes equations presented previously can be solved analytically or easily with CFD. However, most of flow situations encountered in engineering are turbulent in nature. Turbulent flows are characterized by random and three-dimensional eddies, with a wide range of length scales. Large eddies are dominated by inertia effects and viscous effects are negligible. They are created through a process known as vortex stretching and their energies are extracted from the mean flow. These large eddies are unstable and they tend to break up and become progressively smaller until viscous effects become dominant, and the smallest eddies are dissipated. Turbulence is known to give rise to additional stress terms known as Reynolds stresses. Turbulent flow properties such as velocity and pressure can be decomposed into a mean value and fluctuating component (e.g. Equation 4.7) in a process known as Reynolds decomposition.

$$u(t) = \bar{u} + u'(t), \quad v(t) = \bar{v} + v'(t), \quad w(t) = \bar{w} + w'(t), \quad p(t) = \bar{p} + p'(t) \quad (4.7)$$

Replacing the pressure and velocity terms in the Navier-Stokes equations with the form in Equation 4.7 and subsequent averaging of the equations lead to

$$\frac{\partial \bar{u}}{\partial t} + \nabla \cdot \overline{u\mathbf{V}} = -\frac{1}{\rho}\frac{\partial \bar{p}}{\partial x} + \upsilon \nabla \cdot (\nabla \bar{u}) + \frac{1}{\rho}\left[\frac{\partial(-\rho\overline{u'^2})}{\partial x} + \frac{\partial(-\rho\overline{u'v'})}{\partial y} + \frac{\partial(-\rho\overline{u'w'})}{\partial z}\right] \quad (4.8a)$$

$$\frac{\partial \bar{v}}{\partial t} + \nabla \cdot \overline{v\mathbf{V}} = -\frac{1}{\rho}\frac{\partial \bar{p}}{\partial y} + \upsilon \nabla \cdot (\nabla \bar{v}) + \frac{1}{\rho}\left[\frac{\partial(-\rho\overline{u'v'})}{\partial x} + \frac{\partial(-\rho\overline{v'^2})}{\partial y} + \frac{\partial(-\rho\overline{v'w'})}{\partial z}\right] \quad (4.8b)$$

$$\frac{\partial \bar{w}}{\partial t} + \nabla \cdot \overline{w\mathbf{V}} = -\frac{1}{\rho}\frac{\partial \bar{p}}{\partial z} + \upsilon \nabla \cdot (\nabla \bar{w}) + \frac{1}{\rho}\left[\frac{\partial(-\rho\overline{u'w'})}{\partial x} + \frac{\partial(-\rho\overline{v'w'})}{\partial y} + \frac{\partial(-\rho\overline{w'^2})}{\partial z}\right] \quad (4.8c)$$

Equation 4.8 is the Reynolds-Averaged Navier-Stokes equation. Comparison with Equation 4.6 shows that the additional terms in the large bracket containing the fluctuating components of velocity arise due to turbulence and Reynold's decomposition.

CFD offers broadly three approaches for the analysis of turbulent flow problem:

- Direct Numerical Simulation (DNS)
- Large Eddy Simulation (LES)
- Reynolds Averaged Navier-Stokes (RANS) equations

In DNS, turbulence from large eddies down to the Kolmogorov scale is calculated, without any modeling assumptions. This requires the simulation of the unsteady Navier-Stokes equations on a very fine grid. Such calculations are highly costly in terms of computing resources and are generally restricted to simple flows with low Reynolds numbers.

The LES is an intermediate form of turbulence analysis. In this method, the large eddies are tracked while the smaller eddies are modelled. The need to calculate large eddies directly arises from the fact that they are highly anisotropic and vary greatly in

length scales. The smaller eddies are thought to be more isotropic and have a universal behaviour. Prior to computation, LES uses a spatial filtering function to separate the larger and smaller eddies. During spatial filtering information relating to the smaller, filtered-out turbulent eddies is destroyed. The contribution from these filtered-out smaller eddies to turbulence is known as sub-grid-scale stresses and there are various sub-grid-scale models in literature for modeling them. LES is less computationally expensive than DNS and its popularity has been rapidly increasing.

Turbulence models based on the Reynolds Averaged Navier-Stokes (RANS) equations are the most common and popular group in CFD research. It has a specific emphasis on modelling the statistically averaged mean flow field, and only provides lower order turbulence statistics. Due to the very different behavior of large and small eddies and the flow geometry dependence, a general purpose RANS turbulence model suitable for a wide range of practical applications is not available. CFD users need to carefully choose from a number of available RANS models, which best suits the problem at hand and one preferably has been validated against experimental measurements. Usually RANS turbulence models are classified by the number of transport equations that need to be solved in addition to the continuity and Navier-Stokes equation. Table 4.1 shows the common models available in Fluent. A critical review of all the RANS models is not given here in this study. Readers should consult standard CFD textbooks such as Versteeg and Malalasekra. (2007), Fluent User Guide (2005) and Wilcox (2007), for more information.

Table 4.1. RANS turbulence models in Fluent.

Number of extra transport equations	***Name***
One	Spalart-Allmaras model
Two	$k-\varepsilon$ model and variants
Two	$k-\omega$ model and variants
Two	v^2-f model
Seven	Reynolds stress model

In general, the one and two-equation turbulence models are based on the Boussinesq

hypothesis, which assumes isotropy in turbulent Reynolds stresses. The Reynolds stress model (RSM) is more elaborate and solves the transport equations of the six independent Reynolds stresses individually. This results in the RSM being much more computationally expensive than other models. In this thesis, the RSM model has been chosen for modelling particle deposition in a straight duct, in accordance with the work of Tian and Ahmadi (2007). For the CFD modelling of the particle gun in Chapter 5, the Shear Stress Transport (SST) $k-\varepsilon$ model is used.

4.3 PARTICLE DEPOSITION MECHANISMS

In isothermal turbulent flows, particle transport and deposition mechanisms are dominated by inertial impaction, turbulent diffusion, Brownian diffusion and gravity force (Konstandopoulos, 1991). In the presence of a strong temperature gradient, thermophoretic force also affect the particle motion and the mass rate of deposition (Lin *et al.*, 2004).

4.3.1 Inertial Impaction

Inertial impaction is caused by the inability of the particles to follow exactly the curved fluid streamlines. It takes place when the momentum of the particle toward the surface is large enough to overcome drag forces produced by fluid flow (Konstandopoulos, 1991; McFarland *et al.*, 1997). As a result, particles pass through the boundary layer and impact the surface. Figure 4.3 shows the inertial impaction of particles on a cylinder in a cross flow. For a given flow, the inertia effect increases with increasing particle size. The particle deposition efficiency describes the propensity of particles to stay on the surface upon impact. Both particle and surface properties such as surface tension and particle stickiness will play significant roles in

determining this capture efficiency. A more detailed discussion regarding deposition efficiency of dairy powders is given in Section 5.5.

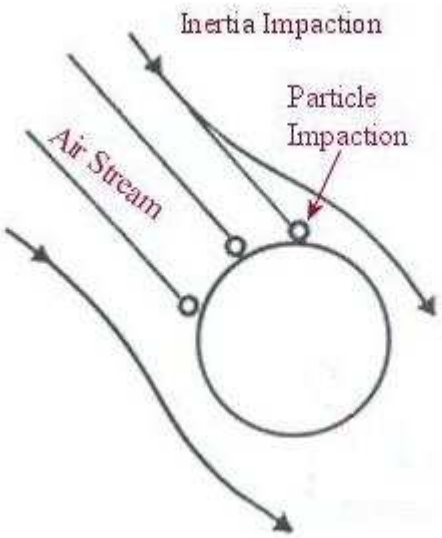

Figure 4.3 Particle deposition due to inertial impaction.

4.3.2 Turbulent Impaction

Turbulent impaction occurs when fine particles interact with and extract kinetic energy from turbulent eddies. These eddies add momentum to the particles and cause the particles to deviate from their mean trajectory. A classic example of particle deposition due to turbulent impaction involves particle deposition in straight pipes and ducts. Despite the main flow and particle motion in the axial direction of the pipe, significant particle deposition has been observed on the side walls (Friedlander and Johnstone, 1957; Liu & Agarwal,1974). Friedlander and Johnstone (1957) put forward a particle free-flight model to explain this, as shown in Figure 4.4.

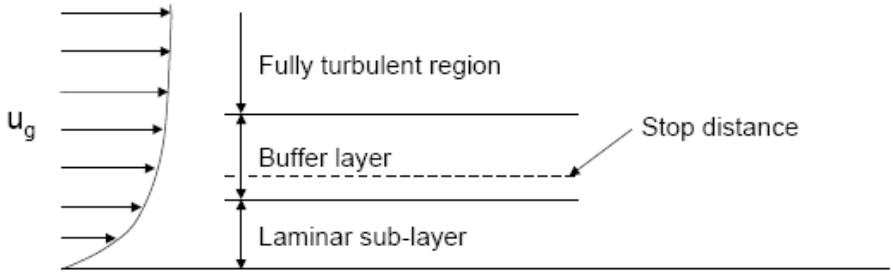

Figure 4.4 Illustration of the free-flight model of Friedlander and Johnstone (1957), taken from Kaer (2001).

Friedlander and Johnstone (1957) postulated that particles are transported in the inertia dominated turbulent core region due to turbulent diffusion to within one stop distance from the boundary wall, and the particles are able to fly across the viscous sub-layer and deposit on the wall. The free-flight theory is interesting but is physically incorrect. Friedlander and Johnstone (1957) has assumed that particles begin their free flight with a velocity approximately equal to the friction velocity of the flow. However, local velocity in the buffer layer and viscous sub-layer is too low to provide the energy needed (Davies, 1965; Young and Leeming, 1997). In subsequent works, various authors have proposed that deposition is due to the near wall coherent eddies and particles obtain their kinetic energy from a process known as turbulent bursts (Owen, 1969; Fan and Ahmadi, 1993).

4.3.3 Brownian and Turbulent Diffusion

Brownian motion arises due to the random interactions between particles and air molecules. There is a net flux of particles from regions of high concentration to low concentration (Marchioli and Soldati, 2002). The rate of particle deposition at the wall due to Brownian motion can be calculated through Fick's Law of Diffusion,

$$J_B = -D_B \frac{dC}{dy} \tag{4.9}$$

where J_B is the particle flux or deposition rate, D_B is the particle Brownian diffusivity and dC/dy is the particle concentration gradient. Particle deposition due to Brownian diffusion is generally significant for sub-micron particles only (Ounis *et al.*, 1993).

In addition to Brownian motion, turbulence also gives rise to diffusive flux of particles. Equation 4.9 can be further expanded to include the contribution from turbulent fluctuations.

$$J = -(D_B + \varepsilon)\frac{dC}{dy} \tag{4.10}$$

where ε is the eddy diffusivity of particles and it is typically taken to be the same of eddy viscosity of air (Lin *et al.*, 1953). As with Brownian motion, particle deposition due to turbulent diffusion also requires the presence of a concentration gradient near the wall.

Transport of particles by turbulent diffusion is highly dependent on the presence of a concentration gradient and is very efficient for particle dispersion in regions of homogenous turbulence, such as in the turbulent core of pipe flow. However in a region where a significant turbulence intensity gradient is present, such as within the boundary layer of a turbulent flow, particle transport by turbulent eddies will be more dominant, which is also not dependent on a concentration gradient.

4.3.4 Thermophoresis

Steep temperature gradients surrounding a particle can give rise to thermophoretic forces. In general, thermophoresis acts in the direction opposite to that of the temperature gradient and transports particles towards regions of lower temperature. Like Brownian and turbulent diffusion, thermophoresis is only significant for submicron particles (Zheng, 2002; Lin *et al.*, 2004).

4.3.5 Eulerian versus Lagrangian Tacking of Particles

Numerical modeling of particle transport and deposition can be developed either in the Eulerian or Lagrangian framework (Guha, 2008). The Eulerian approach is based on the assumption that the particles are present as a second continuous field and the transport equations are solved simultaneously for both air and the particle phase. The Eulerian approach is suitable for a range of multiphase flows in which the particulate loading is significant. A shortcoming of the Eulerian particle transport models is that they do not provide the information on particle impaction at the surface. Hence, in an Eulerian framework one cannot model the particle-surface interactions, which limits its usefulness in numerical particle deposition studies.

In the Lagrangian approach, individual particle trajectory is simulated by solving the particle's equation of motion. Various forces applied on the particle can be included and the momentum equation for the particles is integrated with respect to time along the particle pathline. To obtain statistically meaningful results, typically tens of thousands of particles are simulated all at once. The Lagrangian approach is able to provide detailed information regarding the interactions of particles with solid boundary. The model is capable of accommodating a polydispersed particle size and it also allows for chemical reaction and evaporation typically encountered in industrial

processes. For all these reasons, the Lagrangian approach has found more uses in particle deposition modeling than the Eulerian approach.

To account for the effect of turbulence on particle transport and deposition, a stochastic eddy interaction model is usually incorporated into the Langrangian model. A velocity fluctuation is computed from the CFD turbulence models and superimposed on the calculated mean flow field. When integrating the trajectory of the particles, they are made to encounter a series of turbulent eddies in their path. Each eddy is given a characteristic lifetime. The interaction of the particle with a particular eddy is over either when the lifetime of the eddy is finished or the particle leaves the eddy. The particle will then continue on its path and encounter another turbulent eddy. This is repeated many times until a particle is captured by a wall surface or leaves the flow domain (Dehbi, 2008).

4.4 CFD MODELLING OF PARTICLE DEPOSTION – TEST CASE

CFD modelling of particle deposition in a straight duct was undertaken to build understanding of the important variables that influence particle deposition in a turbulent flow field. CFD was carried out with the commercial code Fluent 6.3. For CFD validation purposes, experimental data from the open literature is used for comparison with CFD results. A wide range of literature data for different duct dimensions and particle material properties is available. Thus, duct and particles of a range of dimension and properties were chosen in order to remove any modeling bias.

4.4.1 Simulation Geometry and Meshing

The meshing and modeling approach is similar to that employed by Tian and Ahmadi (2007). Figure 10.3 shows the dimension and meshing scheme used for the straight duct. The duct has a diameter of 0.02 m and a length of 1 m. A total of 55,000 quadrilateral cells were used for the simulation and grid independence study showed that the finer meshes made no difference in the results obtained. The cells close to the wall, i.e. boundary layer, are made denser than the core of the duct, with the first cell placed at 0.0005 m from the wall. This is needed to better resolve the flow profile in the boundary layer as well as satisfy the requirement of Enhanced Wall Treatment. 2D simulation is sufficient for the simulation because air flow profile in a straight duct is essentially two-dimensional in nature.

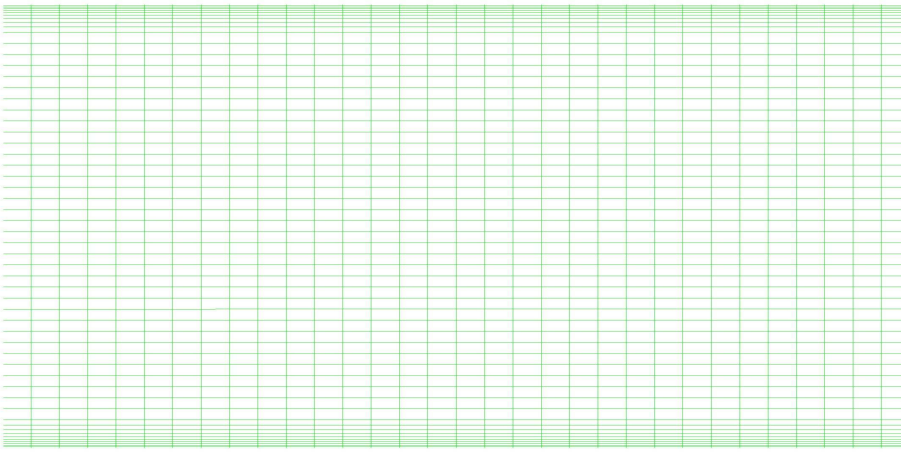

Figure 10.3 Geometry of 2D straight duct with mesh.

4.4.2 Continuous Phase Simulation

CFD simulation of particle deposition in this study follows both the Euler and Lagrangian approach. The continuous phase (air) flow field is obtained by solving the

conservation equations for mass and momentum (Equation 4.2 and Equation 4.8) – Euler approach. The average velocity of air for the simulations is 5 m/s for the 2D straight duct. The calculated Reynolds number is 6845, indicating turbulent flow. Tian and Ahmadi (2007) has shown that 2-equation RANS turbulence model together with the wall function approach can lead to an overestimated particle deposition rate due to their isotropic assumption of turbulence. For deposition in a straight duct, the driving force for particle deposition is the turbulence fluctuation in the wall direction, i.e. the normal Reynolds stress towards the wall. Thus, the accuracy of the predicted particle deposition will depend on the resolution of the near wall turbulence statistics (Kota and Langrish, 2006). Although Direct Numerical Simulation (DNS) and Large Eddy Simulation (LES) have been used quite successfully to predict particle deposition (Kota and Langrish, 2007), their high computational costs are prohibitive with current available computing power. Tian and Ahmadi (2007) have used the 7-equation Reynolds Stress Model together with Enhanced Wall Treatment near the wall for particle deposition. Despite the model being more computationally expensive than other 2-equation turbulence models, the significant improvement in predicted deposition rates justifies its use. In this test case, the continuous flow field is solved in steady state with the Reynolds Stress turbulence model and the Enhanced Wall Treatment for near wall turbulence resolution. Second order discretization schemes are used for all variables.

4.4.3 Discrete Phase Simulation

The particulate phase was solved with Fluent's Discrete Phase Model in a Lagrangian frame of reference (Fluent User's Guide, 2005). The dispersed phase is solved by calculating the trajectory of a representative number of inert particles, through the converged continuous phase flow field. In both cases, it is assumed that the inter-phase momentum exchange between the continuous and discrete phase is

relatively small due to volume loading of the particle being less than 10% of the air and one-way coupling is used. While the simulation of the continuous flow field involves the solving of the non-linear partial differential equations by an iterative approach, the particle trajectory is described by a set of ordinary differential equations written as

$$\frac{dV_p}{dt} = F_D\left(V - V_p\right) + \frac{g_x\left(\rho_p - \rho\right)}{\rho_p} + F_x \qquad (4.11)$$

The first and second term on the right hand side of Equation 4.11 is the drag force and gravitational force, respectively. For the 2D duct, gravity is not activated to keep the simulation in line with the actual experiment which investigated deposition in a vertical flow, and thus gravitational force plays no significant role in particle transport in the wall direction. The last term in Equation 4.11, F_x, represents additional forces such as Brownian and thermophoretic forces, which are not included in this case.

The turbulent dispersion of particles is simulated with Fluent's Discrete Random Walk model (DRW), which is based on a stochastic tracking approach. The interaction of particles with turbulent eddies can be the dominating deposition mechanism under some circumstances and the Discrete Random Walk model takes this into account by incorporating the instantaneous flow velocity into the equation of particle trajectory. The particles are made to encounter on their paths a series of turbulence eddies characterized by a Gaussian distributed random velocity fluctuation and an eddy lifetime. The velocity fluctuations u', v' and w' are obtained by assuming thy obey a Gaussian probability distribution,

$$u' = \varsigma\sqrt{\overline{u'^2}}\ , \quad v' = \varsigma\sqrt{\overline{v'^2}}\ , \quad w' = \varsigma\sqrt{\overline{w'^2}} \qquad (4.12)$$

where ς is a normally distributed random number.

The root mean square velocity fluctuation is obtained from the local kinetic energy. For turbulence models assuming isotropic Reynolds stresses, this is

$$\sqrt{\overline{u'^2}} = \sqrt{\overline{v'^2}} = \sqrt{\overline{w'^2}} = \sqrt{2k/3} \tag{4.13}$$

where k is the turbulent kinetic energy of the local flow. In Reynolds Stress model, each of the velocity fluctuations is individually obtained from the Reynolds stresses.

The interaction between a particle and a turbulent eddy will last until either the lifetime of the eddy is over or and particle leaves the eddy. The characteristic lifetime of the eddy, τ_e, is typically defined as a constant,

$$\tau_e = 2T_L \tag{4.14}$$

where T_L is the integral time scale, which can be taken to be the fluid Langragian integral time for small particles,

$$T_L = C_L \frac{k}{\varepsilon} \tag{4.15}$$

where C_L is a constant. The recommended value for C_L is 0.15 and 0.30 for $k-\varepsilon$ model and RSM model respectively.

4.4.4 Boundary Conditions

A uniform velocity of magnitude of 5 m/s normal to the inlet is specified. Pressure at the outlet is set to 0 Pa gauge. Turbulence intensity is set at 5% and the hydraulic

diameter used in the simulation is based on the diameter of the duct used in the literature data. For the 2D duct, 20000 particles are released from a point source at the inlet center and their initial velocities are made the same to the local gas velocity. Particle size in each simulation is constant and spans from 1 – 250 μm with a fixed density of 1300 kg/m^3. Fluent has a default option for particle trap or rebound at the wall surface. With the literature data, viscous oil was applied on the duct wall surface to minimize particle rebound. Thus, the trap option is specified in the simulation for the surface.

4.4.5 Results and Discussions

The results of particle deposition studies in a straight ducts are usually presented as curves of dimensionless particle deposition velocity, V_{dep}^{+}, versus dimensionless particle relaxation time, τ_p^{+} (Guha, 2008).

$$V_{dep}^{+} = \frac{V_{dep}}{u*} \tag{4.16}$$

$$\tau_p^{+} = \tau_p \frac{u*^2}{\upsilon} \tag{4.17}$$

Where $u*$ is the friction velocity and can be calculated as

$$u* = 0.2U\,\mathrm{Re}^{-1/8} \tag{4.18}$$

where U is the average flow velocity and Re is the Reynolds number.

The friction velocity is a common term in fluid mechanics for describing diffusion and dispersion phenomena and is an alternative illustration of wall shear stress in the

form of velocity. The particle deposition velocity, V_{dep}, is the particle mass flux at the wall surface (kg/m^{2}s) normalized by the particle concentration in the bulk flow (kg/m^3). The particle deposition velocity is obtained as

$$V_{dep} = \frac{J_{wall}}{C_{p,bulk}} \tag{4.19}$$

The particle relaxation time τ_p, also known as particle response time, is a measure of particle's inertia (Guha, 2008). Small particles tend to follow the flow very closely, with very small slip velocity and large particles tend to shoot ahead or lag behind the air flow (Friedlander and Johnstone, 1957). For a given particle with constant particle density, the increase in particle relaxation time represents an increase in the particle size. The particle relaxation time is defined as

$$\tau_p = \frac{\rho_p d_p^2}{18\mu} \tag{4.20}$$

A number of experiments reported in the literature have looked at particle deposition from fully developed turbulent flow over the years. Some of the experimental results are summarized in Figure 4.6, from Young and Leeming (1997).

Three regimes of particle deposition can be clearly identified in the graph. In the first, diffusional deposition regime, there is a slight decrease in the dimensionless particle deposition velocity with increasing dimensionless particle relaxation time. Particles in this regime are usually very small, with particle size less than 1 μm. The driving force for deposition is Brownian and turbulent diffusion. The decrease in deposition velocity is explained by the decrease in the Brownian diffusivity of particles. In the second diffusion-impaction regime, the dimensionless particle deposition velocity is seen to increase linearly over several orders of magnitude with the dimensionless

particle relaxation time. This is attributed to particles with significant inertia interacting with turbulent eddies and gaining enough momentum to coast to the wall (Friedlander and Johnstone, 1957; Young and Leeimg, 1997). In the inertia moderated regime, the very large particles are affected less by the turbulence and there is a slight decrease in deposition with further increase in particle size. Although data from different experiments have been non-dimensionalized to make them comparable, it can be seen from Figure 4.6 that there is still considerable scatter among the data set. However, the underlying trend with the three deposition regimes is the same in all experiments.

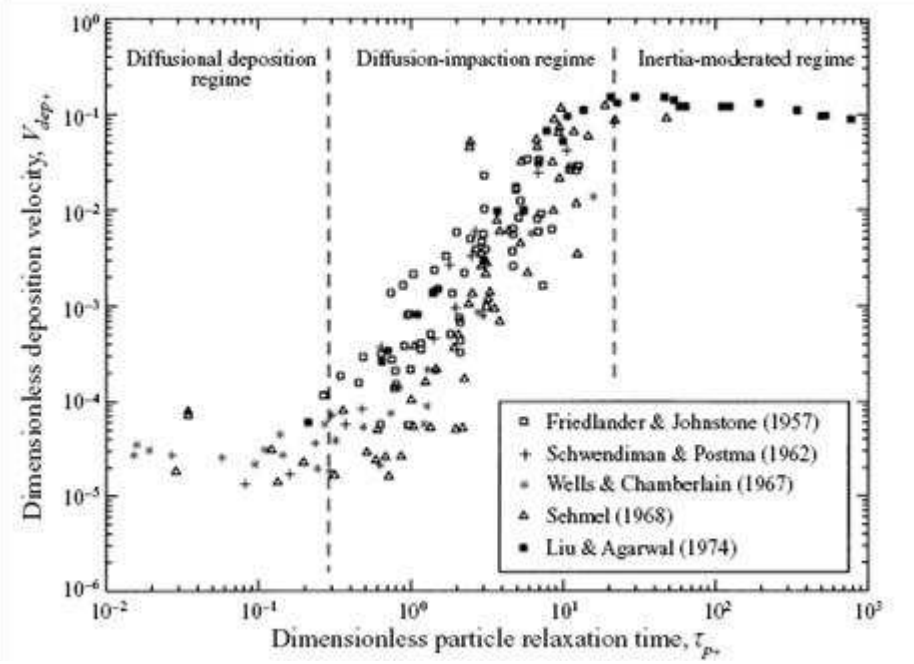

Figure 4.6 Deposition of particles from fully developed turbulent flow in a straight duct, taken from Young and Leeming (1997).

In this study, a procedure for analyzing particle deposition results from CFD has been devised. The particle relaxation time is calculated as usual from Equation 4.20. The particle mass flux at the wall surface, J_{wall} (kg/m^{2}s) is replaced by the particle number flux at the wall, N_{wall} (N_d/ m^{2}s) and the mass concentration of particles in the bulk flow, $C_{p,bulk}$ (kg/m^3) is replaced by particle number concentration, $N_{d,,bulk}$ (N/ m^3).

Calculation of deposition velocity is thus obtained as

$$V_{dep} = \frac{N_{wall}}{N_{d,bulk}} \tag{4.21}$$

It is expected that particle deposition in the 2D straight duct will mainly arise from the interaction of particles with turbulent eddies. This is because the main flow of air is in the axial direction of the duct, and the particles have to reach the side walls either by diffusion or turbulent impaction.

As the experimental data in literature for particle deposition in the straight duct is obtained from fully developed turbulent flow, it is important to carry out the CFD simulation under identical conditions. Figure 4.7 and 4.8 show the velocity and turbulent kinetic energy profiles along the axial direction of the flow in the 2D duct. It can be seen that velocity magnitude reaches fully developed state at approximately 0.3 m downstream of the inlet, a length of about 15 D. The turbulent kinetic energy continues to develop up to the axial direction of 0.6 m. For this reason, the region of interest for calculating particle deposition rate should be at least 0.6 m away from the inlet for the fully developed condition to be satisfied. The particle deposition velocity and relaxation time were calculated from Equations 4.21 and 4.20.

The results are expressed in the conventional plot of dimensionless particle deposition velocity versus dimensionless particle relaxation time in Figure 4.9. Also shown in Figure 4.9 is the experimental result from Liu and Agarwal (1974).

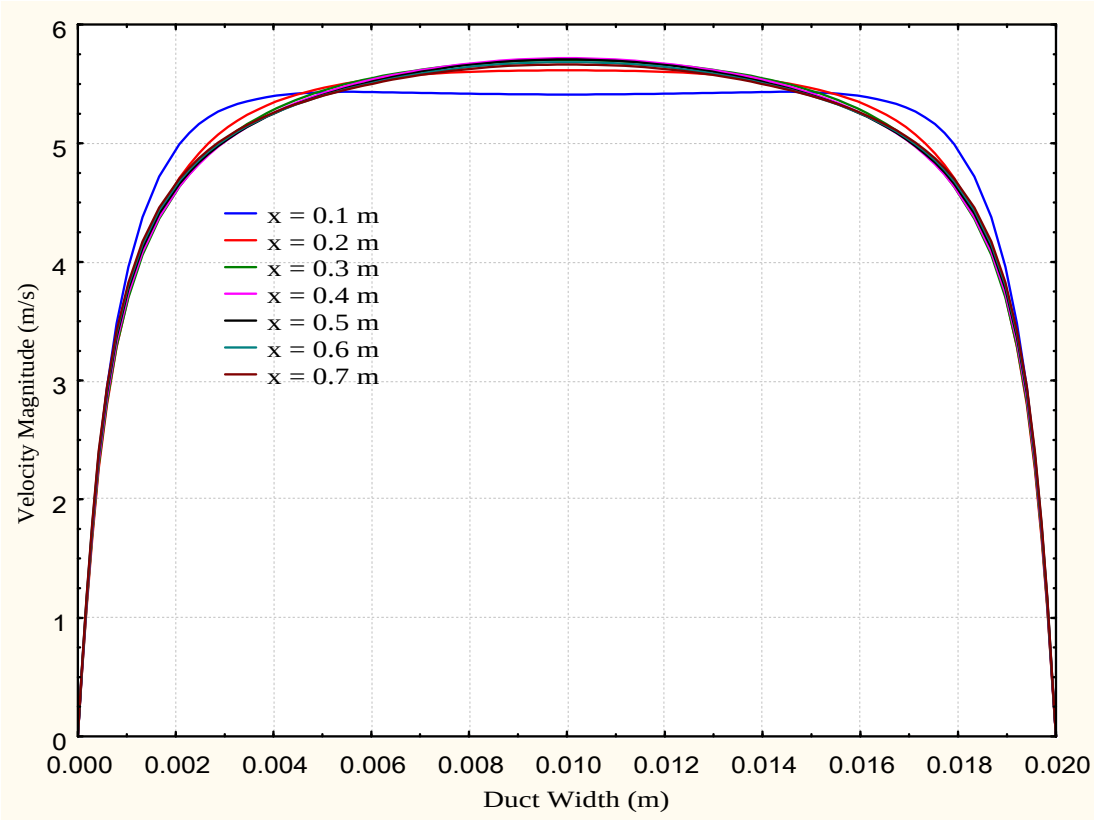

Figure 4.7 Plot of velocity magnitude along the width of the duct.

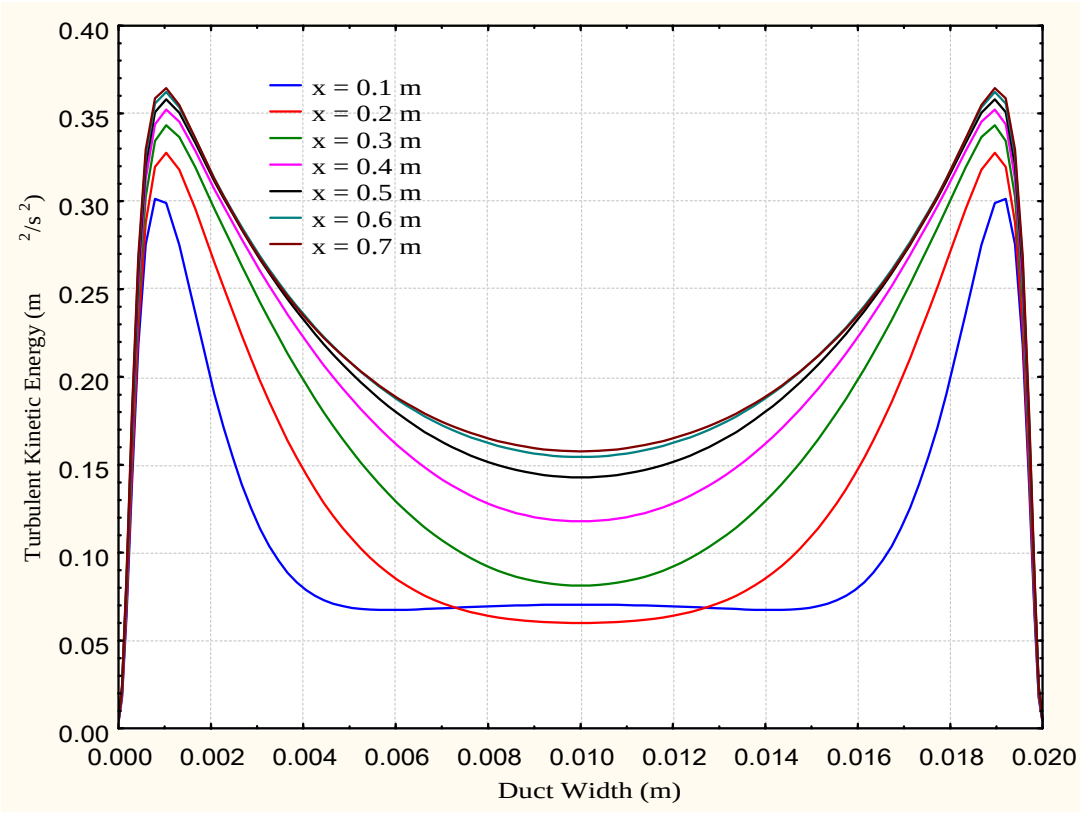

Figure 4.8 Plot of turbulent kinetic energy along the width of the duct.

Particle deposition data from Liu and Agarwal (1974) falls under the diffusion-impaction and inertia moderated regimes, as in by Figure 4.9. Their experimental data is considered one of the best available in the literature and the agreement between the CFD modeled and their results is very good. The simulated particle deposition rate has slightly overestimated the particle deposition in the range of τ_p^+ from 1 to 10. It has predicted the increase in deposition velocity with increasing particle size in the diffusion-impaction regime very well. It has also correctly predicted the decrease in deposition velocity with further increase in particle size. The results obtained are similar to those found by Tian and Ahmadi (2007), who evaluated a range of turbulence models for particle deposition prediction purpose.

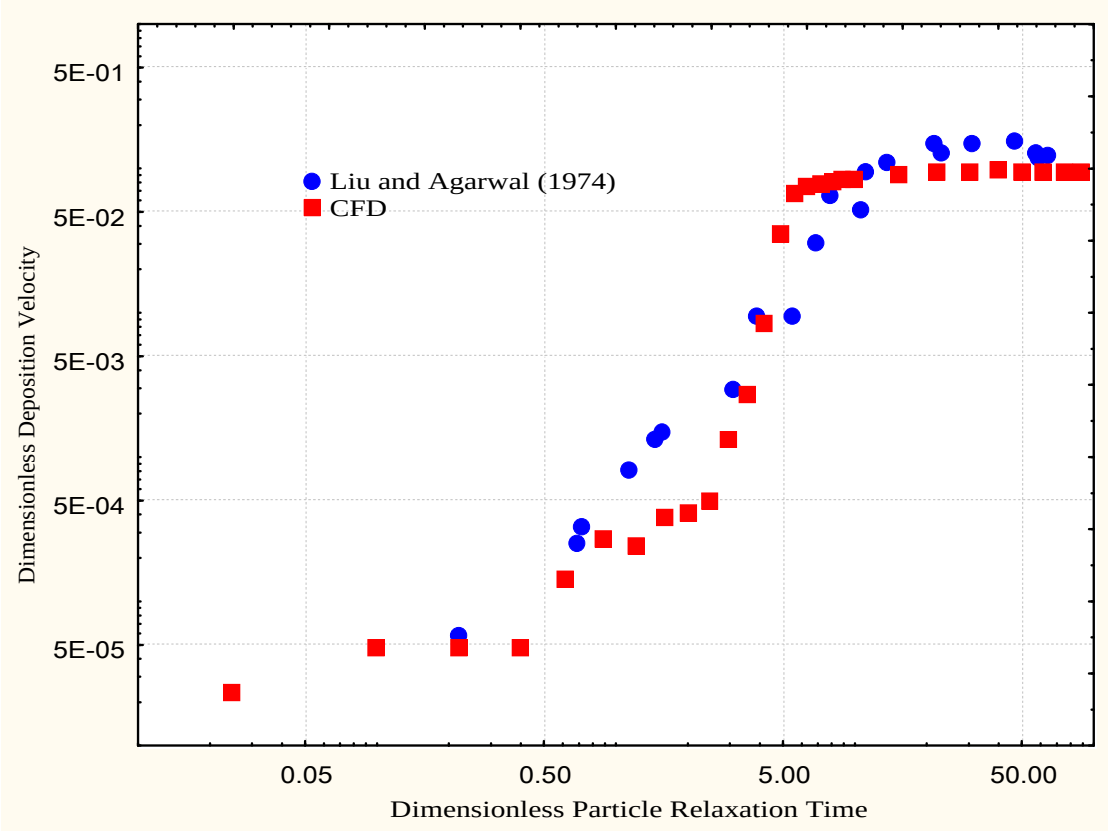

Figure 4.9 Comparison of particle deposition results from CFD and literature experimental data.

It should be noted that while turbulence models based on the RANS equations tend to overestimate the deposition rate of particles, this is only significant for τ_p^+ <1, corresponding to a particle size of around 7 μm in this study. Tian and Ahmadi (2007) concluded that the deposition rate of particle larger than 10 μm, which falls under the inertia-moderated regime, is affected by the turbulence fluctuation level to a lesser extent and therefore is less sensitive to the choice of turbulence models. Their study has shown that even the $k-\varepsilon$ model has yielded results in reasonably good agreement with experimental data.

4.5 CONCLUSION

In this chapter, an introduction is given on the basic principles of Computational Fluid Dynamics together with the continuity and Navier-Stokes equations. Turbulence modeling has been briefly reviewed. The main particle transport mechanisms responsible for particle deposition have been identified and discussed. A viable method of numerical modeling of particle deposition with Fluent has been validated and discussed with a case study of particle deposition from turbulent flow in a straight duct. It needs to be pointed out that the default wall boundary condition, i.e. trap condition, is able to predict the net collision rate of particles with the boundary surface in a flow domain. However, it does not take into account the particle-surface interactions. From the experimental study with the particle gun rig reported in Chapter 3, it has been shown that particle rebound contributes significantly to the deposition results. Therefore in the next chapter, a detailed discussion will be given on the development of such a wall boundary model for prediction of skim milk powder deposition.

CHAPTER 5 - USE OF CFD TO MODEL PARTICLE GUN RIG AND DEVELOPMENT OF WALL BOUNDARY CONDITION

5.1 INTRODUCTION

In Chapter 3, parameters that affect the results of the particle gun test have been studied. It has been shown that these results are dependent on the specific geometry of the equipment as well as the fluid dynamics governing the operating conditions. Thus, they only represent the behaviours of the depositing particles under certain specific conditions. In Chapter 4, a brief review of the application of Computational Fluid Dynamics (CFD) in studying particle deposition has been given. This chapter now combines the understanding from both these chapters to develop a three dimensional CFD model of the particle gun test, with the aim of using the model to predict the milk powder deposition process in pilot and industrial scale situations.

Past works on the particle gun rig have identified the contributions from the effects of air flow, such as the air velocity and H/D ratio. It has been realized in this work that the setup of the particle gun rig has all the features of an impingement jet. It is hoped that existing body of knowledge on impingement jet will help to better interpret the particle gun results.

5.2 PARTICLE GUN AS IMPINGEMENT JET

Operation of the particle gun rig involves the particle-laden air jet impinging orthogonally onto the plane wall. As in pipe flow, impingement jet flow can be classified as laminar, transitional or turbulent depending on its Reynolds number. A fully turbulent impingement jet exists when the Reynolds number ($\mathrm{Re} = \rho UD / \mu$) is greater than 3000 and for 1000 < Re < 3000, the flow regime is semi-turbulent (Viskanta, 1993). The flow regime in this numerical study falls under the fully turbulent state, where Re = 5670 for air velocity at 10.3 m/s.

Figure 5.1 shows the schematic diagram of a typical impingement jet. The structure of the flow can be divided into three different zones (Burwash *et al.*, 2006; Jambunathan *et al.*, 1992):

(1) *Free Jet Zone / Developing Zone*

(2) *Impingement Zone*

(3) *Radial Wall Jet Zone*

At the exit of the long pipe, the flow profile would have obtained that of the fully developed flow. The center line velocity is at its maximum and the velocity falls off rapidly in the direction of the wall due to the no-slip condition. The jet from the pipe then discharges into the ambient air and stationary fluid from the surroundings is entrained into the jet and this mixing action further reduces velocity at the sides of the jet. Up to H/D = 4, the free jet still has a potential core region, which is characterized by a more or less radially independent velocity profile. Further away from the pipe exit between H/D = 4 and 8, the jet starts to widen significantly with its average velocity declining further. In the meantime, the shearing action between the fast moving jet flow and stationary surrounding air will give rise to turbulent eddies known as ring vortices. Eventually the potential core will disappear after about H/D = 8 and the jet flow is said to be fully developed.

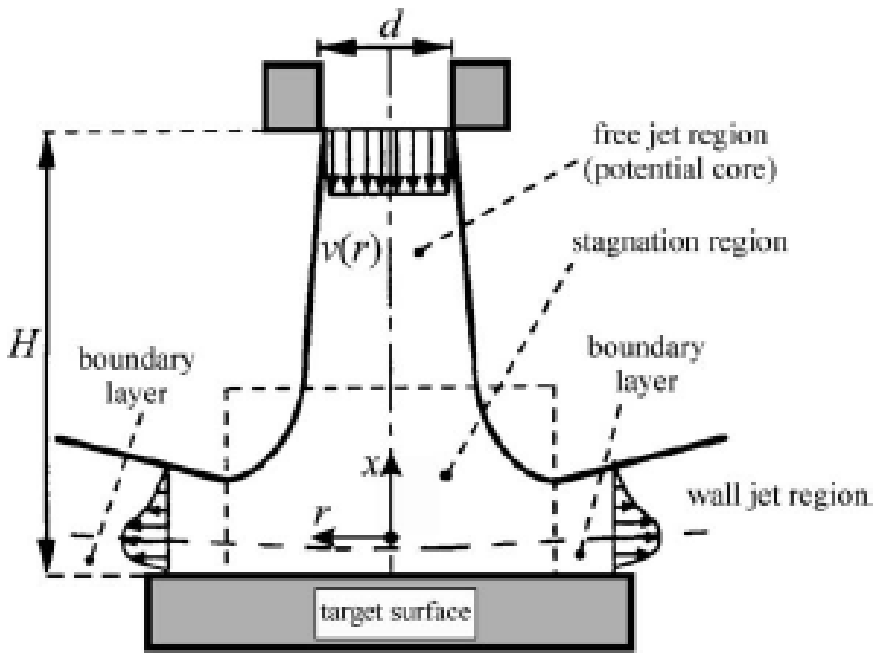

Figure 5.1 Structure of an impingement jet flow, taken from Angioletti *et al.* (2005).

As the jet moves towards the target wall, its momentum is reduced, accompanied by a rise in its static pressure. The thickness of the impingement zone has a typical value from 1.2 to 2 pipe diameters. The ring vortices generated earlier on in the process is still present and also strikes the wall. With the exception at the jet centre, streamlines of the jet begins to diverge and curve as the boundary layer effect of the target wall forces the jet flow in the radial direction. The radial wall jet zone contains very thin but fast-moving, accelerating boundary layers. At the centre of the impaction surface, there is a region corresponding to about one pipe diameter where the radial velocity magnitude and turbulence level are the lowest. This region is termed the stagnation zone. Away from the stagnation zone in the radial direction, the wall jet flow starts to accelerate and turbulence level is much higher compared to other parallel flow such as pipe flow.

From the description of the main characteristics of the impingement jet, it can be concluded that the particle gun rig falls under this category and should be treated as

such. It has been discussed that the distance between the pipe exit and the target wall can have a major impact on the resultant impingement jet characteristics. Past works on the particle gun rig has used an H/D ratio of 20, under which condition the jet would have developed and diverged significantly before impinging. This would have resulted in a much lower average jet velocity compared to that at the pipe exit, which would have in turn reduced the velocity of the particles entrained in the jet. The velocity of deposition is therefore not the velocity at the pipe exit as generally reported and a more detailed analysis is required to determine the correct deposition velocity.

A large H/D ratio is also undesirable because there exists a possibility that the temperature and RH of the jet will have changed as the jet moves further away from the pipe exit. This is supported by the fact that the ambient, stationary air that would have been entrained into the jet is also much colder (ambient air was around 15 – 18 °C). This cooling effect may be more significant for the lower velocity range employed in this study, as compared to the 20 - 50 m/s used by researchers from Massey University. Attempts to measure the temperature of the air close to the impingement plate have proven to be difficult in this experiment. Pt100 temperature sensor has been taped onto the plate but the large surface area of the probe in contact with the plate may have resulted in significant heat conduction, leading to results consistently close to the ambient temperature. Improving the design of the particle gun rig to allow measurements of temperature and velocity can be an area for further research.

In terms of numerical modelling, a smaller H/D ratio would require a much smaller mesh size and thus it is more computationally efficient. For all the above reasons, this study has used an H/D ratio of 4 rather than 20.

5.3 CFD MODELLING OF SINGLE-PHASE IMPINGEMENT JET

5.3.1 Computational Domain

The commercial CFD package Fluent 12 and Gambit 2.4 have been used for modelling the particle gun in this study. The computational domain used for the investigation of the impingement jet is shown in Figure 5.2. This setup resembles closely with the experimental rig used in the lab. The air jet enters the domain at the top and issues from an 800 mm long round pipe with an internal diameter of 11 mm. The target wall is rectangular in shape and measures 164 mm × 136 mm. To properly model the interaction of the jet flow and surrounding ambient air, it has been recommended that the outer radial boundary of the domain should be sufficiently large (ERCOFTAC database). In this case, the outer boundary enclosing the impingement jet and target wall is 328 mm × 272 mm, or at a radial distance of r/D = 15. This arrangement ensures that the numerical solution is not affected by the presence of the boundary. The spacing between the pipe exit and the target wall is 44 mm, corresponding to an H/D ratio of 4.

5.3.2 Meshing and Grid Independence

A combination of structured and unstructured grid has been used for meshing the computational domain. Figure 5.3 shows a slice of the mesh across the x-y plane of the domain. It is seen that the nodes are more concentrated towards the core of the plane as a finer mesh is required to capture the change in velocity gradient and turbulence for the flow in the pipe as well as the jet flow once the air exits the pipe.

Nodes are also accumulated near the walls of the pipe and target wall so that the wall y^+ value is around 1. To mesh the entire domain, the face mesh shown in Figure 5.3 is extruded in both the positive and negative Z directions.

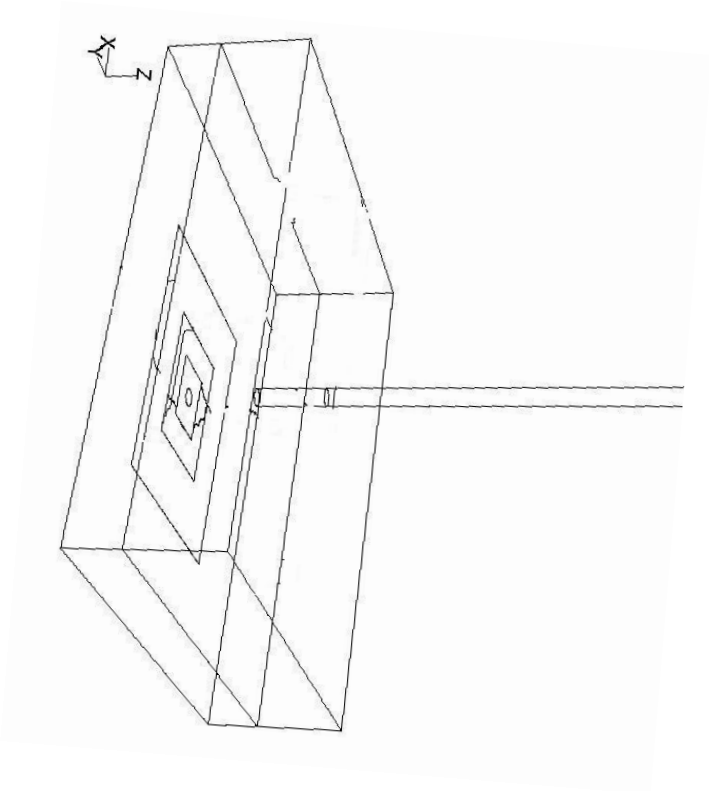

Figure 5.2 Computational domain of particle gun.

A finer grid size is imposed for the negative Z direction towards the target wall, as this is the region where the most intense mixing of the jet flow and ambient air occurs. The effect of the mesh size on the numerical solution is investigated by varying the grid points in the Z direction, resulting in 1,827,857, 4,351,695 and 6,011,342 cells respectively.

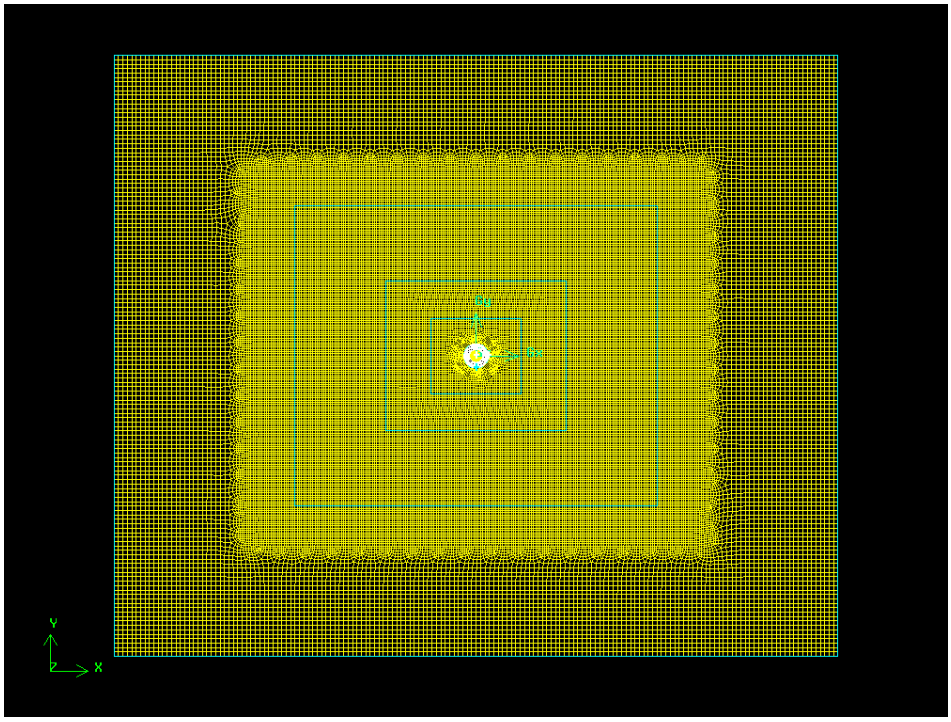

Figure 5.3 Mesh of the computational domain in the x-y plane.

5.3.3 Turbulence Models, Boundary Conditions and Solution Control

The $k-\omega$ shear stress transport (SST) model has been selected as the turbulence model for the present investigation. Craft *et al.* (1993) has investigated the modelling accuracies of a range of turbulence models for the impingement jet flow. The popular low-Reynolds-number $k-\varepsilon$ model has been found to produce excessive turbulence energies that over-predicted experimental values by up to four times. The more elaborate, 7-equation basic Reynolds-Stress model also fared no better due to its sub-model of "wall-reflection" term. The $k-\omega$ SST model has been found to give a reasonable prediction of the impingement jet flow field and heat transfer characteristics (Angioletti *et al.*, 2005). It is also the model of choice for studying particle-laden impingement jet and particle deposition behavior (Burwash *et al.*, 2006).

A constant velocity profile across the pipe inlet is used as the inlet boundary with a

velocity magnitude of 4.5 m/s normal to the inlet and 5% turbulence energy. A pressure outlet boundary condition with gauge pressure set at 0 pascal is imposed for all the boundary surfaces enclosing the computational domain. No-slip condition is selected for all wall boundaries. Gravity has been enabled in the negative Y direction, in accordance with the actual experiment.

The SIMPLE algorithm is used for Pressure-Velocity Coupling. Second-order upwind scheme is used for the spatial discretisation of momentum, turbulence kinetic energy and specific dissipation rate and the second-order scheme is used for the pressure term. Iteration is performed, with no specific convergence criterion imposed. The solution is considered to have converged when the residuals have obtained a static value. The final levels of residual are typically on the order of 5e-08 for all terms. The computational time for the different CFD cases used is approximately 200 CPU hours.

A CFD inlet velocity of 4.5 m/s was used rather than the higher velocity of 10.3 m/s because when the CFD modelling was done the lowest experimental velocity was thought to be 4.5 m/s. At the end of the project Particle Image Velocimetry analysis of the impingement jet was done by another researcher, and the anemometer readings were shown to be out by a factor of 2.3, which corresponds to the anemometer to jet area ratio. Unfortunately due to time constraints, the CFD work has not been able to be re-done for this thesis at the higher inlet velocity of 10.3 m/s.

5.3.4 Single Phase Impingement Jet Results

Figure 5.4 and 5.5 show the velocity magnitude and turbulent kinetic energy along the jet axis for the three mesh sizes simulated. The region covered is from the impingement point to the exit of the pipe. There is no significant difference in the velocity profile between the three cases. The velocity magnitude has an overall

declining trend towards the impingement plate, and this is more pronounced up to 0.01 m above the plate, which is about one pipe diameter. In terms of the turbulent kinetic energy, the mesh with 1.8 million cells is seen to underestimate the rapid rise close to the plate.

Figure 5.6 and 5.7 show the velocity magnitude and turbulent kinetic energy along a line parallel to the impaction surface and at a distance of Z = 0.1 D (0.0011 m) above the plate. The lowest velocity magnitude and turbulent kinetic are at the centre, and this is where the stagnation point is located. Away from the stagnation point, the velocity rises rapidly due to the acceleration of the radial wall jet. High turbulent kinetic energy is also seen to coincide with the wall jet development. It is expected that the controlling particle deposition mechanism in the stagnation zone is inertial impaction due to low velocity and turbulence. Turbulent diffusion may account for more deposition away from the impaction centre. It is seen from Figure 5.6 and 5.7 that the case with 1.8 millions cells has under-predicted both velocity and turbulence in the central jet region. For this reason, all subsequent modelling is carried out with the case of 4 million cells because a higher mesh count does not seem to produce any difference.

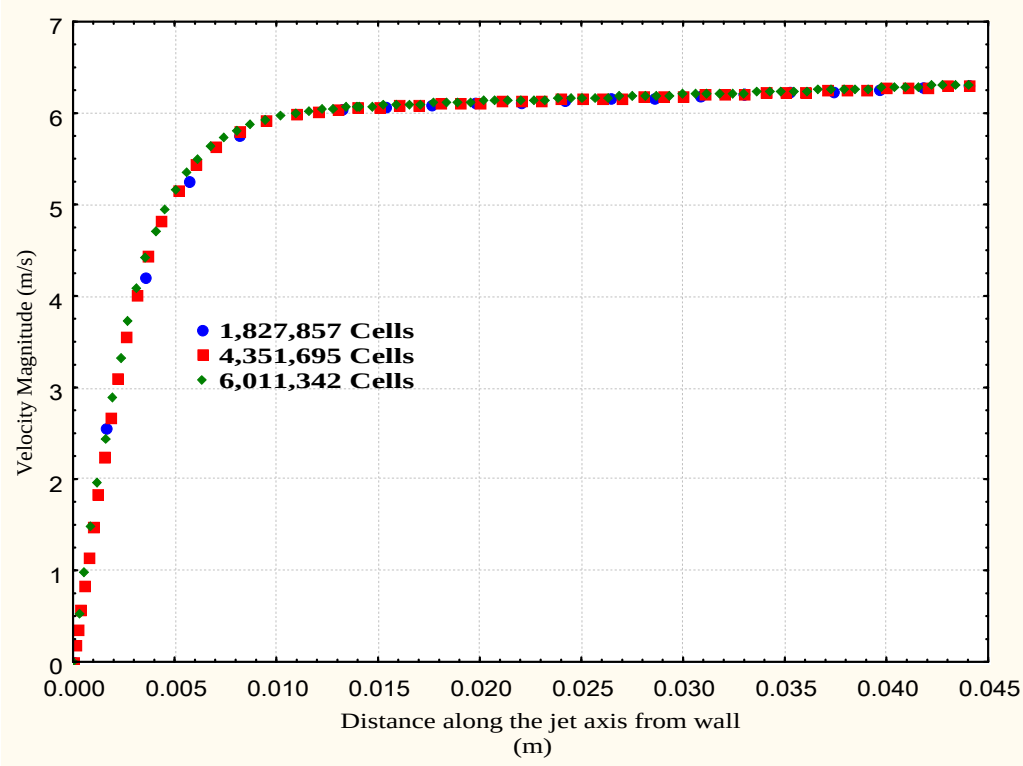

Figure 5.4 Profile of velocity magnitude along the jet axis from the impingement plate to the exit of the pipe.

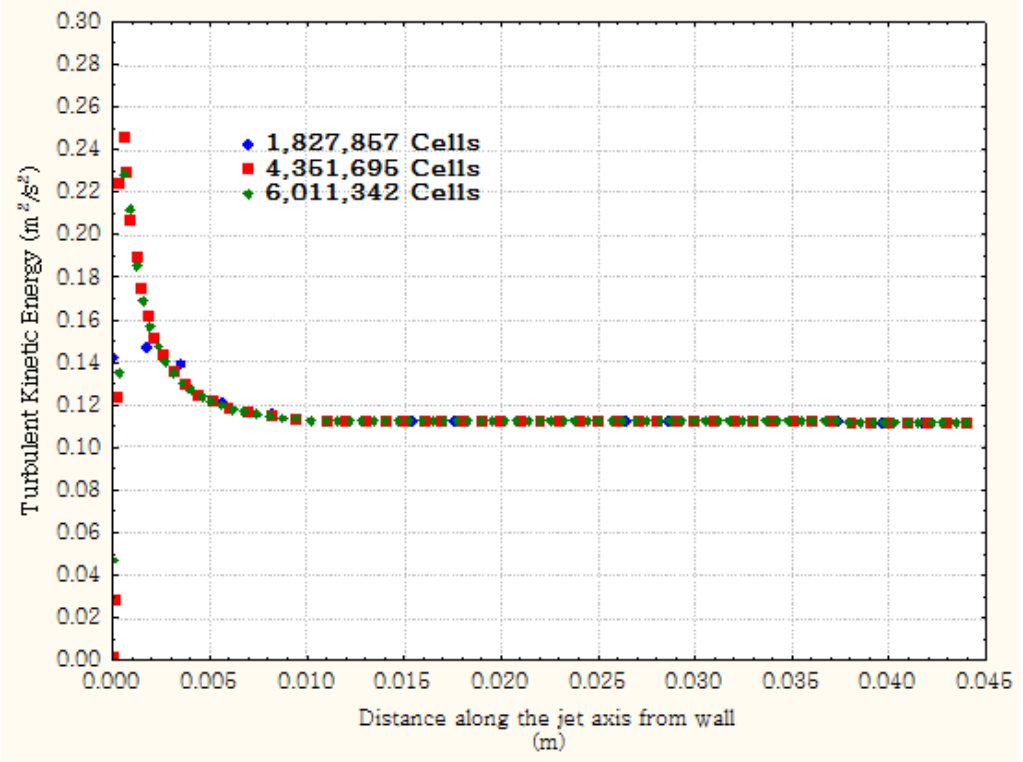

Figure 5.5 Profile of turbulent kinetic energy along the jet axis from the impingement plate to the exit of the pipe.

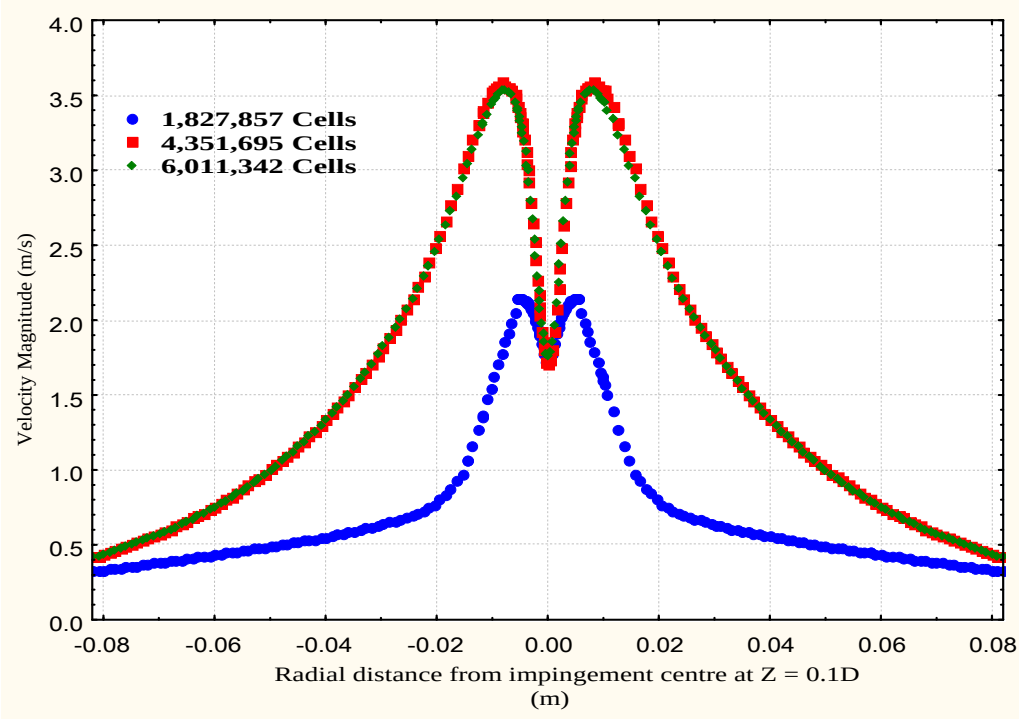

Figure 5.6 Profile of velocity magnitude along a line parallel to the impaction surface and at a distance of Z = 0.1 D above the surface.

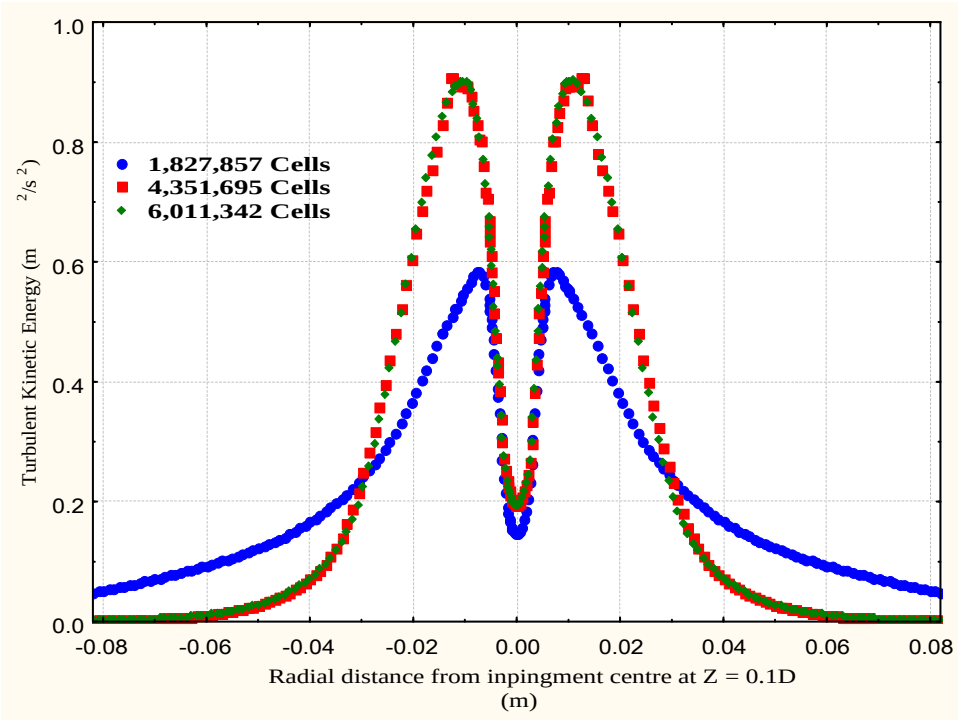

Figure 5.7 Profile of turbulent kinetic energy along a line parallel to the impaction surface and at a distance of Z = 0.1 D above the surface.

Figure 5.8 and 5.9 show a contour and vector plot for velocity magnitude from the pipe exit to the impingement plate. It can be seen that the jet has developed only slightly once exiting the pipe, with the jet width upon impaction at less than 16 mm. The high velocity region characterized by the red colour is the potential core, which still makes up a significant portion of the jet. This is expected due to the low H/D ratio of 4. Figure 5.10 and 5.11, cross-sectional planes to the surface of velocity magnitude, further illustrates the potential core velocity is reduced as the plate is approached. Outside the potential core at the jet periphery, the impinging wall jet starts to show curvature and develops into a radial wall jet. These characteristics are further illustrated by plots of normal and tangential velocities to the plate surface, as shown in Figure 5.12 and 5.13. Normal velocities above 1m/s are common only at radial distances of 10 mm from the centre of the plate. Tangential (radial) velocities then dominate with a maximum arising at a radial distance of 5 mm.

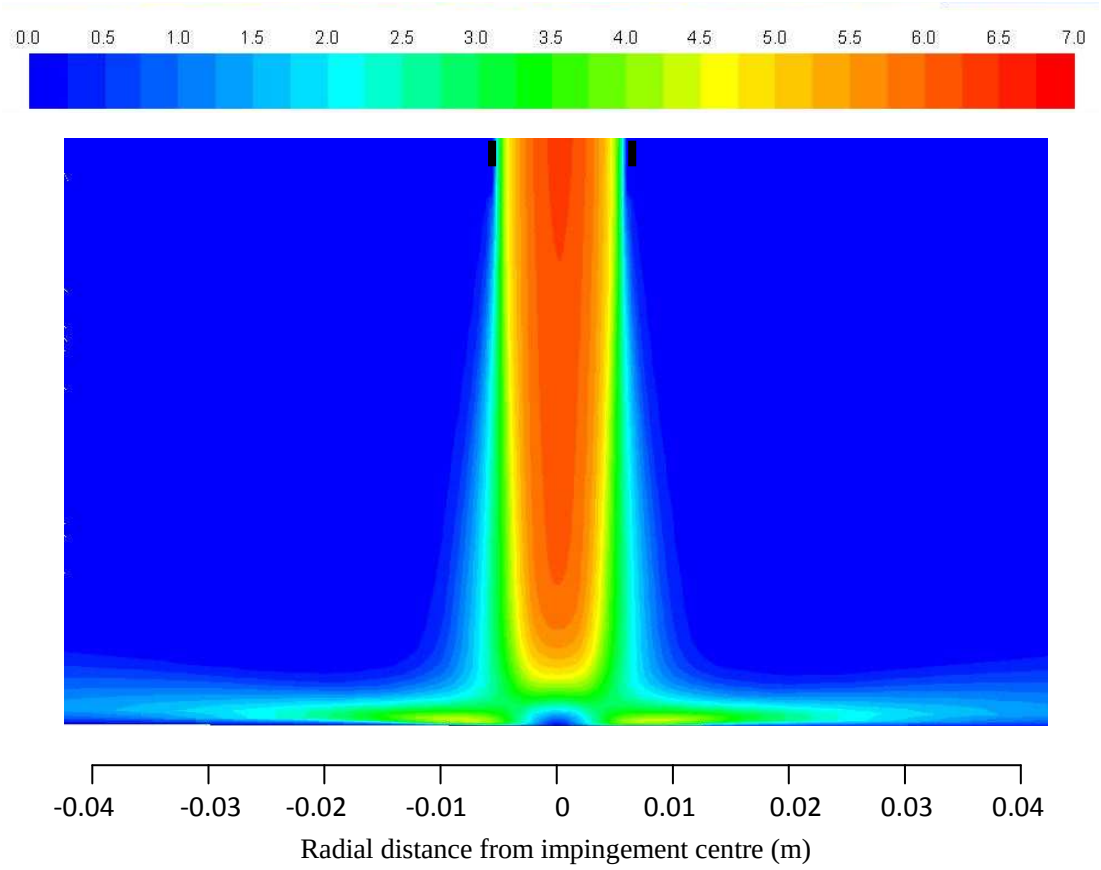

Figure 5.8 Contour of velocity magnitude (m/s) for the impingement jet.

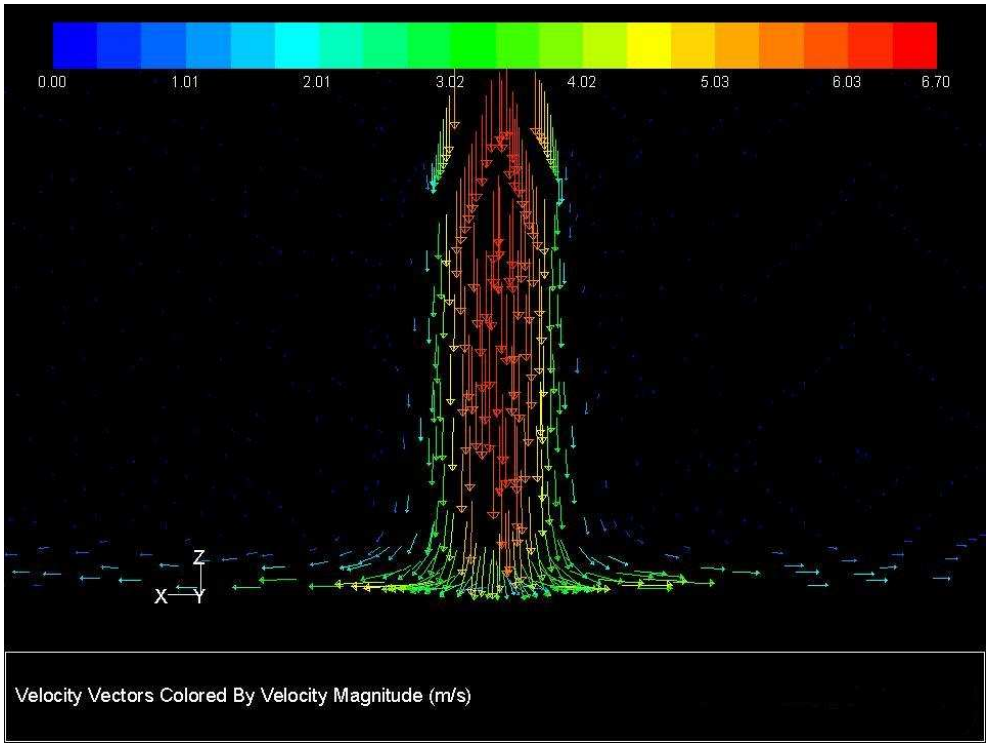

Figure 5.9 Vector plot of velocity magnitude (m/s) for the impingement jet.

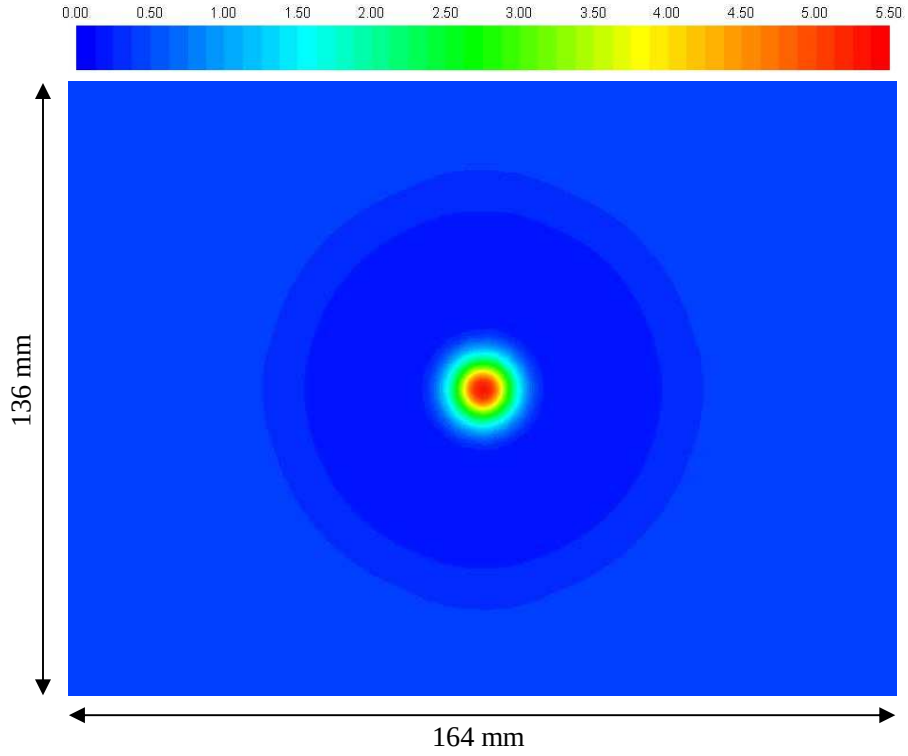

Figure 5.10 Contour of velocity magnitude (m/s) in a plane parallel to the plate at a distance of Z = 0.3 D, data extracted from CFD impingement jet

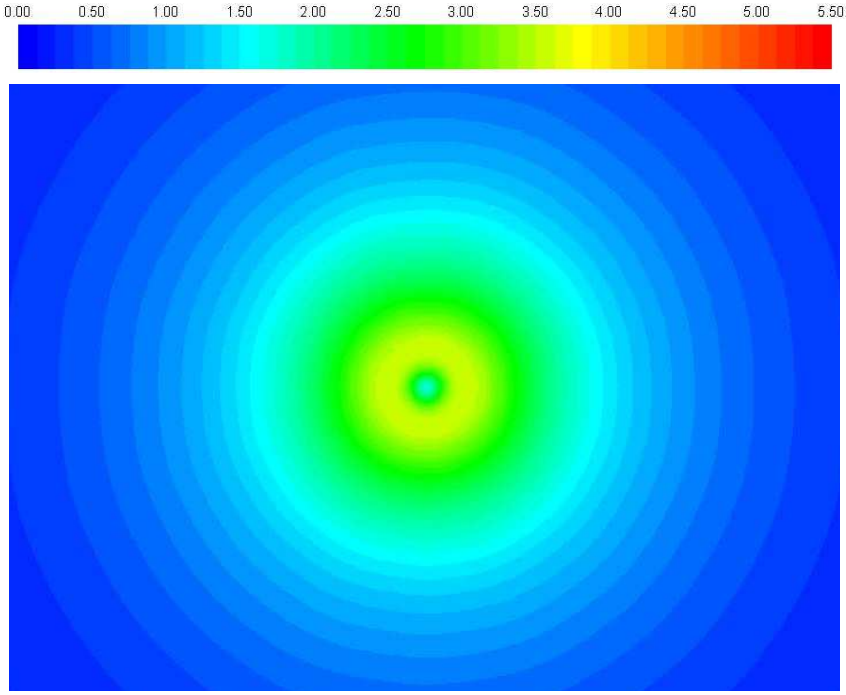

Figure 5.11 Contour of velocity magnitude (m/s) in a plane parallel to the plate at a distance of Z = 0.1 D, data extracted from CFD impingement jet

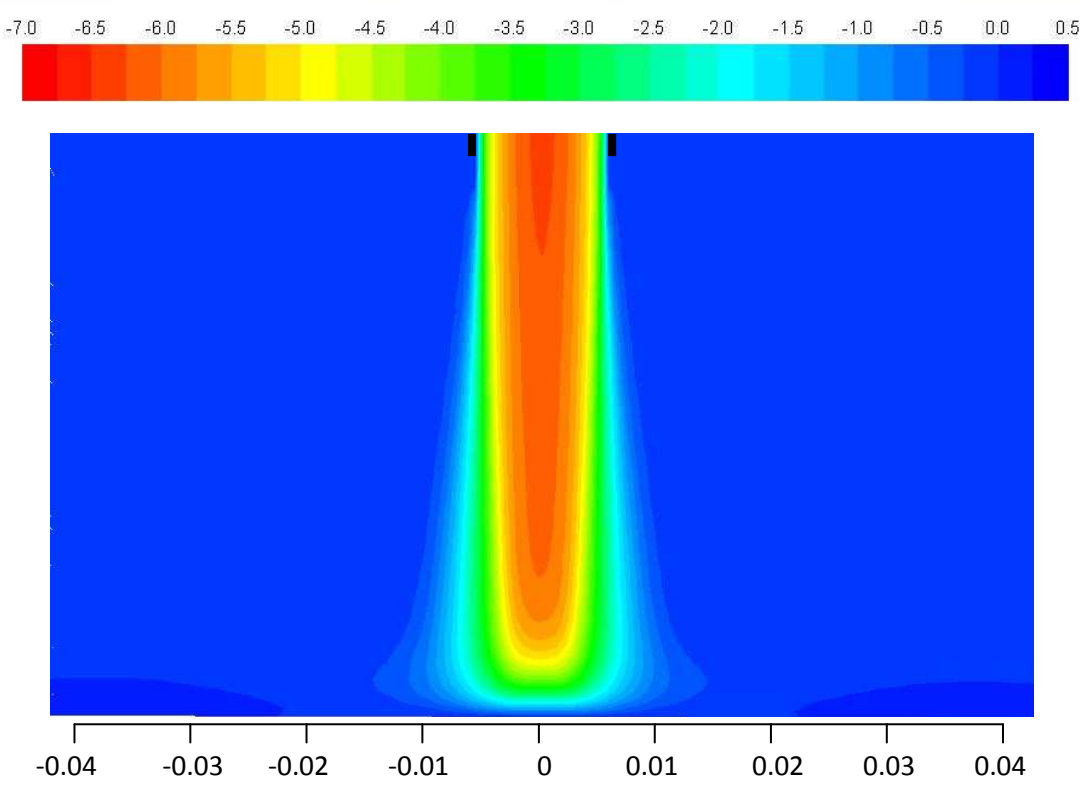

Figure 5.12 Contour of normal velocity (m/s) for the impingement jet.

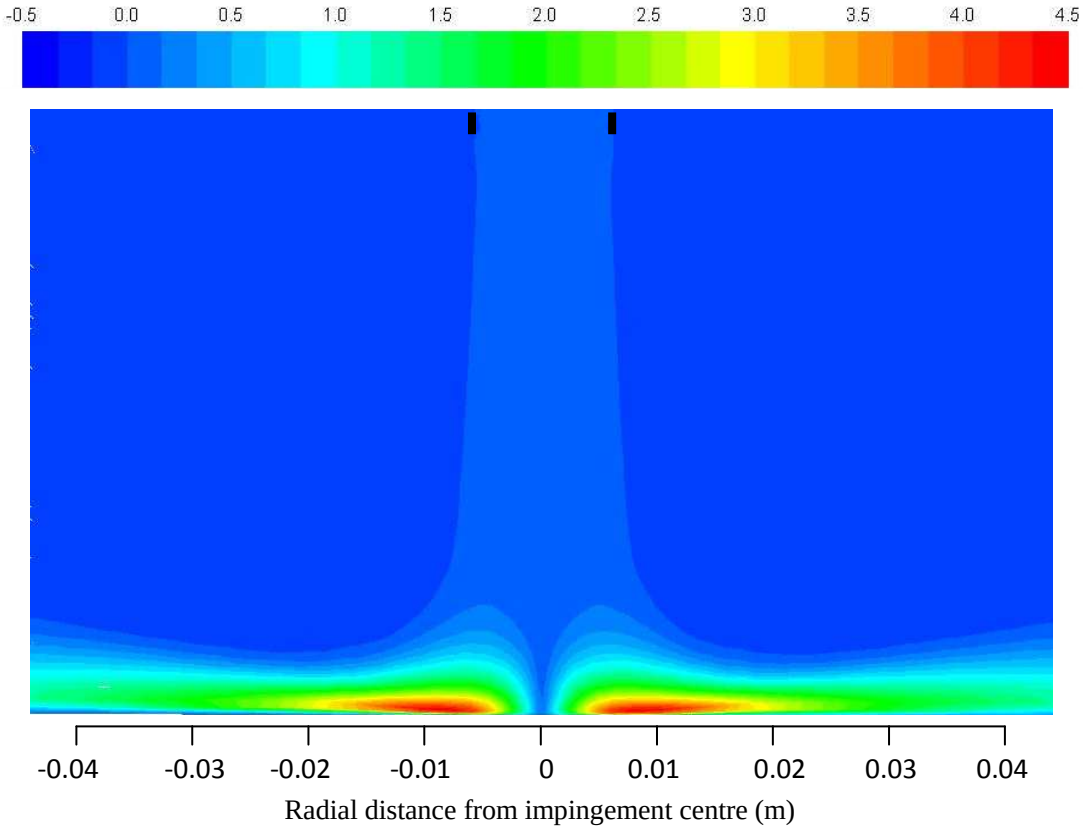

Figure 5.13 Contour of tangential velocity (m/s) for the impingement jet.

5.4 DAIRY POWDER SURFACE CONTACT DYNAMICS

Particle-surface contact dynamics is a very important but often overlooked issue in the subject of dairy powder deposition. In CFD modelling, it is essential to prescribe a wall boundary condition that can decide the fate of an impinging particle. It is important to know, under a specified condition, what portion of the impinging particles will eventually stick to the surface? The sticking probability of a single particle-surface collision event is either 0 or 1 (Konstandopoulos, 2006). The transition from particle rebound (sticking probability = 0) to particle capture (sticking probability = 1) occurs whenever the set of parameters governing the underlying collision process reaches a critical value. When considering an ensemble of particle collision events such as that in the particle gun rig, all of these individual collision outcomes will ultimately give rise to the % deposition measured experimentally. The particle gun experiment has shed light on the set of parameters that are responsible for skim milk powder deposition and rebound. It is desirable to fit a model to the experimental results and apply this model in CFD modeling.

A number of studies have looked at behaviour of impaction and rebound for non-dairy particles (Bitter, 1963; Rogers and Reed, 1984; Wall *et al.*, 1989). It has been found that particles rebound when the incident velocity is greater than a characteristic critical velocity. This critical velocity is dependent on the specific material properties of the particles and the surface. The theory can be best explained with the help of Equation 5.1, which is taken from Xu and Willeke (1993).

$$E_r = E_i - (E_{ad} + E_{pd}) \qquad (5.1)$$

Equation 5.1 is the same as Equation 3.2, and is presented again here. It represents the energy balance of a particle-surface collision event.

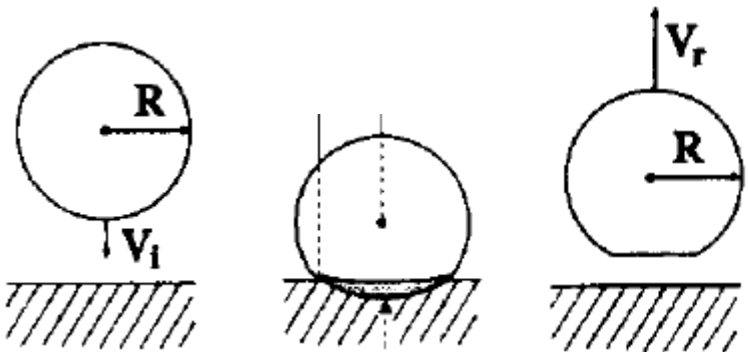

(a) (b) (c)

Figure 5.14 Process of particle-surface collision, adapted from Xu and Willeke (1993).

As shown in Figure 5.14, The particle will approach the surface with velocity V_i, and incoming kinetic energy E_i, $E_i = \frac{1}{2} m V_i^2$. During the contact phase, the energy of the particles is dissipated due to both the work of adhesion (E_{ad}) as well as plastic deformation (E_{pd}). Plastic deformation at the particle surface is permanent and the deformed particle will rebound from the surface with velocity V_r, if it still has excess energy left. Describing both the incoming and rebound kinetic energy of the particles in terms of their mass and velocity, Equation 5.1 can be written as

$$\frac{1}{2} m V_r^2 = \frac{1}{2} m V_i^2 - (E_{ad} + E_{pd}) \tag{5.2}$$

or

$$V_r = \sqrt{V_i^2 - \frac{2(E_{ad} + E_{pd})}{m}} \tag{5.3}$$

Equation 5.3 shows a number of important features. It can be inferred that whether the particle sticks to or rebounds from a surface will result from the competition between the available incoming kinetic energy and energy dissipation mechanisms. The energy

dissipated is increased for a higher work of adhesion and plastic deformation, but reduced for a smaller particle size or mass. At the same level of energy dissipation, an increase in particle impinging velocity will lead to a higher particle rebound velocity.

Most of the important effects uncovered from the particle gun experiments can be explained with Equation 5.2. The basic feature of the particle gun result is a linear increase in the % deposition with increasing levels of $T\text{-}T_g$. It is known that with increasing $T\text{-}T_g$ the particle surface viscosity will reduce which helps stronger liquid bridges to form. This essentially increases the energy loss due to the work of adhesion, E_{ad}. Similarly, particles with higher moisture content are more likely to deposit (Murti, 2006). This can be explained by the increasing softness and thus the increase in the plasticity term E_{pd}. It has been shown in Section 3.4.3 that an increased particle gun tip velocity will increase the $(T\text{-}T_g)_{critical}$ and decrease % deposition at all levels of $T\text{-}T_g$. Equation 5.2 shows that at a higher V_i while other factors are constant, the particles are more likely to rebound. Similarly, the effect of particle size reported in Section 3.4.4 and summarised in Figure 3.15 can also be explained by Equation 5.3 or 5.5. With smaller diameter particles (lower mass), the $(T\text{-}T_g)_{critical}$ reduces at the same V_i.

In the event of particle capture, where $V_r = 0$, Equation 5.3 can be reduced to

$$V_i = V_{cr} = \sqrt{\frac{2(E_{ad} + E_{pd})}{m}} \tag{5.4}$$

or

$$\frac{1}{2} m V_{cr}^2 = E_{ad} + E_{pd} \propto \mathrm{T} - \mathrm{T_g} \tag{5.5}$$

Equation 5.4 represents the case when the incoming particle kinetic energy is equal to the energy dissipation. The velocity at which this occurs is termed the critical velocity

for particle deposition, V_{cr}. In practice, particles will also be captured if $V_i < V_{cr}$. When V_i is greater than V_{cr}, rebound occurs and the greater the V_i exceeds V_{cr}, the higher the coefficient of restitution.

The critical velocity for particle rebound has been measured experimentally in a number of cases. Wall *et al.* (1990) has used Laser Doppler Velocimetry for measuring the rebound velocities of ammonium fluorescein particles impacting on targets made of a variety of materials. van Beek *et al.* (2006) studied the impact behaviours of 50 μm particles on a powdery surface with a high speed digital camera system (Figure 5.15).

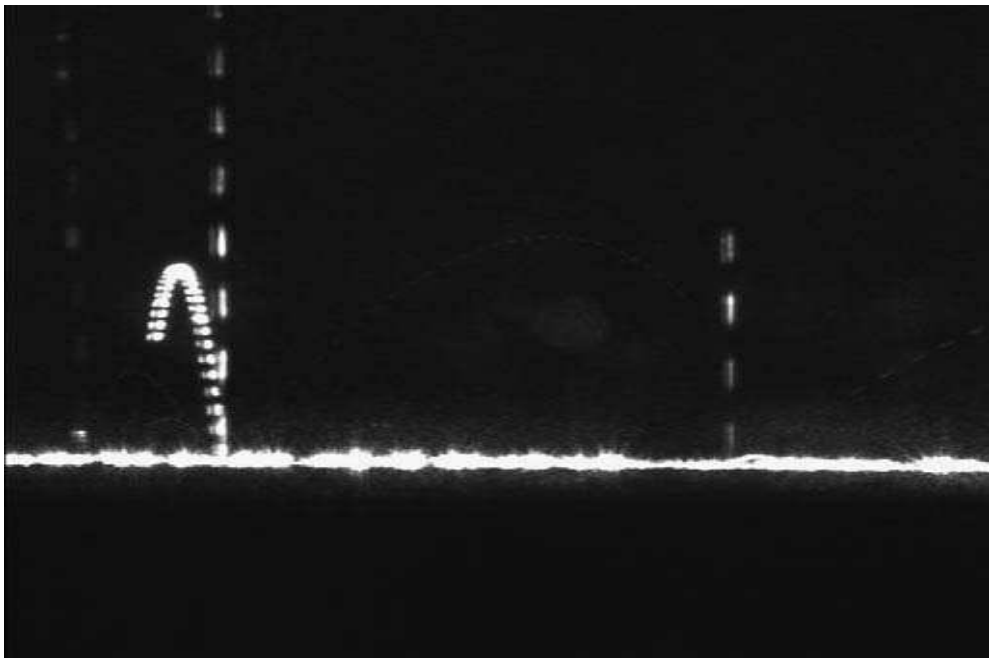

Figure 5.15 Particle impact and rebound behaviour studied by high speed camera, taken from van Beek *et al.* (2006).

Due to time and resource constraints in this study, no attempt has been taken to carry out such a study. The newly acquired Particle Image Velocimetry instrument at the University of Waikato offers a promising experimental method that can be potentially used to augment the particle gun rig for this purpose. However, a number of problems may exist. Experiments studying impact and rebound behaviours of particles are

typically carried out in a vacuum column. This is because researchers are often only interested in the particle-surface collision process itself. The presence of air or other gases will cause lift and drag effects that will mask the coefficient of restitution measured. In the case of dairy powder deposition, a vacuum environment is not practical as the temperature and humidity effect can only be imparted by a gas medium. Secondly, the critical rebound velocity has been shown to be particle size dependent. Practically it is difficult to obtain dairy powders of a uniform particle size distribution from manufactured powders. The sieving procedure adopted in this study can reduce the particle size distribution to a certain limit, but the resultant particles are still far from uniform. Recently, researchers from Monash University (Patel, 2008) have reported promising results on laboratory single stream particle drying procedure that is capable of producing identical particle sizes. Lastly, the proposed critical velocity for dairy powder deposition will cover a range of values depending on the $T\text{-}T_g$ condition. This is because Equation 5.3 shows that V_{cr} is directly proportional to E_{ad}, which is in turn dependent on $T\text{-}T_g$. As a result the deposition of dairy powders are more complicated as compared to non-dairy powders such as metal powder, whose surface adhesion only relies on van der Waals forces, which are constant (Xu and Willeke, 1993).

5.5 DEVELOPMENT OF A SKIM MILK POWDER DEPOSITION WALL BOUNDARY MODEL FOR CFD

5.5.1 Discrete Phase Modelling

Particles are tracked in the flow domain in the Lagrangian framework. The Fluent Discrete Phase Model (DPM) is used for this purpose. The particles are chosen to be inert, with a particle density of 1140 kg/m^3 (Murti, 2006). One-way coupling between the particle and the carrier phase is assumed. The experimental particle feed rate of 0.05 g/s results in a particle to air volume fraction of 0.01% is used in the CFD model. These conditions fulfil the one-coupling requirement of less than 10%.

5.5.1 Default Wall Boundary Conditions in Fluent

There are a number of default wall boundary conditions for particle-wall interactions offered in commercial CFD packages such as Fluent and CFX. These are trap, escape and reflect. The trap and escape options are essentially the same for inert, non-reacting particles. Once the particle touches a bounding surface with either of these two options turned on, the calculation for the trajectory of the particle is terminated. With the reflect option, CFD users are able to define the rebound velocity of the particles as a function of the impingement angle and coefficient of restitution. In addition to these default options, users can also formulate their own boundary conditions through the User-Defined-Function (UDF) offered by Fluent.

The trap/escape boundary condition is in fact a reflection of the rate of particle collisions taking place between the particles and boundary surface. In this case, it also gives a good estimate for the scenario where the particles are infinitely sticky, i.e. at

very high level of $T\text{-}T_g$. The use of the trap/escape condition has been adopted in CFD studies simulating particle deposition in straight pipe and human airways. In such studies, either the wall surface has been made sticky deliberately by coating adhesives on the surface or the particles have been made sticky by using viscous oil droplets. However, this option is not realistic for simulating dairy powder deposition. It has been observed experimentally in the particle gun study that the sticking propensity (% deposition) is a strong function of $T\text{-}T_g$. Accompanying this rise in % deposition with increasing levels of $T\text{-}T_g$, there is also a evolution of the deposition morphology as shown in Figure 3.9 in section 3.4.1. Thus, the trap/escape boundary condition only represents the most extreme case in which the particle sticking propensity is the highest.

5.5.2 Improved Wall Boundary Conditions in Literature

Recognising the limitations of the trap/escape boundary conditions, researchers studying dairy powder deposition have sought to come up improved models. In a CFD study on the effect of dryer chamber configurations on spray drying performance, Huang *et al.* (2003) has used a “reflect” condition for the dryer wall. In addition, the coefficient of restitution has been set to zero for both the normal and tangential components. However, a reflect boundary condition means that the particles will never be captured and thus do not deposit. Although all of the kinetic energies of the impinging particles are lost, they can still extract momentum from the boundary layer air flow and also experience the effect of gravity. Eventually, all particles injected into the computational domain will leave the outlet and no information regarding deposition is obtainable.

In a similar study, Harvie *et al.* (2002) applied a wall boundary condition based on the sticky point concept, i.e. $(T\text{-}T_g)_{critical}$. The value of $(T\text{-}T_g)_{critical}$ chosen is 23.3 °C for

skim milk powders, as recommended by Hennigs *et al.* (2001). This value is obtained with the stirrer stickiness test, which records the critical $T\text{-}T_g$ value that stops the movement of the stirrer shaft inserted into a powder bed and rotating at a constant speed. Hennigs *et al.* (2001) has recommended the incorporation of the result into CFD code to model the build up of wall deposits. They also suggested that for conditions resulting in $T\text{-}T_g < 23.3$ °C, the particles can be considered to bounce off the wall but stick to the wall if $T\text{-}T_g > 23.3$ °C. Harvie *et al.* (2002) have implemented this approach in their CFD modelling of a tall form spray dryer. For $T\text{-}T_g < 23.3$ °C, the particles are set to rebound from the wall elastically, i.e., coefficient of restitution =1. For $T\text{-}T_g > 23.3$ °C, the coefficient of restitution for impinging particles is set to zero and if the rate of moisture evaporation for the particles is less than 0.001 s^{-1}, the particles are considered to be captured. For all the cases Harvie *et al.* (2002) have simulated, on average about 300 to 400 particles out of a total 2000 particles tracked end up sticking to the walls of the internal chamber as deposits. This amount of deposits corresponds to 15% to 20% of the total throughput and Harvie *et al.* (2002) have concluded that this criteria based on $(T\text{-}T_g)_{critical} = 23.3$ °C is too pessimistic. It has been shown in the particle gun experiments that the $(T\text{-}T_g)_{critical}$ only represents the condition at which the % deposition starts to increase significantly. This over-estimation in the extent of particle deposition obtained by Harvie *et al.* (2002) is very likely due to the fact that the model stipulates a 100% deposition for $T\text{-}T_g > 23.3$ °C, which is not the case.

Woo *et al.* (2008) have evaluated the accuracy of different drying models implemented in CFD simulation of spray dryer. They have also implemented a wall boundary condition based on the concept of critical velocity. To the best of the author's knowledge, this particular study is the only one that has implemented such an approach to determine the particle deposition propensity. Woo *et al.* (2008) have prescribed a critical velocity (V_{cr}) of 0.02 m/s and 8 m/s for particles and droplets, respectively. Particles are classified as having a moisture content less than 30%wt and droplets have a moisture content greater than 30%wt. The critical velocity criteria

used is based on the normal velocity component of the impinging particles, thus it can also be termed the critical normal velocity. In this approach, particles are considered to deposit if the normal velocity is less than 0.02 m/s. Otherwise, the particles will rebound from the surface with a restitution coefficient of 0.8. However, Woo *et al.* (2008) have not given any supporting evidence for the choice of critical normal velocity and coefficient of restitution. The material of interest to be spray dried in their study is a sucrose-maltodextrin solution. Although it is different from skim milk, it is believed its deposition behaviour will also be significantly affected by the $T\text{-}T_g$ condition (Foster, 2005), as sucrose has the same molecular weight as lactose. Thus, the single criterion also involves simplifying assumptions as the critical normal velocity is likely to change with varying $T\text{-}T_g$.

5.5.3 Development of Wall Boundary Condition

This section seeks to develop a CFD wall boundary condition for skim milk powder, based on the results from the particle gun experiment. Ideally, the model should have the following features:

(a) The model should be based on a kinetic energy balance model for the impinging particles.
(b) The model should be able to describe the increasing deposition propensity of SMP particles with increasing $T\text{-}T_g$ level.

(c) The model should be able to capture the evolving deposit morphology observed experimentally with increasing $T\text{-}T_g$ level.

The model is formulated according to Equation 5.2 and 5.5 and is based on the rationale that there exists one single critical velocity for particle deposition

corresponding to each level of $T\text{-}T_g$. A single particle size of 30 μm is used for most of the model development. This particle size is the same as the d_{50} of the sieved fraction (< 45 μm). The < 45 μm fraction is also fitted with a Rosin Rammler distribution, which is also modelled in CFD. The experimental operating condition chosen for the model development is at 10.3 m/s average air velocity, because sufficient experimental data and deposit photographs are available for this condition. It is recognized that the critical velocity for deposition is likely to be a function of particle size, even at the same $T\text{-}T_g$ level. However, a more detailed experimental study that looks at particle bouncing behaviour at the single particle level is required to understand such a particle-size dependency. Thus, this is accepted as a limitation of the current model and may be an area for future research.

The model is written through the Fluent UDF template for Discrete Phase Model (DPM) boundary conditions. A condensed version of the UDF is presented below for explanation and the full detail of the UDF is shown in Appendix 2.

```
Eloss = 0.5 * particlemass * Vcriticalnormal * Vcriticalnormal;

Einormal = 0.5 * particlemass * normal_velocity * normal_velocity;

Erebound = Einormal - Eloss;

Erebound = MAX (Erebound, 0);

Vreboundnormal = sqrt(2 * Erebound / particlemass);

if (Erebound == 0)

{

f1= fopen("D:\\55 walla.txt","a");

fprintf(f1,"%d %e %e %e %e %e \n",p->part_id,normal_velocity, tangential_velocity,P_POS(p)[0], P_POS(p)[1],

P_POS(p)[2], P_MASS(p));

fclose(f1);

p->stream_index=-1;

return PATH_ABORT;

}
```

```
else
{
for(i=0; i<idim; i++)
p->state.V[i] *= 1; /* 1 is the tan COR, this computes rebound tan_velocity in vector form */
for(i=0; i<idim; i++)
 p->state.V[i]-= Vreboundnormal * normal[i]; /* 1 is the normal COR, this computes rebound normal velocity in vector
form */
for(i=0; i<idim; i++)
p->state0.V[i] = p->state.V[i];
return PATH_ACTIVE;
 }
```

Substitution of Equation 5.5 into Equation 5.2 leads to

$$\frac{1}{2}mV_{normal,r}^{2} = \frac{1}{2}mV_{normal,i}^{2} - \frac{1}{2}mV_{normal,cr}^{2} \qquad (5.6)$$

In the UDF above, a critical normal velocity ($V_{critical\ normal}$ in UDF; $V_{normal,cr}$ in Equation 5.6) is assumed for each CFD run. At the point of particle impact, the energy dissipated due to the critical normal velocity is subtracted from the normal component of the particle impinging kinetic energy. If the right hand side of Equation 5.6 is equal to or less than zero, the particle is considered to be captured by the wall. The UDF then writes its deposition position in the x-y coordinate to a text file and terminates its trajectory calculation. If the right hand side of Equation 5.6 is greater than zero, then a part of the kinetic energy is not dissipated and still available for rebound. This excess kinetic energy is converted back to the normal velocity component of the rebounding particle. In this case, the tangential velocity is assumed to retain its original value. There are limited evidences in the literature suggesting that tangential component of particle kinetic energy is also dissipated to some extent (Xu *et al.*, 1993). Upon

impact, some particles may rotate along the surface before lifting off and a certain portion of the tangential kinetic energy is expanded towards lifting part of the particle surface to sustain its rotational motion. While the energy dissipation mechanisms in the normal direction have been well established (Wall *et al.*, 1990; Konstandopolus, 2006), the coefficient of restitution for the tangential component needs further research and setting this to unity in this thesis is acknowledged as a simplifying assumption.

With the particle gun exit air velocity and the particle size held constant in the CFD model, the only variable of interest is the critical normal velocity. It is not known *a priori* the exact relationship between the critical normal velocity and $T\text{-}T_g$. However, considering the average air velocity in the particle gun was thought to be 4.5 m/s and the maximum centre line velocity was thought to be around 6 m/s, it is expected the maximum particle impinging velocity will not exceed the maximum. The resultant % deposition and deposit morphology for the case of average particle size of 30 μm is shown in Figure 5.16 (a) through to 5.16 (g).

The size of the plot in Figure 5.16 corresponds to the actual size of the collection plate used in the experiment, i.e. 164 mm × 136 mm. The underlying trend shown by these figures is very distinct. As the critical normal velocity for deposition is increased from 0.1 m/s to 1.5 m/s, the % deposition also increases from 9.2% to 56.7% (Figure 5.17). This trend is similar to the experimental observation of increasing % deposition with increasing $T\text{-}T_g$ (Figure 5.18). This supports the modelling approach of using the critical normal velocity for deposition as a substitute for $T\text{-}T_g$.

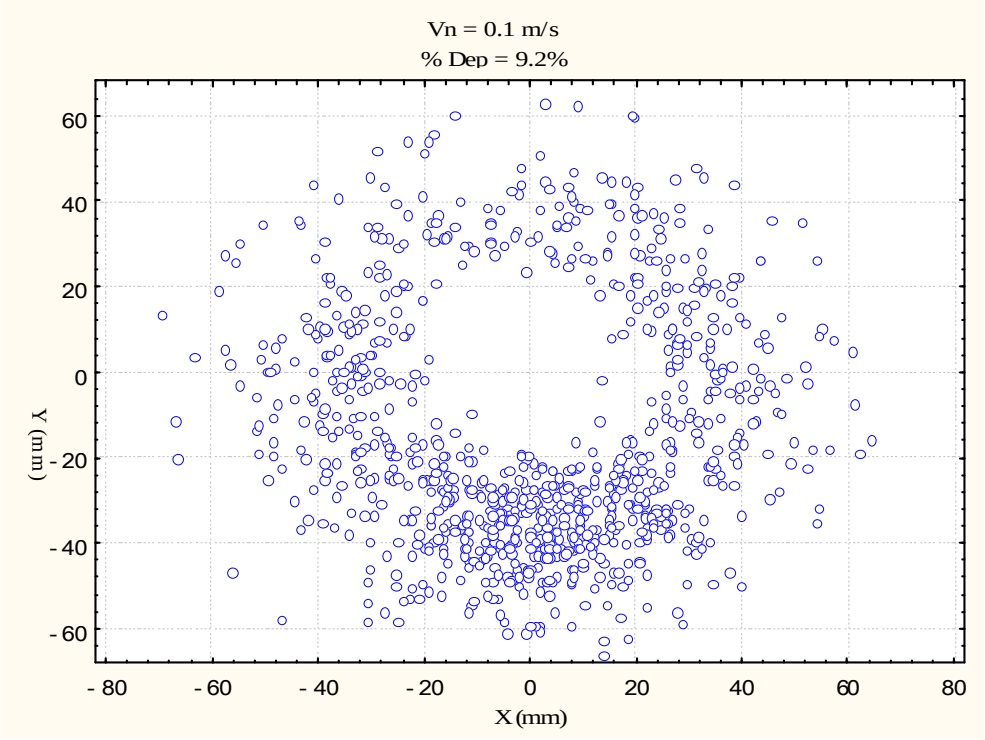

Figure 5.16 (a) % deposition and deposit morphology at critical normal velocity = 0.1 m/s.

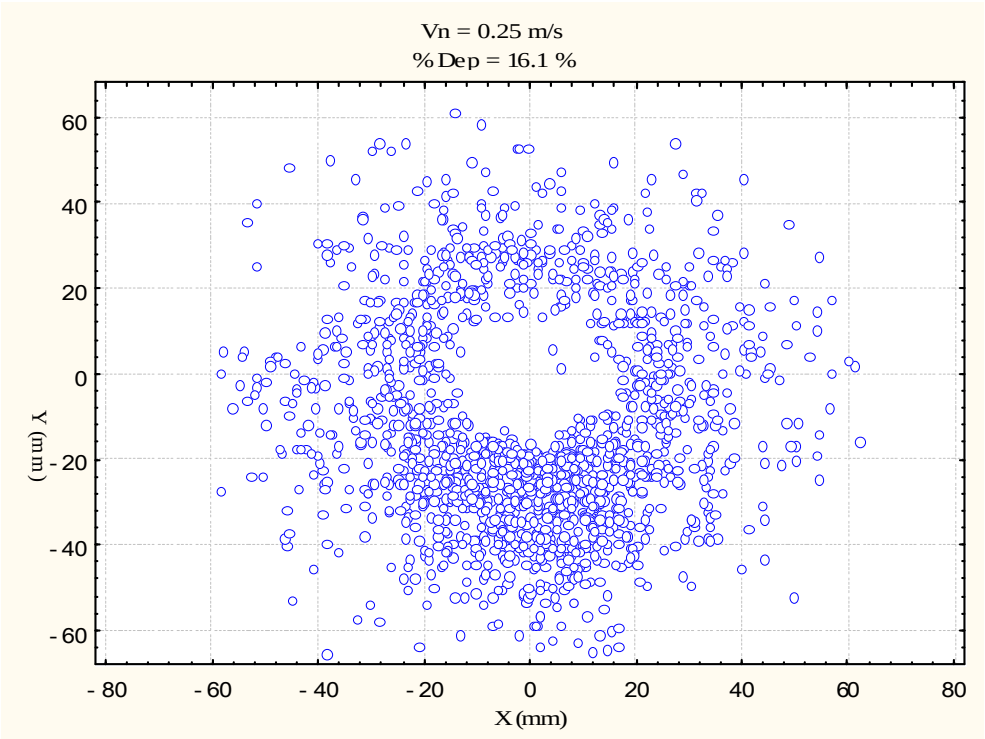

Figure 5.16 (b) % deposition and deposit morphology at critical normal velocity = 0.25 m/s.

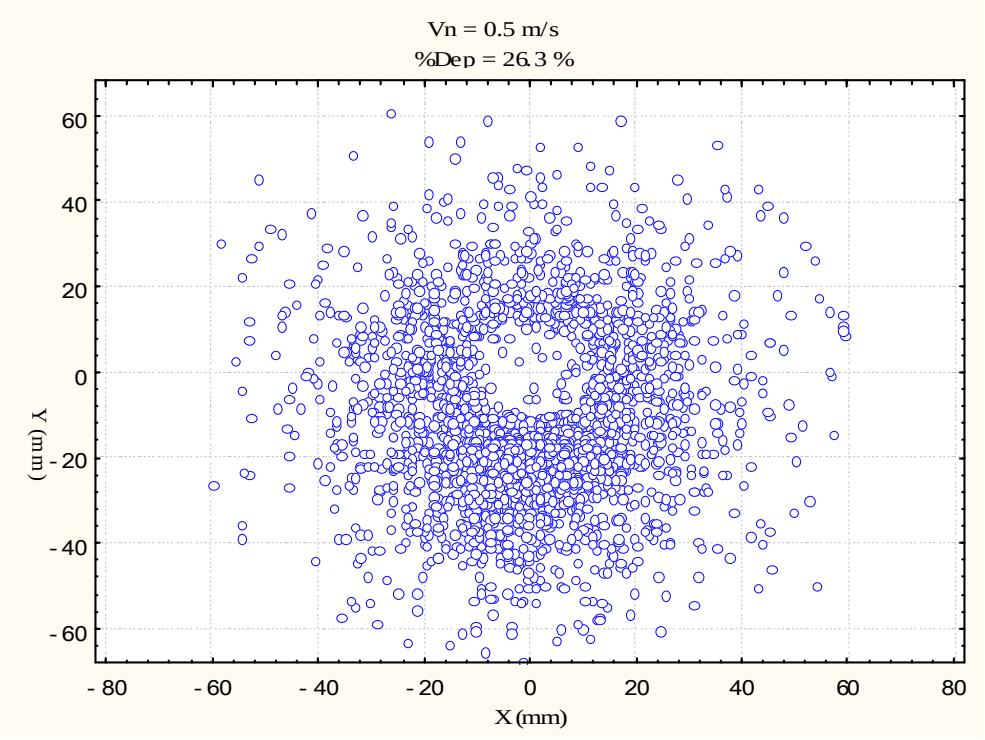

Figure 5.16 (c) % deposition and deposit morphology at critical normal velocity = 0.5 m/s.

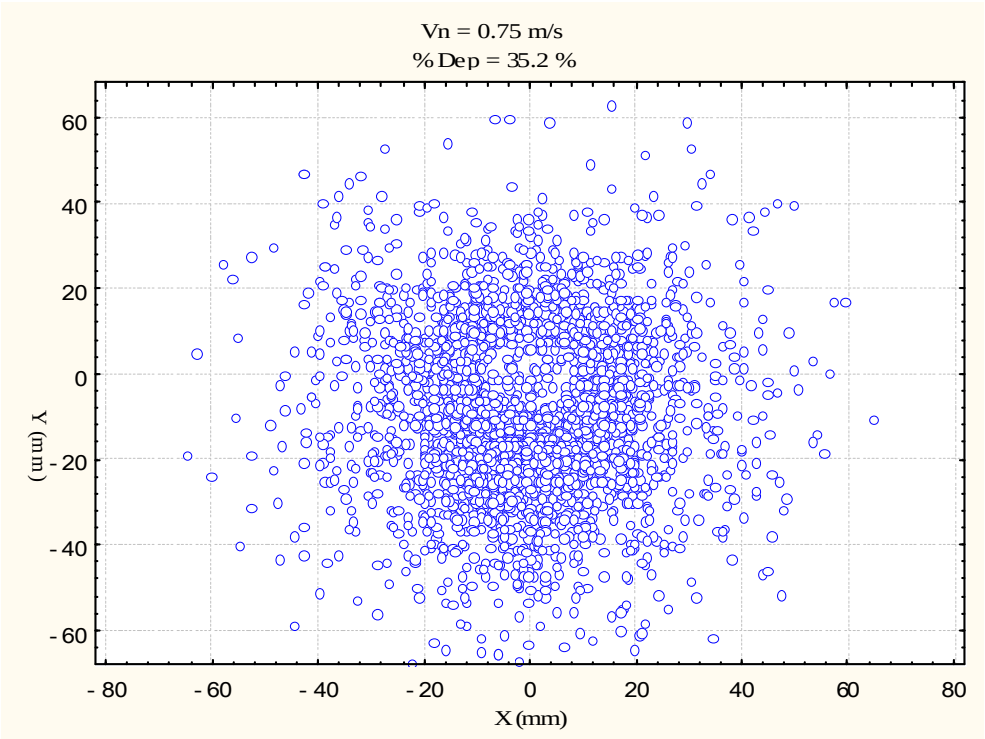

Figure 5.16 (d) % deposition and deposit morphology at critical normal velocity = 0.75 m/s.

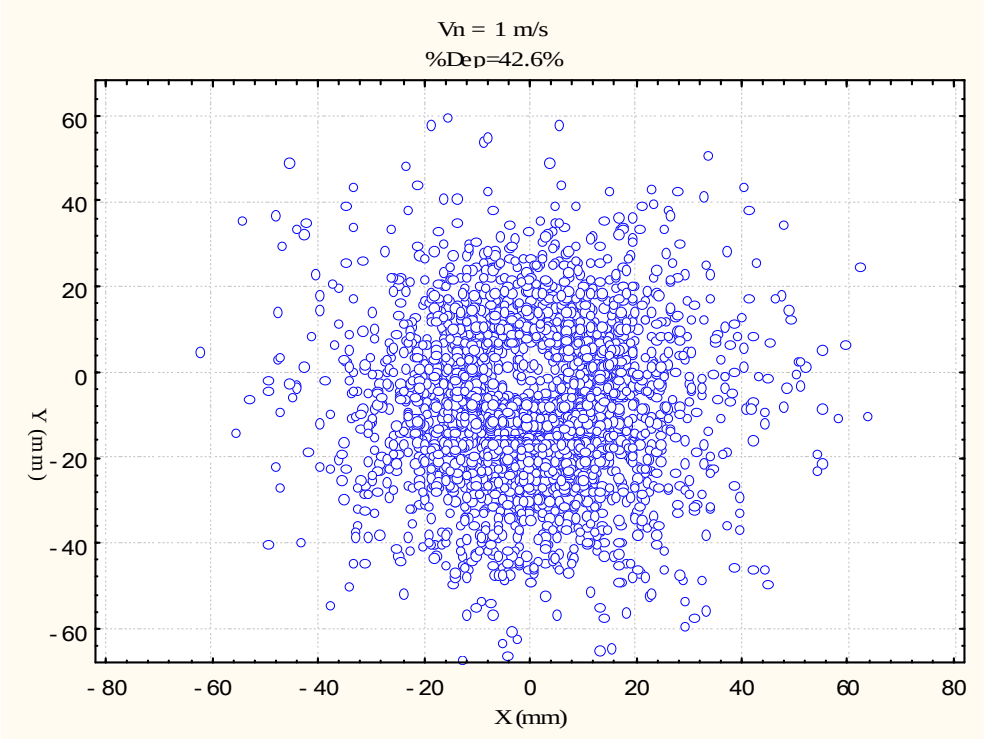

Figure 5.16 (e) % deposition and deposit morphology at critical normal velocity = 1 m/s.

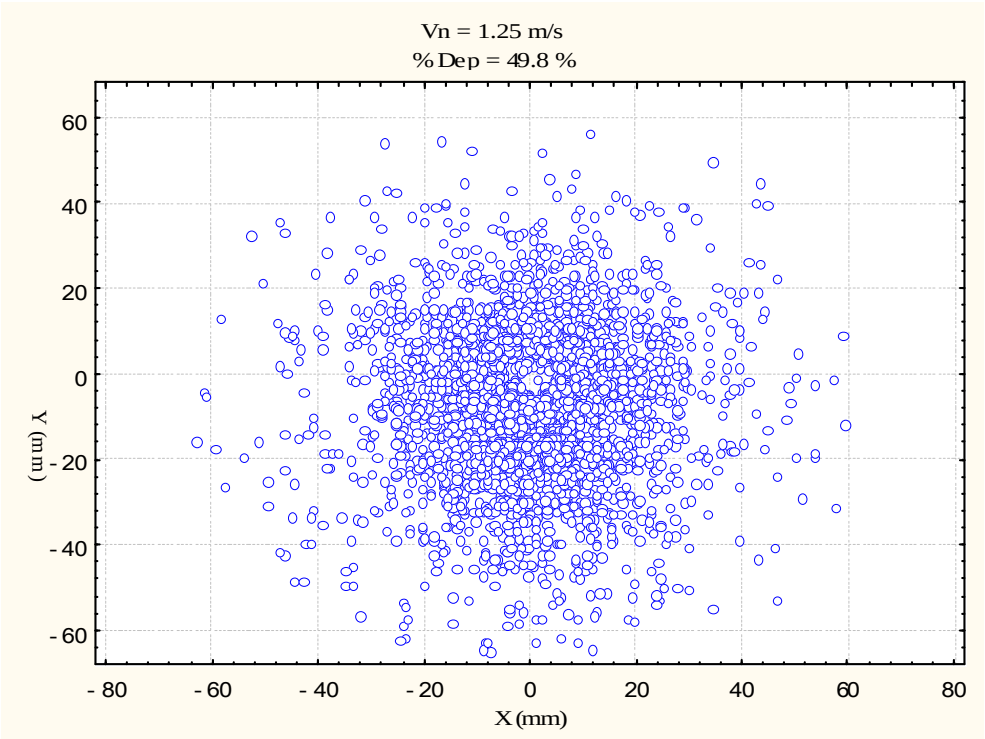

Figure 5.16 (f) % deposition and deposit morphology at critical normal velocity = 1.25 m/s.

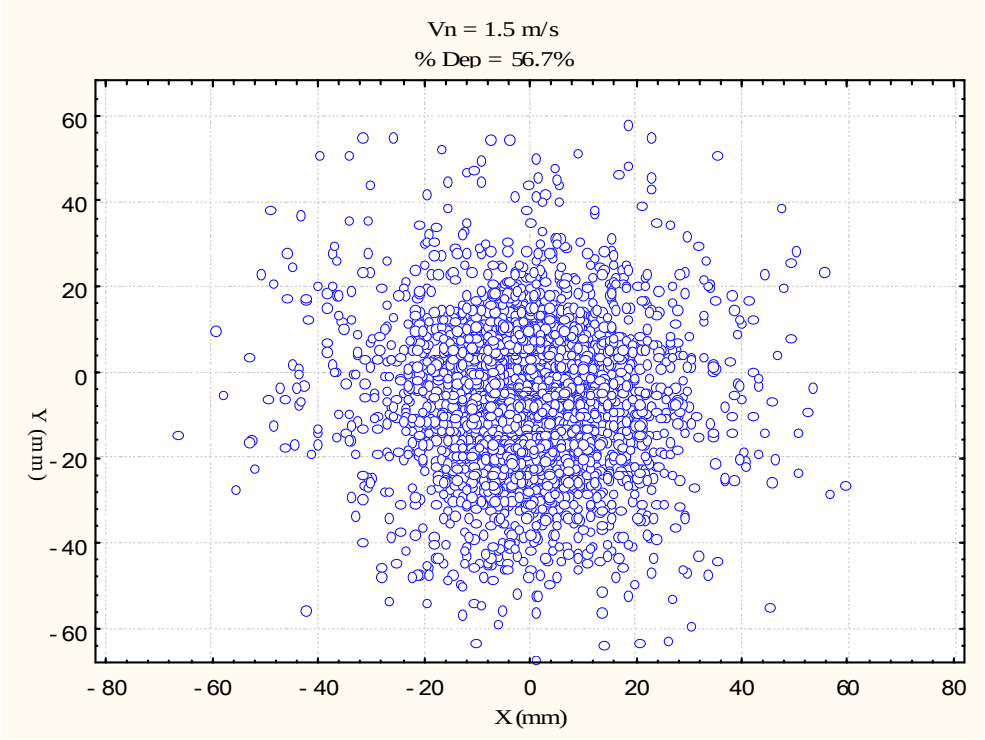

Figure 5.16 (g) % deposition and deposit morphology at critical normal velocity = 1.5 m/s.

Accompanying this increase in % deposition is the evolution of the deposit morphology. At low critical velocity (corresponding to low levels of stickiness), particles tend not to deposit at the central regions on the collection plate. This is because the normal impinging jet and the radial wall jet close to the plate centre have significant momentum, which also leads to relatively large particle impact velocities there. Further away from the centre, both the radial wall jet and particle velocity will level off and the condition becomes favourable for particle deposition. The centre clear ring of no deposition observed in Figure 5.16 gets progressively smaller with increasing critical normal velocity until it finally disappears at between 1.25 and 1.5 m/s. These values (1.25 m/s and 1.5 m/s) are relatively low compared to the average CFD jet velocity of 4.5 m/s. However, Figure 5.4 shows that the velocity along the jet axis rapidly declines to zero as the plate is approached. At a distance of 0.1 D above the plate (1.1 mm) the velocity just above the stagnation zone is in range of 1.6 m/s to 2 m/s, as shown in Figure 5.6. Particles deposited in the central region of

the plate do not necessarily result from first impacts. Thus, the CFD prediction of the deposit clear ring disappearing at in the velocity range of 1.25 m/s to 1.5 m/s seems reasonable.

This evolving deposit morphology is in good visual agreement with experimental observations that have been shown in Figure 3.9 and Appendix 1. For model interpretation, the photographs of the experimentally observed deposit morphology for the condition of 10.3 m/s air velocity and <45 μm particle size have been compared with the CFD simulation at 4.5 m/s. The size of the clear ring from both the CFD simulation and experiments is specifically compared.

To derive the relationship between $T\text{-}T_g$ and CFD critical normal velocity V_n, the respective deposition results are plotted in Figure 5.17 and Figure 5.18. The V_n = 0 m/s (Figure 5.18) corresponds to the onset of deposition at $(T\text{-}T_g)_{critical}$ in Figure 5.17. Both CFD and experimental results are summarized in Table 5.1.

Table 5.1 % Deposition as a function of $T\text{-}T_g$ and critical normal velocity.

Experimental		CFD	
T-Tg DegC	**% Dep**	**Vn m/s**	**% Dep**
14.3	19.0	0.10	9.2
15.0	8.0	0.25	16.1
19.6	12.9	0.50	26.3
21.6	7.7	0.75	35.2
25.7	30.3	1.00	42.6
28.0	30.3	1.25	49.8
31.9	39.4	1.50	56.7
33.2	28.8		
35.9	48.7		
36.4	44.8		
37.1	45.4		
40.7	46.9		
41.1	52.4		
46.0	52.1		

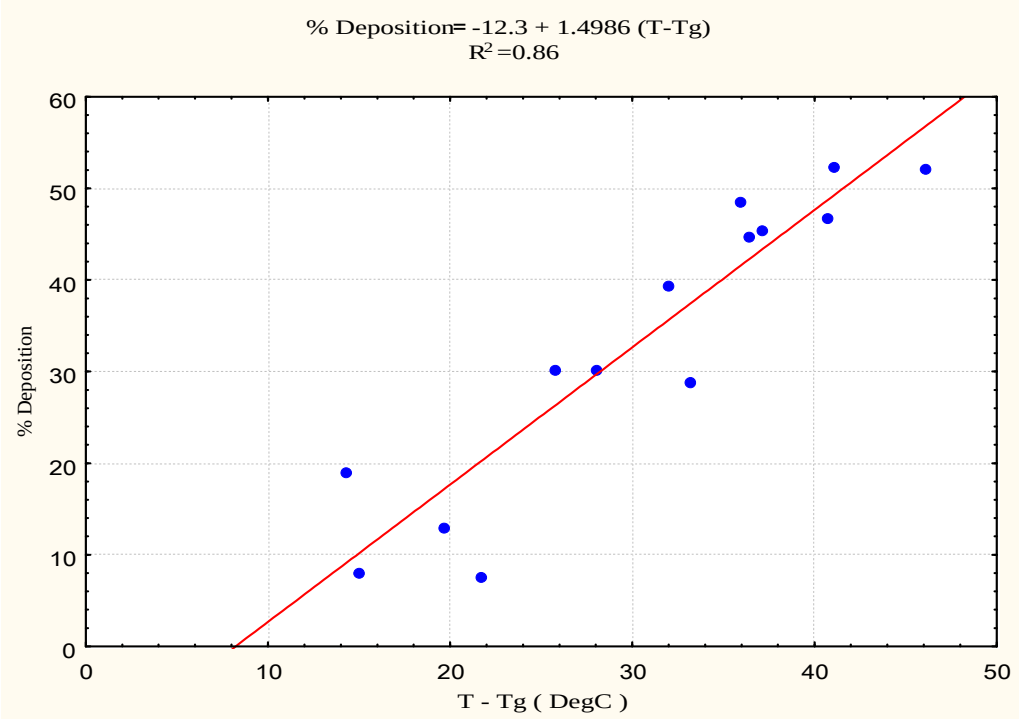

Figure 5.17 Experimental % deposition versus $T-T_g$ for SMP, d(0.5) of 30 µm, jet velocity 10.3 m/s, H/D ratio of 4 and $(T-T_g)_{critical}$ of 8.2 °C.

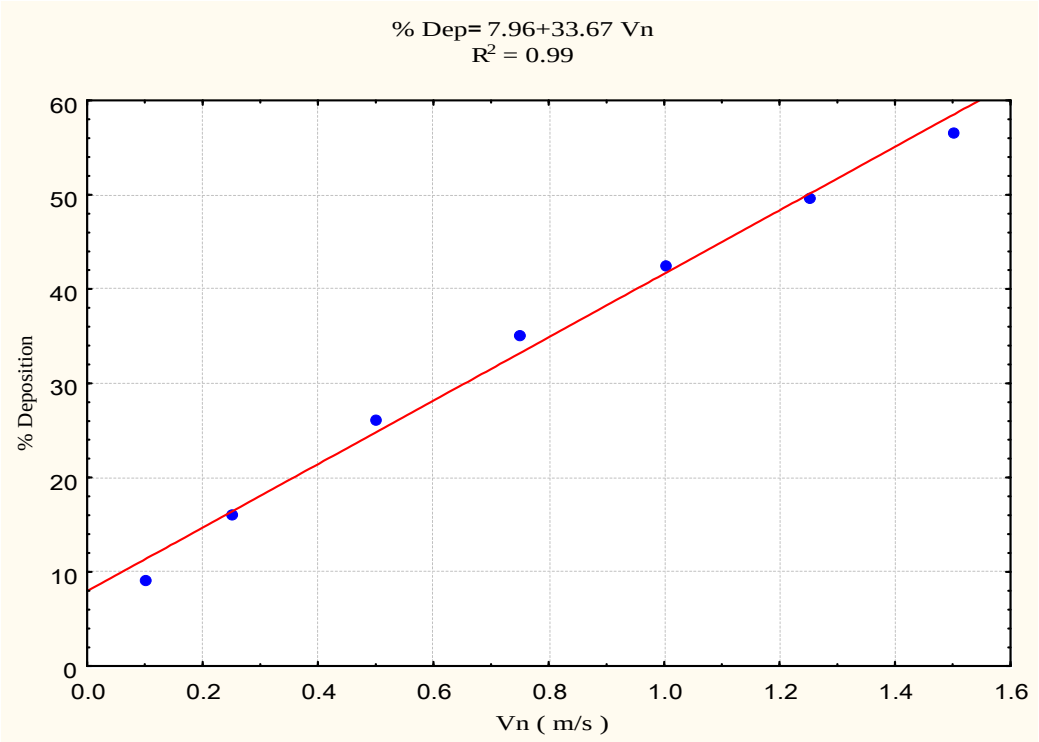

Figure 5.18 CFD % deposition versus V_n for 30 µm particles, jet velocity 4.5 m/s and H/D ratio of 4.

Figure 5.18 shows that the results from CFD simulation are similar to the particle gun experimental results and can also be fitted with a linear regression line as a first order approximation. The resultant fitted first order models for both the experiment and CFD simulation are

$$\% \text{ Deposition} = -12.3 + 1.499\,(T - T_g) \qquad (5.7)$$

and

$$\% \text{ Deposition} = 7.96 + 33.6\,V_n \qquad (5.8)$$

Equations 5.7 and 5.8 can be equated to match the % depositions experimental with the % deposition CFD to derive V_n as a function of $T\text{-}T_g$.

$$V_n = 0.0445\,(T - T_g) - 0.6 \quad [\text{m/s}] \qquad (5.9)$$

Unfortunately Equation 5.9 is unlikely to be valid because of the different CFD and experimental jet velocities used. It is anticipated that a higher CFD jet velocity of 10.3 m/s would require higher particle capture velocities to give CFD deposition % that match experimental deposition %.

A relationship can also be established for the CFD results between V_n and deposit morphology in terms the centre clean ring diameter, as shown in Figure 5.19. The centre clear ring diameter decreases logarithmically with increasing V_n.

$$\text{Clear Ring Diameter} = 10.59 - 37.52\log(V_n) \qquad (5.10)$$

Substituting Equation 5.9 for V_n leads to

$$\text{Clear Ring Diameter} = 10.59 - 37.52\log\left[0.0445\,(T - T_g) - 0.6\right] \qquad (5.11)$$

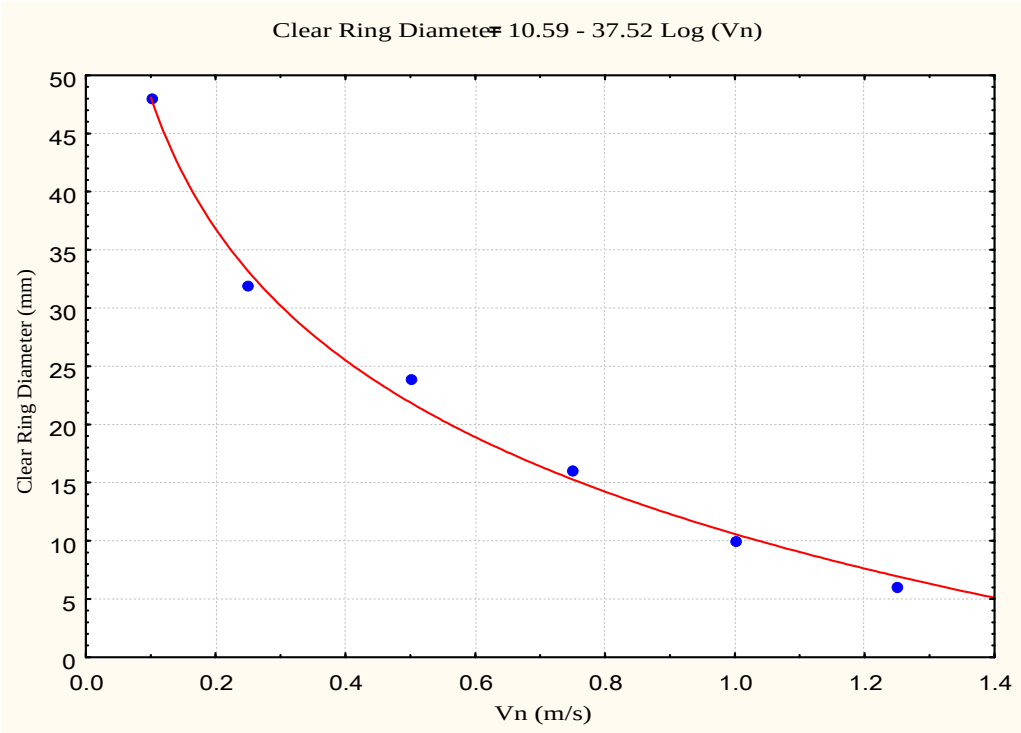

Figure 5.19 Regression plot of CFD simulation results, clear ring diameter against V_n.

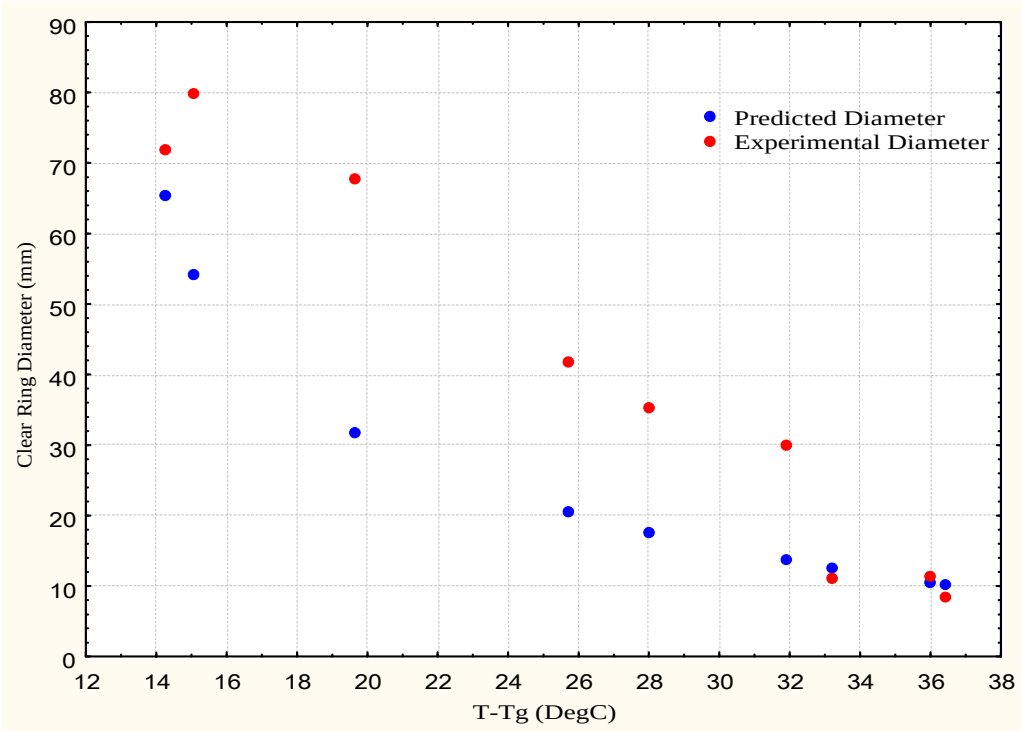

Figure 5.20 Comparison of experimentally observed deposit clear ring diameter with CFD prediction using Equation 5.11.

The predicted clear ring diameter is shown in Figure 5.20 together with the experimentally measured values assuming similar levels of % deposition. It is seen that the diameters predicted by the CFD boundary condition are consistently lower than the experimental values. The difference gets larger then smaller with increasing $T\text{-}T_g$ and has a maximum of 40 mm at $T\text{-}T_g$ of 20 °C. At $T\text{-}T_g$ levels above 33 °C, the difference is negligible. This difference may be due to the lower average velocity used in the CFD models compared to the experimental tests.

In general, the CFD wall boundary condition has overestimated the rate of deposit morphology evolution in the low critical velocity range and predicted correctly the trend of narrowing clear ring diameter with increasing $T\text{-}T_g$. The lack of agreement in the clear rings absolute dimension between the numerical and experimental values is, however, a limitation of the current model.

5.5.4 Angle of Impact and Wall Boundary Condition

In the current model, the energy dissipative mechanisms have been assumed to be operative only in the normal direction of impact. The tangential velocity at point of impact is assumed to play no part in particle deposition and rebound. Part of this assumption is due to the scarcity of existing literature that investigates the effect of impact angle.

Figure 5.21 shows a selected number of particle trajectories from the CFD simulation. For demonstration purpose, the wall boundary condition has been set to “reflect” and the lines are the path lines of the particles. It is seen in Figure 5.21 that the first point of particle impact is located at the centre of the plate. This is due to the inertia of the particles and they only expand slightly within the jet. As a result, particles will collide with the wall with their velocity predominantly in the wall direction. Particles

rebounding off the plate after first impacts are seen to spread out radially due to their entrainment in the radial wall jet. Most of the second impacts take place in an area still within the corresponding area of the pipe. This is due to the rebounding particles being caught up in the jet going in the wall direction. Subsequent particle-surface impacts still occur, with particles bouncing along their trajectories. Due to the change in direction of the particle trajectories, their impact velocities now have a higher tangential velocity to normal velocity ratio than those of the first two impacts.

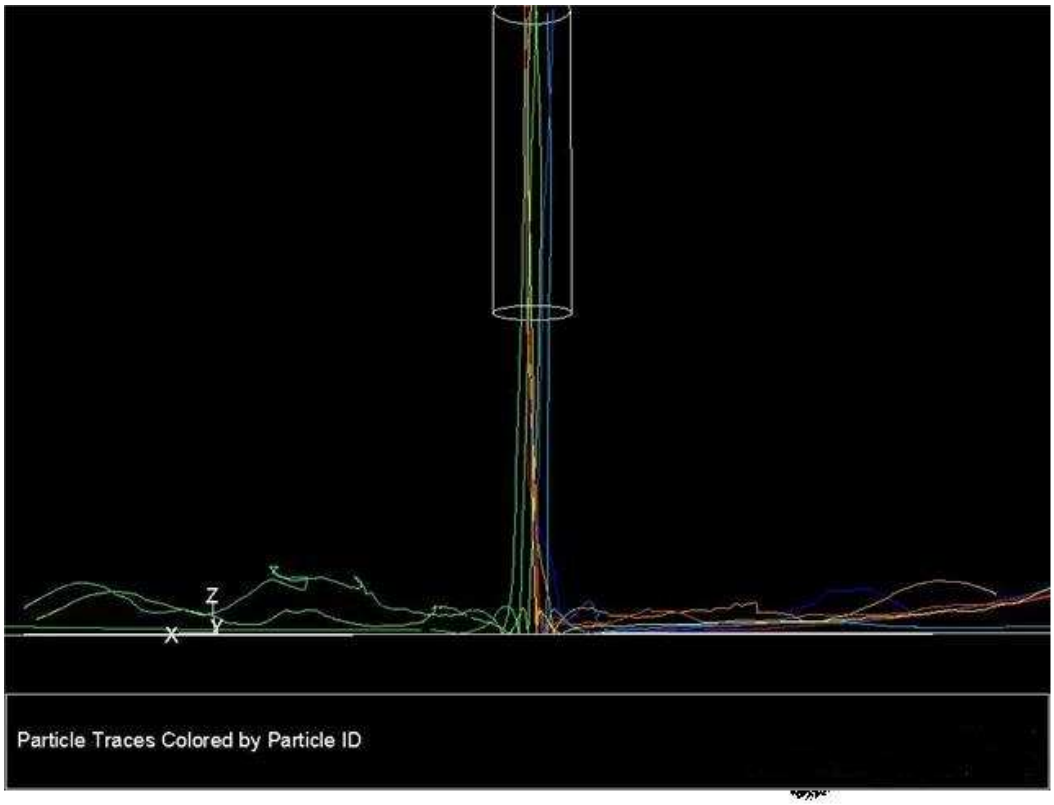

Figure 5.21 Particle trajectories in the impingement zone of the particle gun, CFD simulation, H/D 4, jet velocity 10.3 m/s.

Konstandopoulos (2006) is one of few authors to investigate the criteria for particle deposition/rebound at oblique impact, i.e. the incoming particle has a significant tangential velocity component. The author has proposed that there exists a critical angle of incidence for particle deposition.

$$\alpha_{cr} = \arctan\left(\frac{V_t}{V_n}\right) \tag{5.12}$$

or

$$\left(\frac{V_t}{V_n}\right) < \tan(\alpha_{cr}) \quad \text{for deposition to occur} \tag{5.13}$$

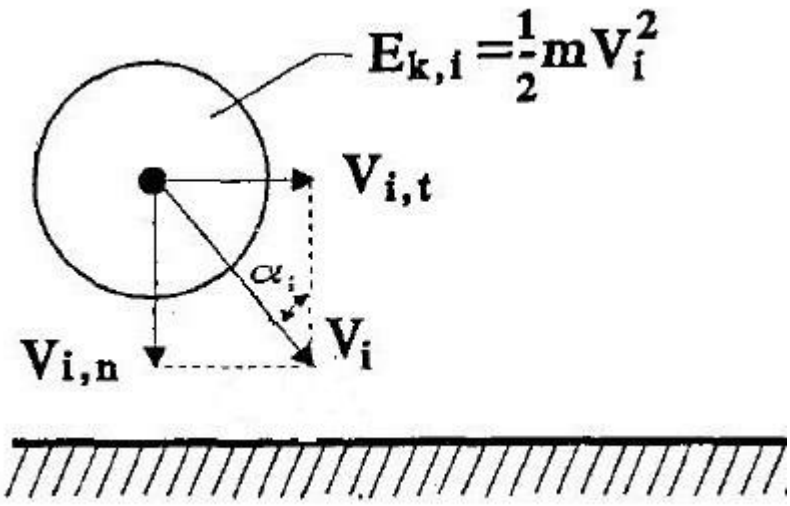

Figure 5.22 Illustration of angle of incidence for an impinging particle, Xu and Willeke (1993).

As shown in Figure 5.22, α_i is the angle of incidence relative to the normal. V_t and V_n are the tangential and normal velocity of the impacting particle, respectively. At normal angle of incidence, α_i equals zero and so is the ratio V_t/V_n. As the angle of impact gets more acute, V_t/V_n also increases proportionally. Motivated by a number of experiments that have studied particle impact on cylindrical surfaces, Konstandopoulos (2006) postulates that beyond a critical angle of incidence (or a critical V_t/V_n ratio), impacting particles cannot stick even though its normal velocity of impact still fulfils the criteria of $V_n < V_{n,\,crit}$. The author fitted his model to the

experimental data of Wang and John (1988), who studied the impaction of monodisperse ammonium fluorescein particles on stainless steel cylinders and arrived at a value of V_t/V_n = 2.752. Similarly, a V_t/V_n = 6.88 has been found to yield good agreement with experiments involving biological particles impacting on glass rods by Aylor and Ferrandino (1985). No experimental data is available for milk powder.

A modification of the original UDF in the CFD simulation has been made to include the V_t/V_n effect. Simulation has been run for the extreme case of case of V_t/V_n = 30, corresponding to a α_{cr} = 88°, for a number of critical normal velocity. Thus if the particle impacts the surface with a V_t/V_n greater than 30 (α_i = 88°) it will rebound and vice versa. The results are shown in Appendix 3 and the inclusion of the extra criteria does slow down the rate of deposit morphology evolution. However, in the absence of experimental data at low velocities and a wide range of impact angles it is not possible to validate the influence of the V_t/V_n term in the CFD simulation. It is recommended that future particle gun research be carried out in this area using a small plate around 20mm diameter in order to control the contact velocity and the contact angle.

5.5.5 Particle Size Effects

An attempt has been made to incorporate the full particle size distribution used in the actual particle gun experiment in the CFD simulation. Fluent has a built-in Rosin-Rammler particle distribution function for this purpose, which is defined by

$$Y_d = e^{-(d_p/\bar{d}_p)^n} \tag{5.14}$$

In Equation 5.14, *d* is the particle size, $\bar{d}$ is the size constant, *n* is the size distribution

parameter and Y_d is the mass fraction of particles of diameter greater than d (Fluent User Guide). For the particle size distribution used for the CFD simulation (< 45 μm), $\bar{d}$ and n are found to be 41 μm and 2.99, respectively. The minimum and maximum diameters of the particle size are 15.6 μm and 88 μm. Figure 5.23 shows the actual particle size distribution and the fitted Rosin-Rammler distribution.

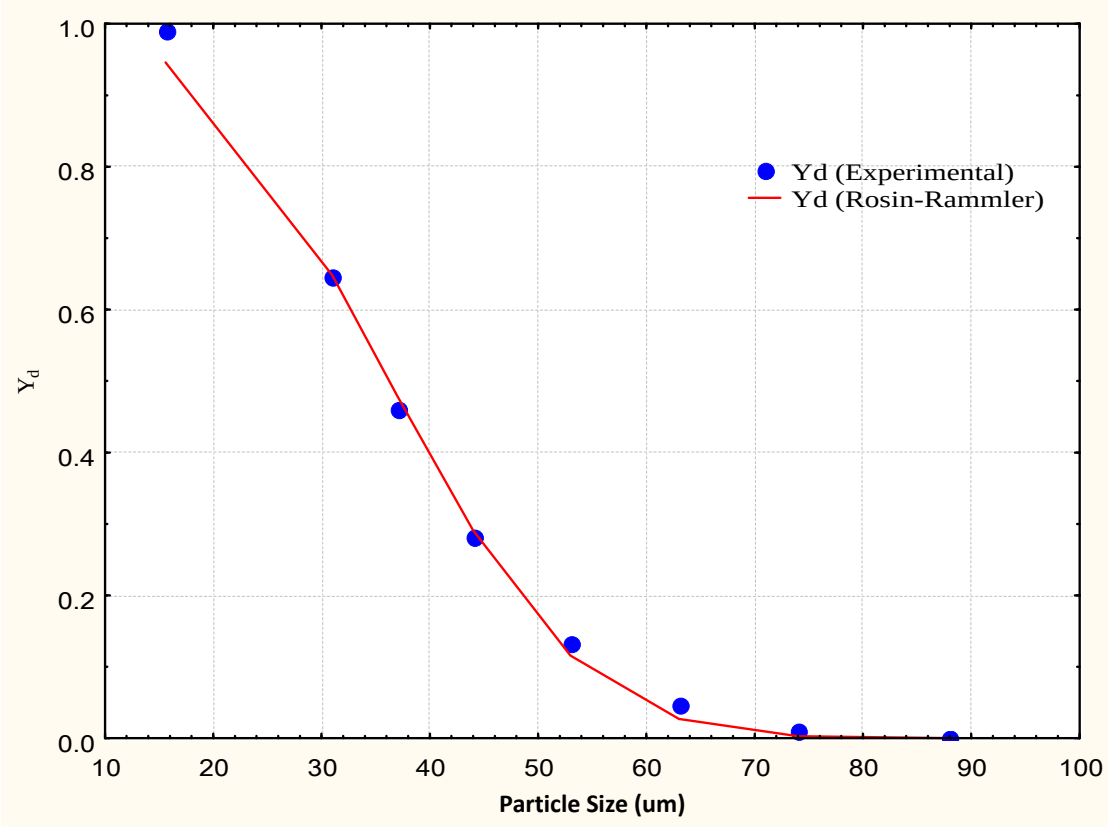

Figure 5.23 Fitted Rosin-Rammler particle size distribution.

It has been found that Fluent does not generate an actual distribution in the particle size as dictated by the Rosin-Rammler function. Rather, the software allocates a mass fraction to each particle representative of the Rosin-Rammler distribution. This results in an equal number of particles in each size fraction. It has been decided to evaluate the contribution to the total % deposition at each level of V_n from particles in the different size fractions. For this purpose, the total number of particles deposited have been divided into ten size fractions, with each fraction having the same number of

original injections, i.e. 1000 each. The data for this is shown in Appendix 4. The contribution to total % deposition for four of the ten size fractions is shown in Figure 5.24 as a function of V_n.

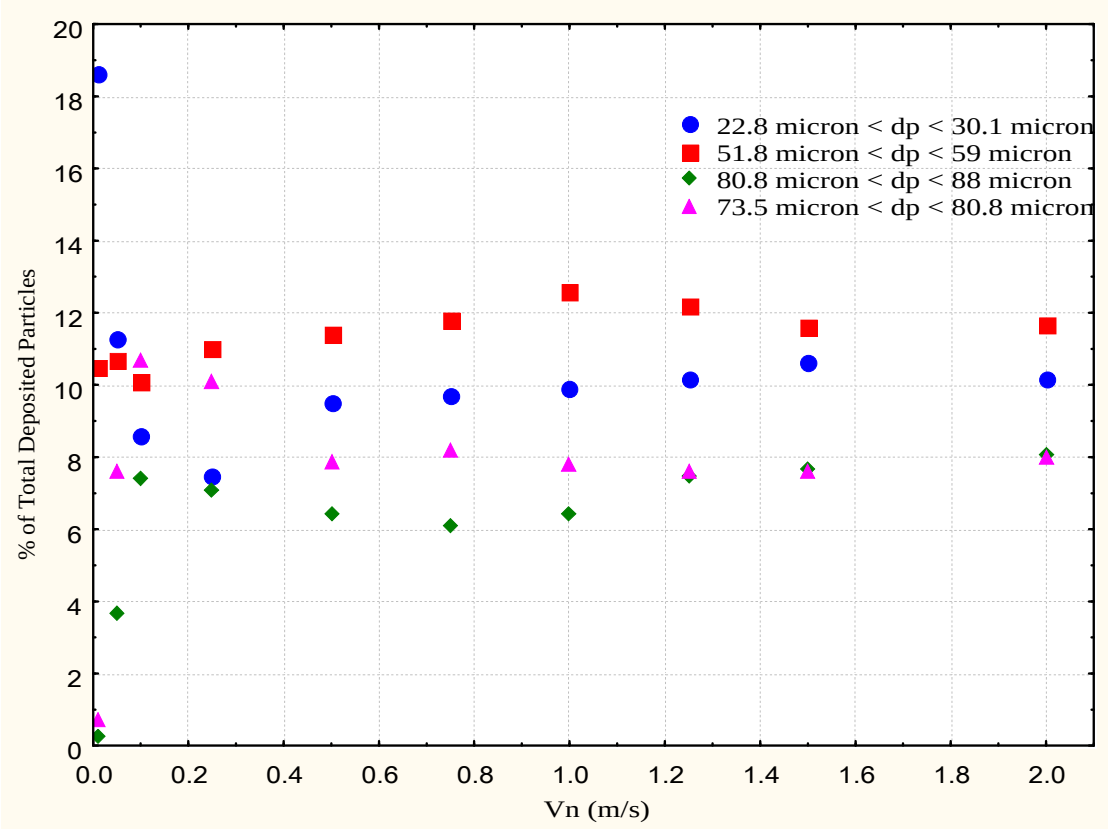

Figure 5.24 Effect of particle size on the % deposition with increasing V_n.

It is seen in Figure 5.24 that the two fractions of heavier particles (particle size >73.5 μm) consistently contribute less to the total % deposition at all levels of V_n. This trend is more pronounced as V_n approaches zero, corresponding to the least sticky state, and the two large fractions are seen to drop towards 0% mass fraction very rapidly. Interestingly, particles in the middle size fraction (51.8 μm < d_p < 59 μm) have a higher deposition propensity than that of the smallest size fraction (22.8 μm < d_p < 30.1 μm) at intermediate levels of V_n. The reason for this is not clear but probably is due to the fact that small particles are more easily entrained in the wall jet flow and carried out of the flow domain. However, this trend is reversed at low levels of V_n, where the contribution from the 22.8 μm < d_p < 30.1 μm is seen to shoot up.

This overall trend is in agreement with the experimental observation that increasing the particle size will lead to a lower % deposition at a given particle stickiness level.

5.6 CONCLUSION

In this chapter, the particle gun has been modelled as an impingement jet setup through CFD. It is found for the H/D ratio of 4 adopted in this study, the jet undergoes minimal development before impinging the surface. Thus the temperature, RH and velocity of the air jet will be very close to the values measured experimentally at the pipe exit. CFD simulation of particle deposition has also been carried out for the finest particle fraction. A wall boundary condition is developed with Fluent's User Define Function for estimating the particle stick/rebound behaviour at impaction surface. The concept of a critical normal deposition velocity is implemented in the UDF and the resultant % deposition and deposit morphology show a similar trend as that observed experimentally. However, the model has overestimated the rate of deposit morphology evolution. More experimental works are needed in this area to study the dependency of deposition behaviour on particle size and tangential velocity, possibly with PIV or other particle imaging systems. Larger scale experiment, such as wind tunnel study of particle deposition, is also recommended.

CHAPTER 6 – CONCLUSIONS AND RECOMMENDATIONS

A review of existing stickiness testing methods for dairy powders has been given. It is agreed by the author that the particle gun test provides the closest simulation to actual spray drying and duct particle conveying process. The particle gun test is based on the adhesion dynamics of particles and is more quantitative than other methods. It allows the experimentation of variables such as particle impact velocity through the air jet velocity, which is difficult or not possible in other methods.

The $(T\text{-}T_g)_{critical}$ criteria as determined from the particle gun test can be an ambiguous measure of the onset of deposition because the critical point is strongly affected by the air jet flow dynamics and the particle size distribution of the milk powder. However, $T\text{-}T_g$ is a good measure of the stickiness of the particle.

Modifications of the particle gun rig have been carried out in this work. The flow orientation is changed from vertical to horizontal to ensure that only particles stuck to the plate are considered as deposited. The distance between the Perspex pipe exit and impingement plate has been shortened to 44 mm or an H/D ratio of 4. Higher H/D ratios result in a more developed and cooler jet, so the $T\text{-}T_g$ level and particle velocity is significantly different from those measured at the pipe exit.

Three velocity values below 20 m/s have been used in the experiments. It is found for bulk skim milk powders, increasing the velocity from 10.3 m/s to 19.4 m/s increased $(T\text{-}T_g)_{critical}$ from 18.6 °C to 39.0 °C. Increasing the particle size from a d(0.5) of 30 μm to 61 μm increases the $(T\text{-}T_g)_{critical}$ from 8.2 °C to 18.6 °C at 10.3 m/s, and from 14.8 °C to 39.0 °C for 19.4 m/s. It is concluded that in addition to the particle surface

stickiness, the kinetic energy of particles also has an important role in determining the outcomes of particle deposition. At higher velocities the particles have more kinetic energy, and for the same level of stickiness and are less likely to stick. Similarly, large diameter particles have more kinetic energy, and are also less likely to stick.

The particle gun test has demonstrated that particle deposition is a two-step process. Firstly, the particles need to arrive at the wall. The subsequent interaction between the particles and the wall, depending on the surface stickiness level and particle kinetic energy, will result in either particle stick or rebound. Interesting deposit morphology has been observed experimentally, alongside the increase in % deposition. At low stickiness levels, particles tend to deposit at the periphery of the collection plate, with a relatively large clear zone at the centre. With increasing $T\text{-}T_g$, the location of particle deposition gets gradually closer to the plate centre and finally the clear zone disappears. This means that the deposits on the collection plate have resulted from multiple collision and rebound events.

It has been shown that the setup of the particle gun rig is similar to an impingement jet, which is characterized by the free jet zone, impingement zone and radial wall jet zone. Computational fluid dynamics (CFD) software Fluent has been employed to model the impingement jet. The SST $k-\omega$ turbulence model together with an appropriate mesh has been shown to model the single phase jet flow correctly. Fluent's Discrete Phase Model together with the eddy dispersion model are used for simulating the trajectories of the particles.

It has been realised that the default wall boundary option offered by Fluent is insufficient for modelling purpose. Experimentally it has been observed that particle deposition is mainly a function of the $T\text{-}T_g$ level and thus CFD modelling should be able to capture this feature. A wall boundary condition has been developed through the User Defined Function of Fluent. The concept of a critical normal deposition velocity has been applied in the code as a numerical substitute for $T\text{-}T_g$. Results show

that increasing the critical normal deposition velocity leads to increased % deposition, which shows similar trends with experimental results. Moreover, the trend of decreasing centre clear zone of no deposition has also been captured well by the model, although the rate of deposit evolution has been overestimated by the model.

It is expected that the critical velocity for deposition will be a function of particle size. However, current experimental resources are insufficient for this finer detail. The Particle Imaging Velocimetry recently acquired by the University of Waikato can possibly be further employed to track individual particles and study their stick/rebound behaviours in more detail. CFD modelling should also be carried out for wind tunnel particle deposition studies, when the experimental results become available for comparison.

The sticky point curve has been commonly employed in milk powder plants and specifies a safe region of spray drying to avoid powder stickiness and deposition. Results from this study show that the sticky point curve is a significant function of both the velocity and particle size distributions, in addition to $T\text{-}T_g$. The standard operating condition of the rig adopted by past researchers is 20 m/s air velocity, although this may be closer to 50 m/s.

It is recommended that plant and pilot scale data be collected and analysed for the velocity and particle size distributions present in different parts of the dryer and exhaust ducts so more concrete conclusions can then be made on the optimal conveying air velocity and duct geometry to be aimed at.

REFERENCES

Adhikari, B., Howes, T., Bhandari, B. R., & Truong, V. (2001). Stickiness in foods – a review of mechanisms and test methods. *International Journal of Food Properies 4*, 1- 33.

Angioletti, M., Nino, E., & Ruocco, G. (2005). CFD turbulent modelling of jet impingement and its validation by particle image velocimetry and mass transfer measurements. *International Journal of Thermal Sciences 44*, 2005.

Aylor, D. E., & Ferrandino, F. J. (1985). Rebound of pollen and spores during deposition on cylinders by inertial impaction. *Atmospheric Environment 19*, 803–806.

Beever, P. F. (1985). Fire and explosion hazards in the spray drying of milk. *Journal of Food Technology 20*, 637 – 645.

Bhandari, B. R., & Howes, T. (1999). Implications of glass transition for the drying and stability of dries foods. *Journal of Food Engineering 40*, 71-79.

Bhandari, B., & Howes, T. (2005). Relating stickiness property of foods undergoing drying and dried products to their surface energetics. *Drying Technology 23*, 781 – 791.

Bitter, J. G. A. (1963) A study of erosion phenomena – Part II. *Wear 6*, 169 -190.

Boonyai, P. (2005). *Development of new instrumental techniques for measurements of stickiness of solid particulate food materials*. PhD Thesis, University of Queensland.

Boonyai, P., Bhandari, B., & Howes, T. (2005). Measurement of glass-rubber transition temperature of skim milk powder by static mechanical test. *Drying Technology 23*, 1499 – 1514.

Bronlund, J. E., & Paterson, A. H. (2004). Moisture sorption isotherms for crystalline, amorphous and predominantly crystalline lactose powders. *International Dairy Journal 14*, 247 – 254.

Brooks, G. F. (2000). *The sticking and crystallization of amorphous lactose*. Master of Technology Thesis, Massey University.

Burwash. W., Finlay, W., & Matida, E. (2006). Deposition of particles by a confined

impinging jet onto a flat surface at Re = 10,000. *Aerosol Science and Technology 40*, 147 – 156.

Busnaia, A. A. (1995). Particle – substrate collisions, particle rebound and removal. *Journal of Adhesion 51*, 167 – 180.

Chatterjee, R. (2004). *Characterising stickiness of dairy powders*. Master of Technology Thesis, Massey University.

Chen, X. D., Lake, R., & Jebson, S. (1993). Study of skim milk powder deposition on a large industrial dryer. *Trans. I. Chem. E. 71 (C)*, 180–186.

Chen, X. D. (1994). Towards a comprehensive model based on control of milk drying process. *Drying Technology 12*, 1105 – 1130.

Chen, X. D. (1997). A new water sorption equilibrium isotherm model. *Food Research International 30*, 755 – 759.

Chen, X. D. (1998). A temperature dependence function of equilibrium sorption isotherm established by a reaction engineering approach. *Journal of Food Engineering 37*, 259 – 269.

Chong, L. V., Chen. X. D., & Mackereth, A. R. (1999). Effect of ageing and composition on the ignition tendency of dairy powders. *Journal of Food Engineering 39*, 269-276.

Craft, T. J., Gragan, J. W., & Launder, B. E. (1993). Impinging jet studies for turbulence model assessment – II An examination of the performance of four turbulence models. *International Journal of Heat and Mass Transfer 36*, 2685 – 2697.

Crofskey, C. M. (2000). *Investigation into the caking problems associated with spray dried cream powders 55 and 77*. Summer Project Report, Massey University.

Davies, C. N. (1965). Deposition of aerosols from turbulent flow through pipes. *Proceedings of the Royal Society of London Series A 289*, 235 – 246.

Dehbi, A. (2008). A CFD model for particle dispersion in turbulent boundary layer flows. *Nuclear Engineering and Design 238*, 707 – 715.

Downton, G. E., Flores-Luna, J. L., & King, C. J. (1982). Mechanisms of stickiness in hygroscopic, amorphous powders. *Industrial and Engineering Chemistry Fundamentals 21*, 447 - 451.

ERCOFTAC database - http://www.cfd.mace.manchester.ac.uk/ercoftac/

Fan, F. G., & Ahmadi, G. (1993). Sublayer model for turbulent deposition of particles in vertical ducts with smooth and rough surfaces. *Journal of Aerosol Science 24*, 45 – 64.

Fennema, O. R. (1996). *Food Chemistry*. New York, USA: Marcel Dekker.

Fletcher, D. F., Guo, B., Harvie, D. J. E., Langrish, T. A. G., Nijdam, J. J., & Williams, J. (2006). What is important in the simulation of spray dryer performance and how do current CFD models perform? *Applied Mathematical Modelling 30*, 1281 – 1292.

Fluent User's Guide (2005). Lebanon, NH: Fluent Inc.

Foster, K. D. (2002). *The prediction on sticking in dairy powders*. PhD Thesis, Massey University.

Friedlander, S. K., & Johnstone, H. F. (1957). Deposition of suspended particles from turbulent gas streams. *Industrial and Engineering Chemistry 49*, 1151 – 1156.

GEA Niro Method No. A 8 a - http://www.niro.com/niro/cmsdoc.nsf/webdoc/ndkw74jjlp

Guha, A. (2008). Transport and deposition of particles in turbulent and laminar flow. *Annual Review of Fluid Mechanics 40*, 311 – 341.

Harvie, D. J. E., Langrish, T. A. G., & Fletcher, D. F. (2002). A computational fluid dynamics study of a tall-form spray dryer. *Food and Bioproduct Processing 80*, 163 – 175.

Hennigs, C., Kockel, T. K., & Langrish, T. A. G. (2001). New measurements of the sticky behaviour of skim milk powder. *Drying Technology 19*, 471 – 484.

Huang, L., Kumar, K., & Mujumdar, A. S. (2003). Use of computational fluid dynamics to evaluate alternative spray dryer chamber configurations. *Drying Technology 21*, 385 – 412.

Intipunya, P., Shrestha, A., Howes, T., & Bhandari, B. (2009). A modified cyclone stickiness test for characterizing food powders. *Journal of Food Engineering 94*, 300 – 306.

Jambunathan, K., Lai, E., Moss, M. A., & Button, B. L. (1992). A review of heat transfer data for single circular jet impingement. *International Journal of Heat and Fluid Flow 13*, 1992.

Kentish, S., Davidson, M., Hassana, H., & Bloore, C. (2005). Milk skin formation during drying. *Chemical Engineering Science 60*, 635 – 646.

Kim, E. H. J., Chen, X. D., & Pearce, D. (2005). Effect of surface composition on the flowability of industrial spray dried dairy powders. *Colloids and Surfaces B: Biointerfaces 46*, 182 – 187.

Konstandoupoulos, A. G. (1991). *Effects of particle inertia on aerosol transport and deposit growth dynamics*. PhD Thesis, Yale University.

Konstandopolous, A. G. (2006). Particle sticking/rebound criteria at oblique impact. *Journal of Aerosol Science 37*, 292 – 305.

Kota, K., & Langrish, T. A. G. (2007). Prediction of deposition patterns in pilot-scale spray dryer using Computational Fluid Dynamics (CFD) simulations. *Chemical Product and Process Modelling 2*, article 26.

Lazar, M. E., Brown, A. H., Smith, G. S., Wong, F. F., & Lindquist, F. E. (1956). Experimental production of tomato powder by spray drying. *Food Technology 10*, 129 – 137.

Li, A., & Ahmadi, G. (1995). Computer simulation of particle deposition in the upper tracheobronchial tree. *Aerosol Science and Technology 23*, 201-233.

Lin, C. S., Moulton, R. W., & Putnam, C. L. (1953). Mass transfer between solid wall and fluid streams – mechanisms and eddy distribution relationships in turbulent flow. *Industrial and Engineering Chemistry 45*, 636.

Lin, J.S., Tsai, C. J., & Chang, C. P. (2004). Suppression of particle deposition in tube flow by thermophoresis. *Aerosol Science 35*, 1235 – 1250.

Liu, B. Y. H., & Agarwal, J. K. (1974). Experimental observation of aerosol deposition in turbulent flow. *Aerosol Science 5*, 145 – 155.

Marchioli, C., & Soldati, A. (2002). Mechanisms for particle transport and segregation in a turbulent boundary layer. *Journal of Fluid Mechanics 468*, 283-315.

Masters, K. (1991). *Spray Drying Handbook*. Singapore: Longman Scientific and Technical.

McFarland, A. R., Gong, H., Muyshondt, A., Wente, W. B., & N. K. Anand. (1997).

Aerosol deposition in bends with turbulent flow. *Environmental Science and Technology 31*, 3371 – 3377.

Murti, R. A. (2006). *The effect of lactose source on the stickiness of dairy powders*. Master of Engineering Thesis, Massey University.

O'Donnell, A. M., Brooks, G. F., Paterson, A. H. J. (2002). A constant humidity air supply system for pilot scale applications. *International Journal of Food Science and Technology 37*, 369 – 374.

Ounis, H., Ahmadi, G., & McLaughlin, J. B. (1993). Brownian particle deposition in a directly simulated turbulent channel flow. *Physics of Fluids A 5*, 1427 – 1432.

Owen, P. R. (1969). Pneumatic transport. *Journal of Fluid Mechanics 39*, 407 – 432.

Ozmen, L., & Langrish, T. A. G. (2003). A study of the limitations to spray dryer outlet performance. *Drying Technology 21*, 895 – 917.

Palzer, S. (2005). The effect of glass transition on the desired and undesired agglomeration if amorphous food powders. *Chemical Engineering Science 60*, 3959 – 3968.

Patel, K. (2009). *Production of uniform particles via single stream drying and new applications of the reaction engineering approach*. PhD Thesis, Monash University.

Papadakis, S. E., & Bahu, R. E. (1992). The sticky issues of drying. *Drying Technology 10* (4), 817 – 837.

Paterson, A. H., Brooks, G. F., Bronlund, J. E., & Foster, K. D. (2005). Development of stickiness in amorphous lactose at constant T-T_g levels. *International Dairy Journal 15*, 513 – 519.

Paterson, A. H., Bronlund, J. E. Zuo, J. Y., & Chatterjee, R. (2007). Analysis of particle-gun-derived dairy powders stickiness curves. *International Dairy Journal 17*, 860 – 865.

Pearce, D. L. (2010). *Private communication.* Fonterra Research Centre, Palmerston North, NZ.

Perry. R. H., & Green, D. W. (1997). *Perry's Chemical Engineer's Handbook*. USA: McGraw-Hill.

Písecký, J. (1997). Handbook of milk powder manufacture. Niro A/S.

Rogers, L, N., & Reed, J. (1984). The adhesion of particles undergoing an elastic-plastic impact with a surface. *Journal of Physics D 17*, 677 – 689.

Stevenson, M. J. H. R. (1999) *Computational modelling of drying milk droplets.* Master of Engineering Thesis, University of Auckland.

Tian, L., & Ahmadi, G. (2007). Particle deposition in turbulent duct flow – comparisons of different model predictions. *Journal of Aerosol Science 38*, 377 – 397.

van Beek, M. C., Rindt, C. C. M. Wijers, J. G., & van Steenhoven, A. A. (2006). Rebound characteristics for 50 μm particles impacting a powdery deposit. *Powder Technology 165*, 53 – 64.

Versteeg, H., & Malalasekra, W (2007). *An Introduction to Computational Fluid Dynamics- The Finite Volume Method* (2 ed.). England: Pearson Education Ltd.

Viskanta, R. (1993). Heat transfer to impinging Isothermal Gas and Flame jets. *Experimental Thermal and Fluid Sciences 6*, 111 - 134.

Wall, S., & John, W., & Wang, H. C. (1990). Measurements of kinetic energy loss for particles impacting surfaces. *Aerosol Science and Technology 12*, 926 – 946.

Wallack, D. A., & King, C. J. (1988). Sticking and agglomeration of hygroscopic, amorphous carbohydrates and food powders. *Biotechnology Progress 4*, 31 – 35.

Wilcox, D.C. (2006). *Turbulence Modelling for CFD, 3rd Edition*, DCW Industries, Inc.

Woo, M. W., Daud, W. R. W., Tasirin, S. M., Zainal, M., & Talib, M. (2008). Effect of wall surface properties at different drying kinetics on the deposition problem in spray drying. *Drying Technology 26*, 15 – 26.

Woo, M. W., Daud, W. R. W., Mujumdar, A. S., Wu, Z. H., Talib, M. Z.M., & Tasirin, S. M. (2008) CFD Evaluation of Droplet Drying Models in a Spray Dryer Fitted with a Rotary Atomizer. *Drying Technology 26*, 1180 – 1198.

Xu, M. D., Willeke, K., Biswas, P., & Pratsinis, S. E. (1993). Impaction and rebound of particles at acute incident angles. *Aerosol Science and Technology 18*, 143 – 155.

Xu, M. D., & Willeke, K. (1993). Right-angle impaction and rebound of particles.

Journal of Aerosol Science 24, 19 – 30.

Young, J., & Leeming, A. (1997). A theory of particle deposition in turbulent pipe flow. *Journal of Fluid Mechanics 340*, 129 – 159.

Zheng, F. (2002). Thermophoresis of spherical and non-spherical particles: a review of theories and experiments. *Advances in Colloid and Interface Science* *97*, 253 – 276.

Zuo, J. Y. (2004). *The stickiness curves of dairy powders*. Master of Technology Thesis, Massey University.

Zuo, J. Y., Paterson, A. H., Bronlund, J. E., & Chatterjee, R. (2007). Using a particle-gun to measure initiation of stickiness of dairy powders. *International Dairy Journal 17*, 268 – 273.

APPENDIX 1 - PHOTOGRAPHS OF DEPOSIT MORPHOLOGY

A1.1 Air Velocity of 10.3 m/s and d_p<45µm Particle fraction

Figure A1.1 Deposit morphology at air velocity of 10.3 m/s and <45 µm particle fraction. T-T_g = 15 °C; % Dep = 8.0 %; Centre Clear Ring Diameter = 80mm.

Figure A1.2 Deposit morphology at air velocity of 10.3 m/s and <45 µm particle fraction. T-T_g = 14.3 °C; % Dep = 19.0 %; Centre Clear Ring Diameter = 72 mm.

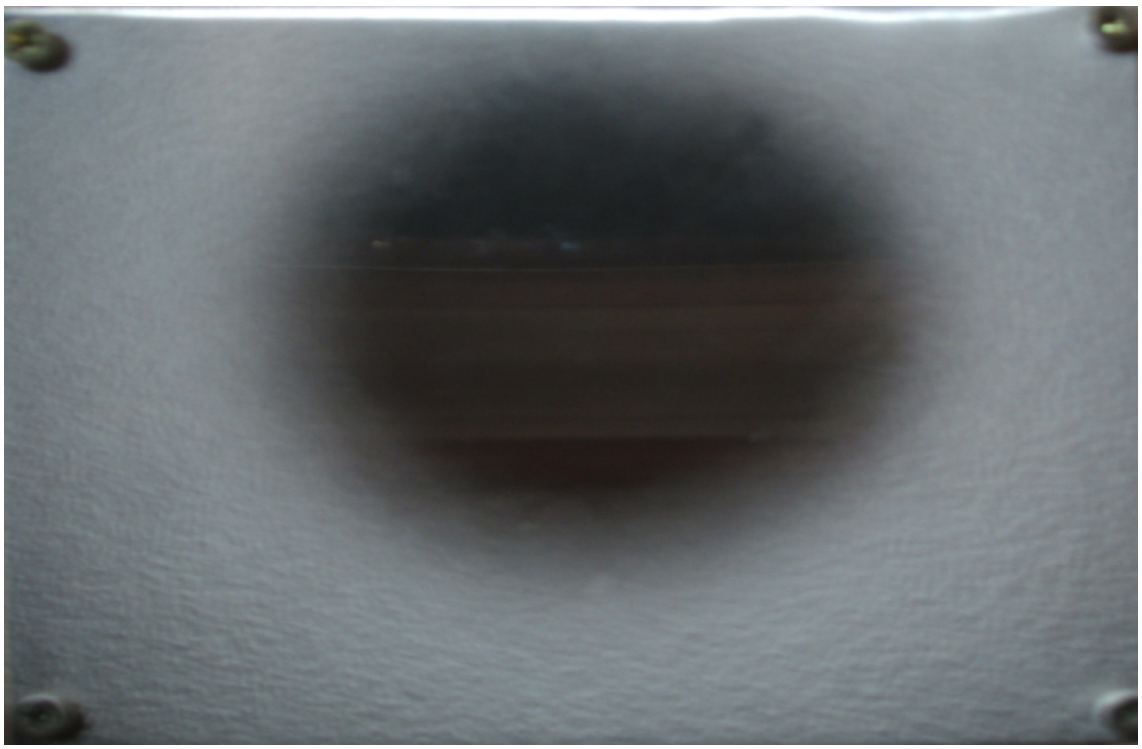

Figure A1.3 Deposit morphology at air velocity of 10.3 m/s and <45 µm particle fraction. T-T_g = 19.6 °C; % Dep = 12.9 %; Centre Clear Ring Diameter = 68 mm.

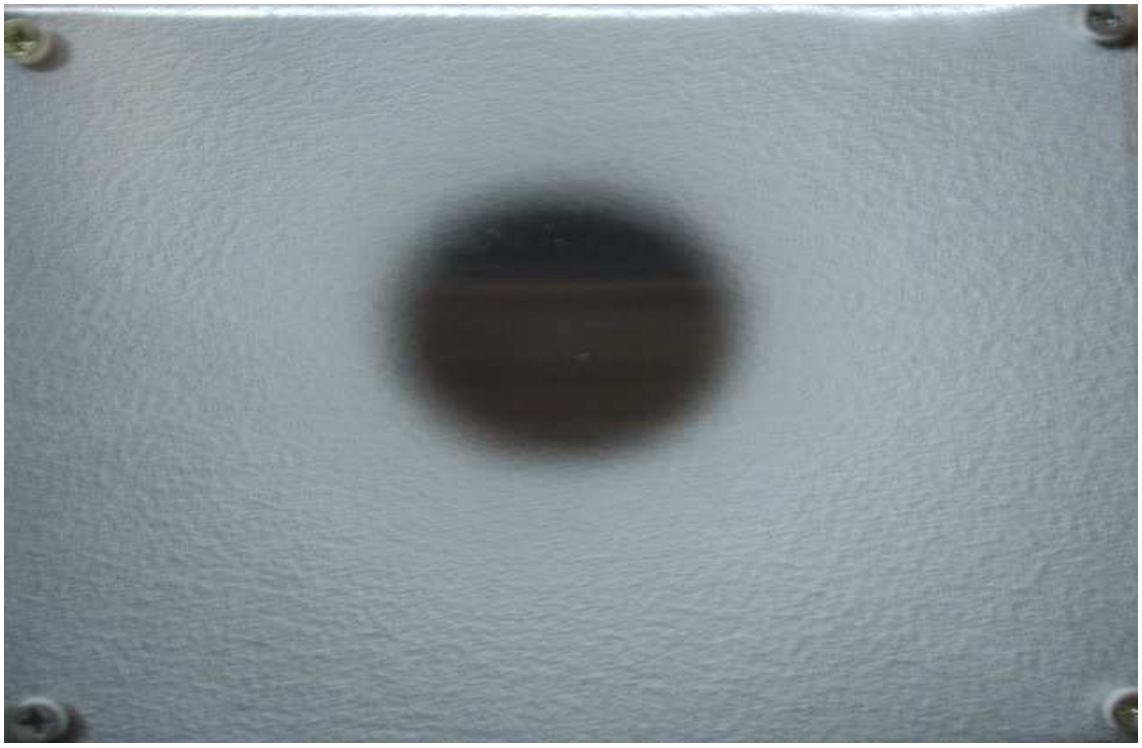

Figure A1.4 Deposit morphology at air velocity of 10.3 m/s and <45 µm particle fraction. T-T_g = 25.7 °C; % Dep = 30.3 %; Centre Clear Ring Diameter = 42 mm.

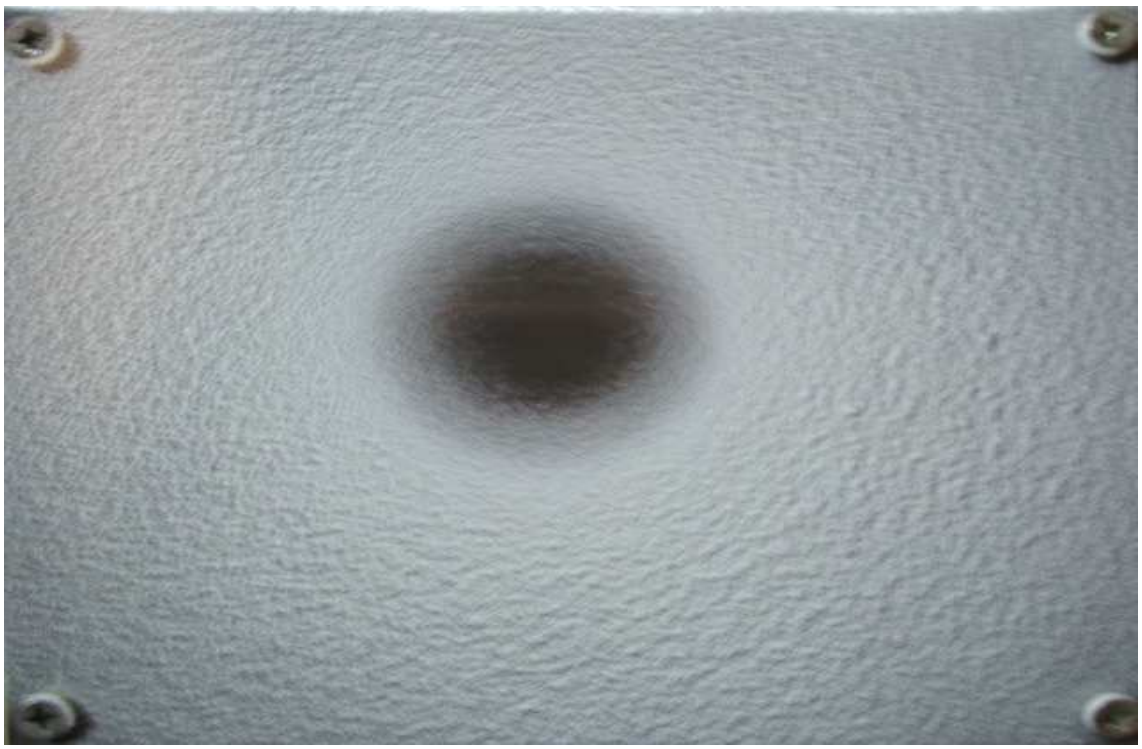

Figure A1.5 Deposit morphology at air velocity of 10.3 m/s and <45 µm particle fraction. T-T_g = 31.9 °C; % Dep = 39.4 %; Centre Clear Ring Diameter = 30 mm.

Figure A1.6 Deposit morphology at air velocity of 10.3 m/s and <45 µm particle fraction. T-T_g = 35.9 °C; % Dep = 48.7 %; Centre Clear Ring Diameter = 11.5 mm.

Figure A1.7 Deposit morphology at air velocity of 10.3 m/s and <45 µm particle fraction. T-T_g = 36.4 °C; % Dep = 44.8 %; Centre Clear Ring Diameter = 19.4 mm.

A1.2 Air Velocity of 10.3 m/s, 45µm<d_p<63µm Particle Size

Figure A1.8 Deposit morphology at air velocity of 10.3 m/s and 45µm<d_p<63µm particle fraction. T-T_g = 17.0 °C; % Dep = 6.39 %.

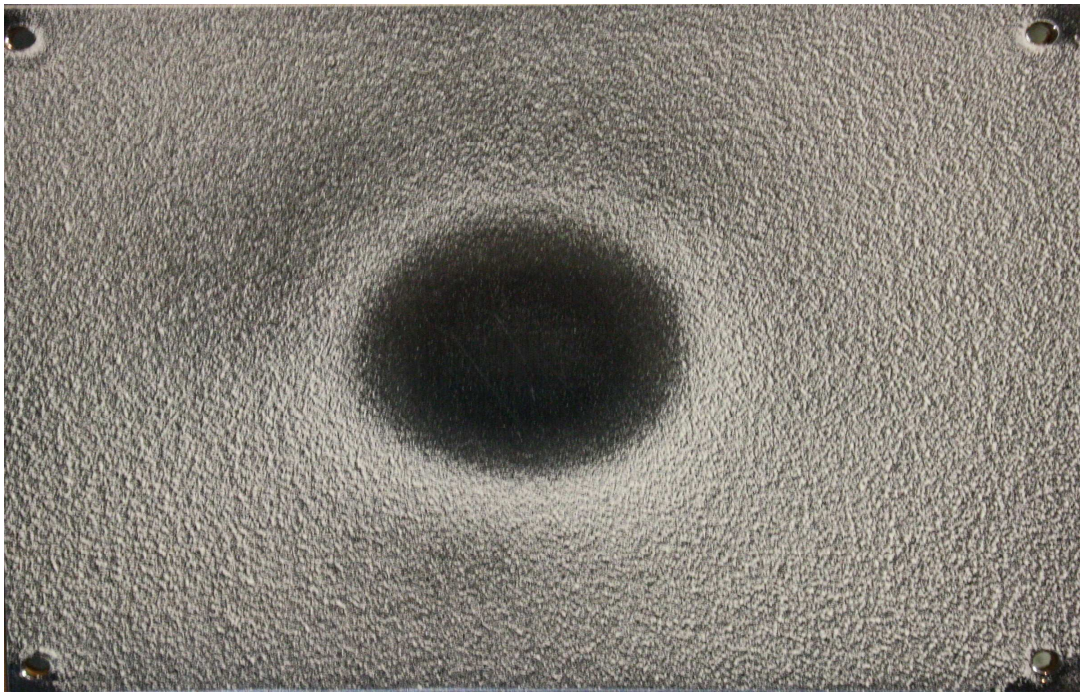

Figure A1.9 Deposit morphology at air velocity of 10.3 m/s and 45µm<d_p<63µm particle fraction. T-T_g = 25.1 °C; % Dep = 14.27 %.

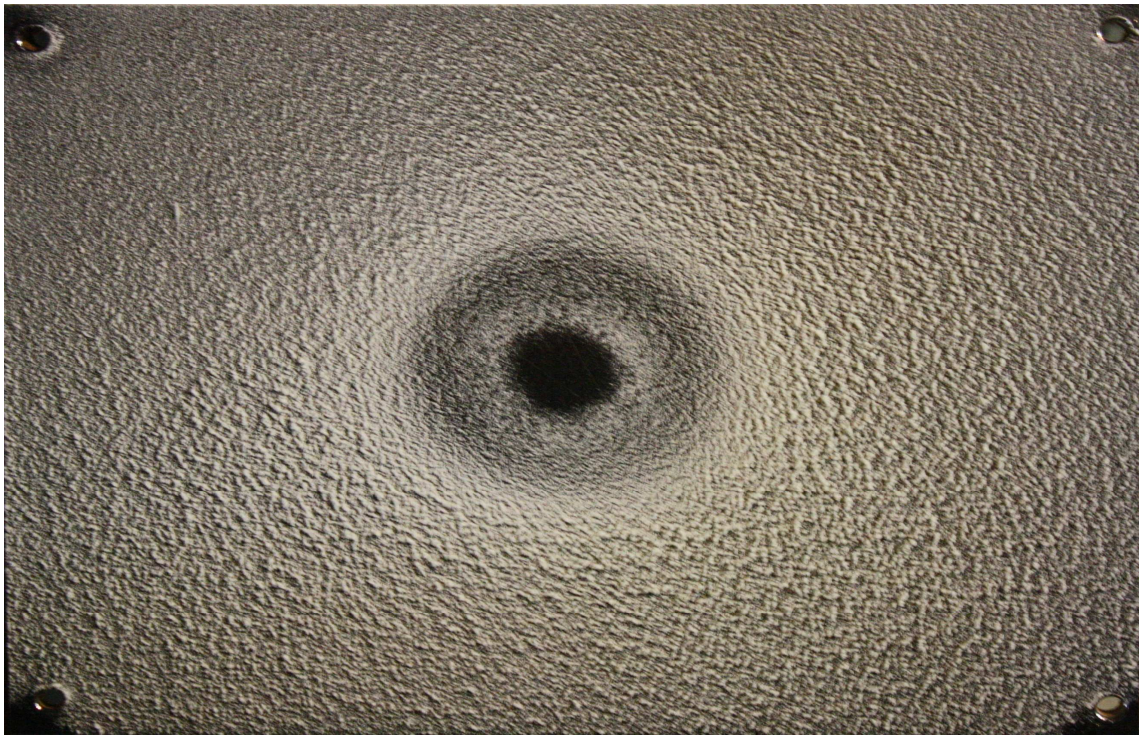

Figure A1.10 Deposit morphology at air velocity of 10.3 m/s and $45\mu m<d_p<63\mu m$ particle fraction. $T-T_g$ = 28.8 °C; % Dep = 28.98 %.

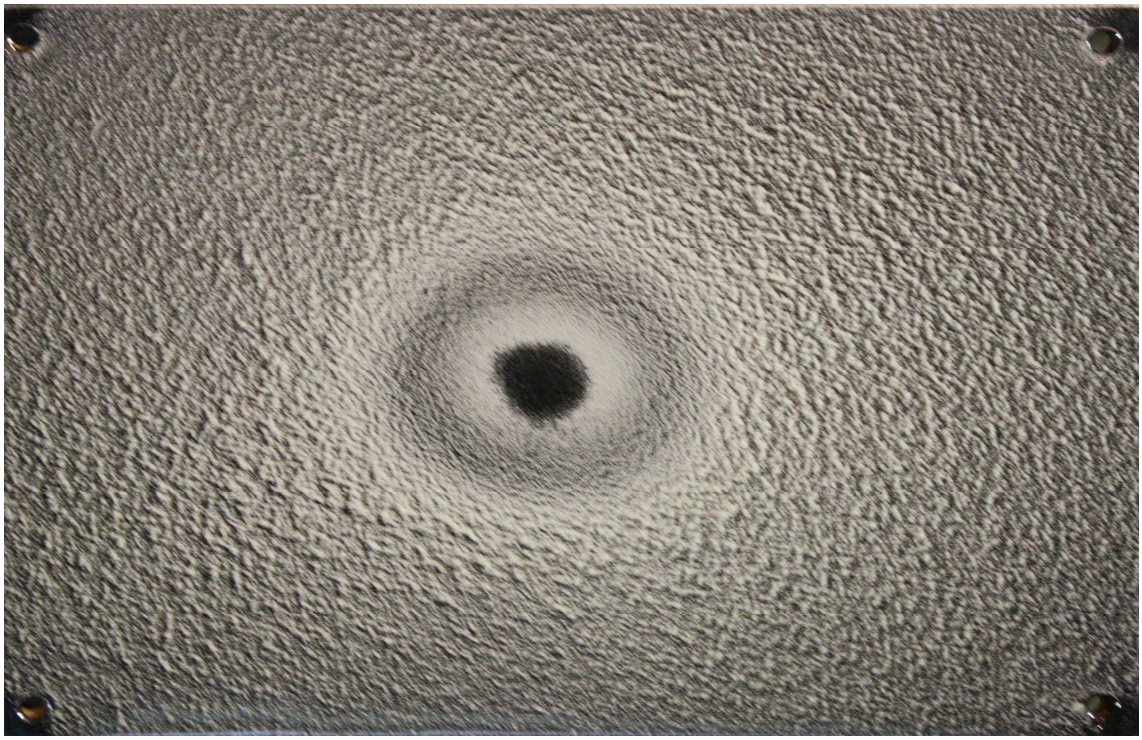

Figure A1.11 Deposit morphology at air velocity of 10.3 m/s and $45\mu m<d_p<63\mu m$ particle fraction. $T-T_g$ = 31.9 °C; % Dep = 32.10 %

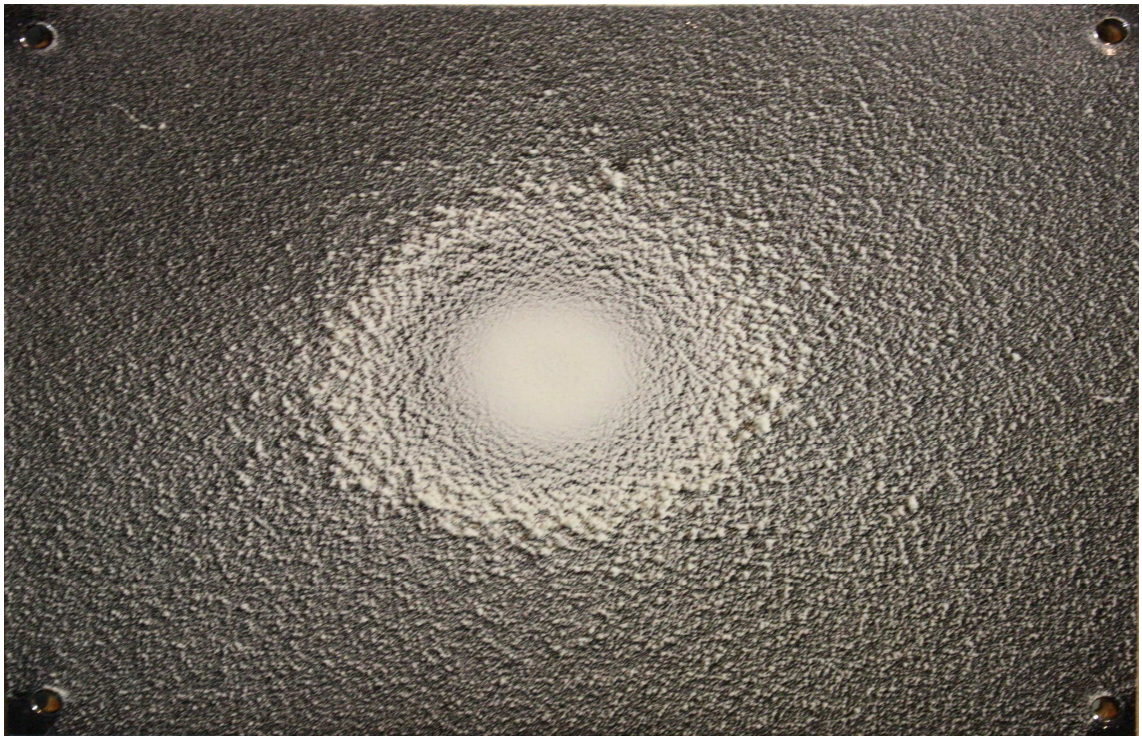

Figure A1.12 Deposit morphology at air velocity of 10.3 m/s and $45\mu m<d_p<63\mu m$ particle fraction. $T-T_g$ = 37.6 °C; % Dep = 34.12 %

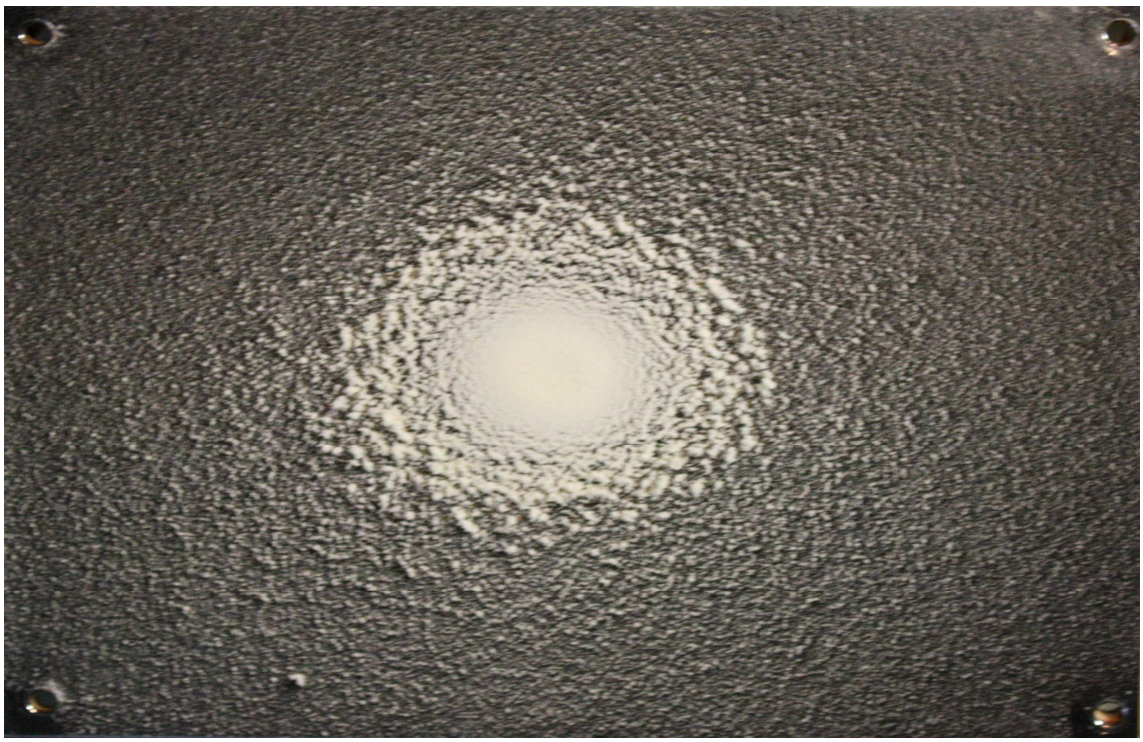

Figure A1.13 Deposit morphology at air velocity of 10.3 m/s and $45\mu m<d_p<63\mu m$ particle fraction. $T-T_g$ = 44.6 °C; % Dep = 44.08 %

A1.3 Air Velocity of 10.3 m/s and Bulk Particle Size

Figure A1.14 Deposit morphology at air velocity of 10.3 m/s and bulk particle fraction. T-T_g = 20.7 °C; % Dep = 3.20 %.

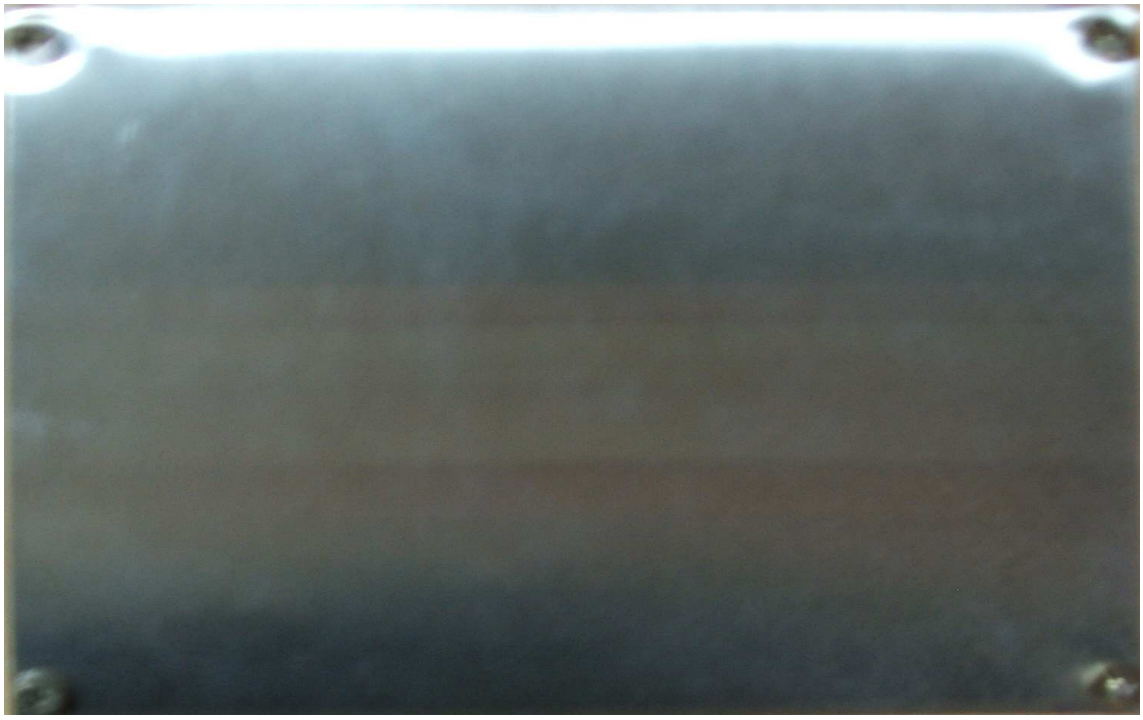

Figure A1.15 Deposit morphology at air velocity of 10.3 m/s and bulk particle fraction. T-T_g = 24.8 °C; % Dep = 5.12 %.

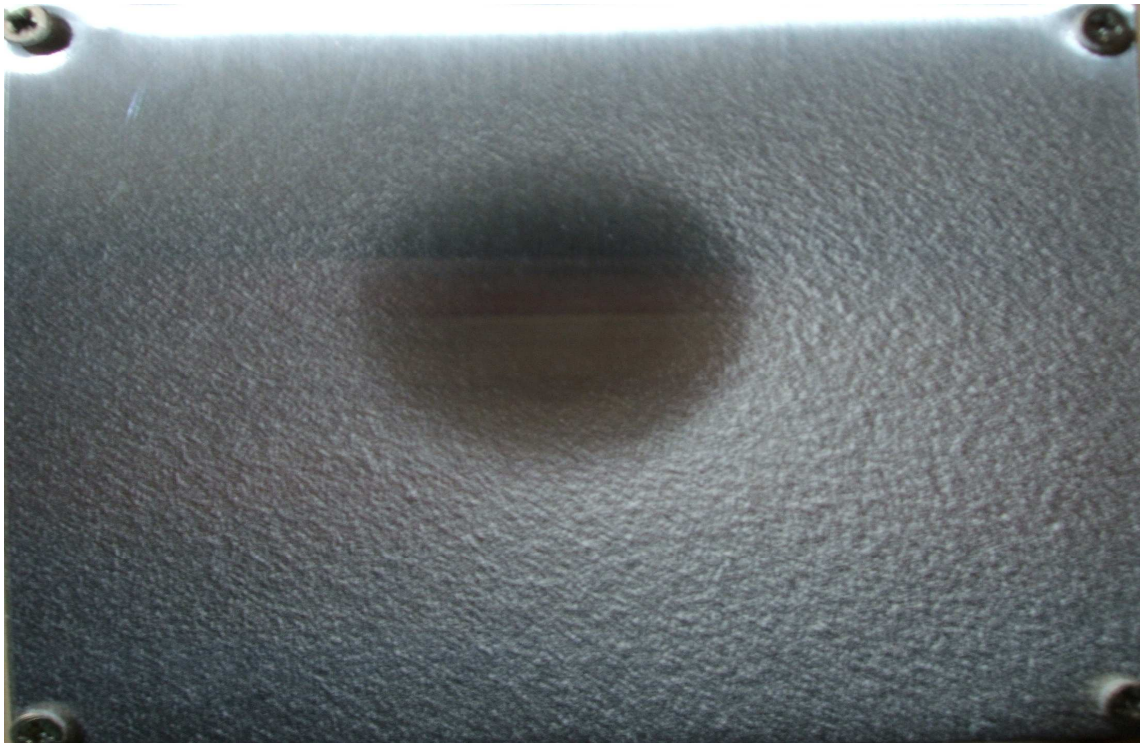

Figure A1.16 Deposit morphology at air velocity of 10.3 m/s and bulk particle fraction. T-T_g = 27.2 °C; % Dep = 8.30 %.

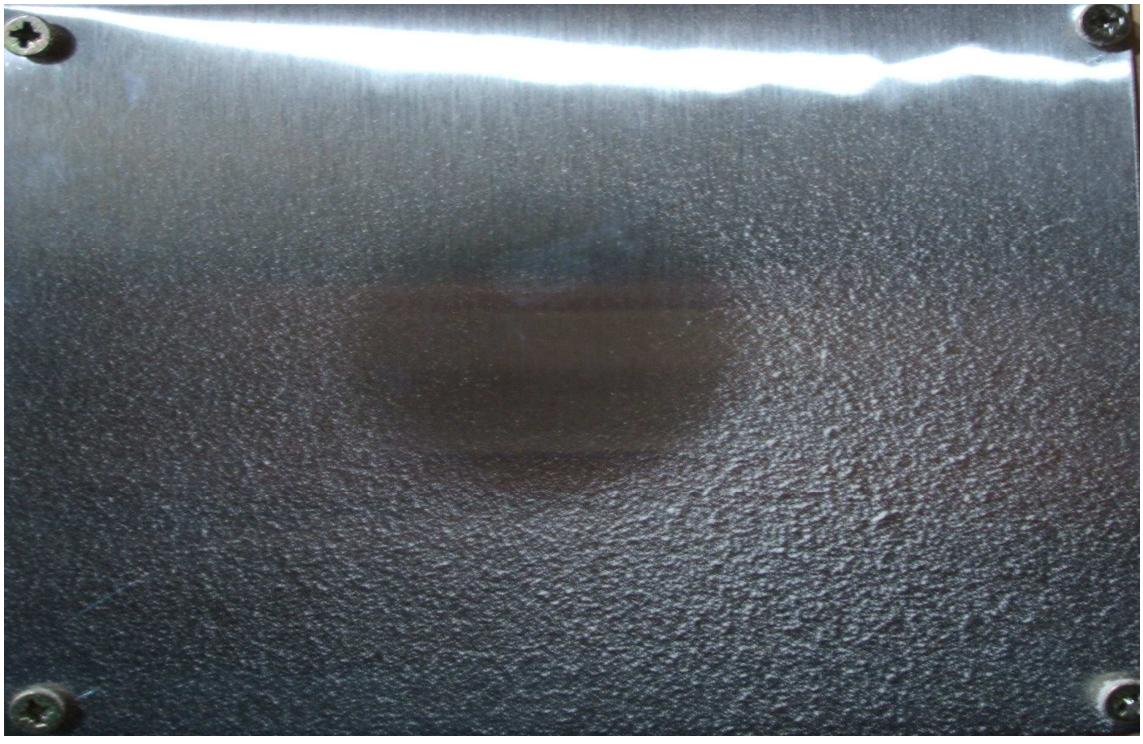

Figure A1.17 Deposit morphology at air velocity of 10.3 m/s and bulk particle fraction. T-T_g = 30.5 °C; % Dep = 13.48 %.

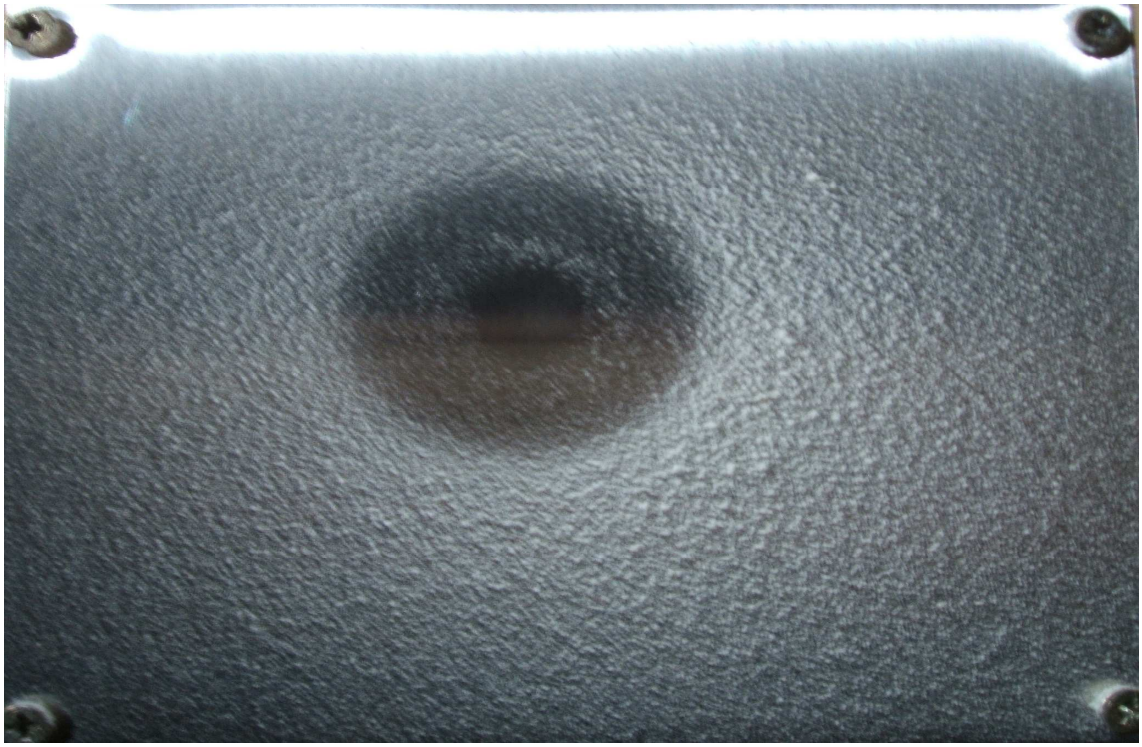

Figure A1.18 Deposit morphology at air velocity of 10.3 m/s and bulk particle fraction. T-T_g = 33.0 °C; % Dep = 12.9 %.

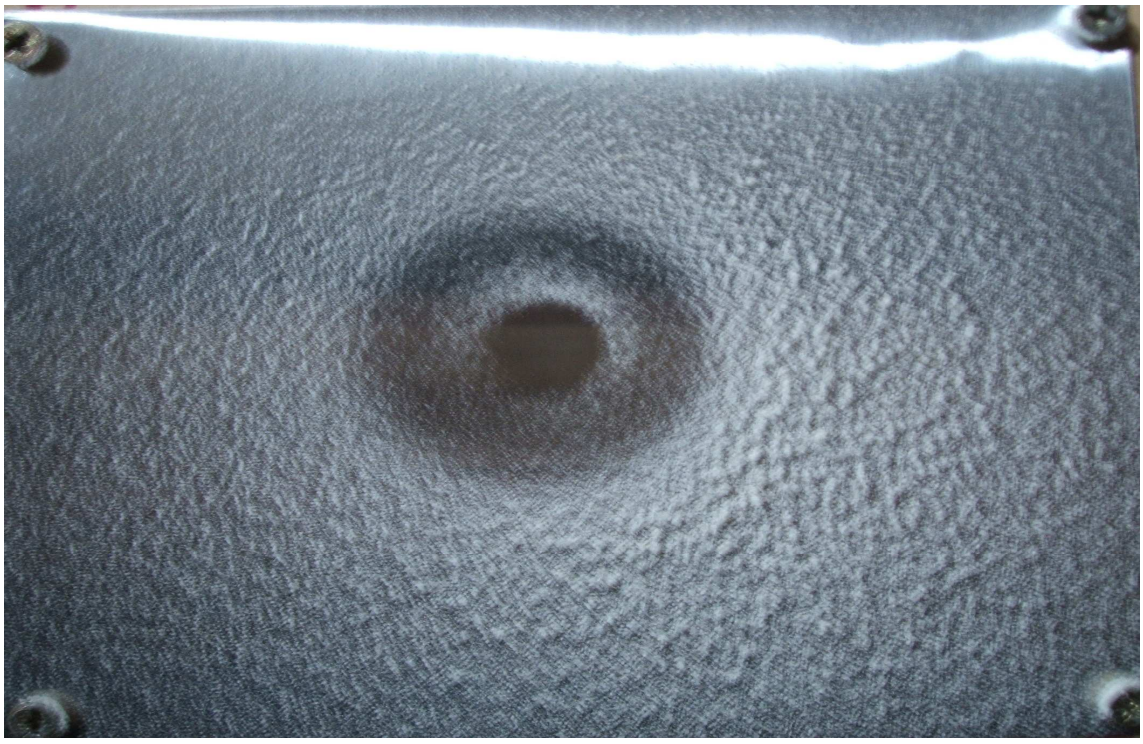

Figure A1.19 Deposit morphology at air velocity of 10.3 m/s and bulk particle fraction. T-T_g = 310.3 °C; % Dep = 23.27 %.

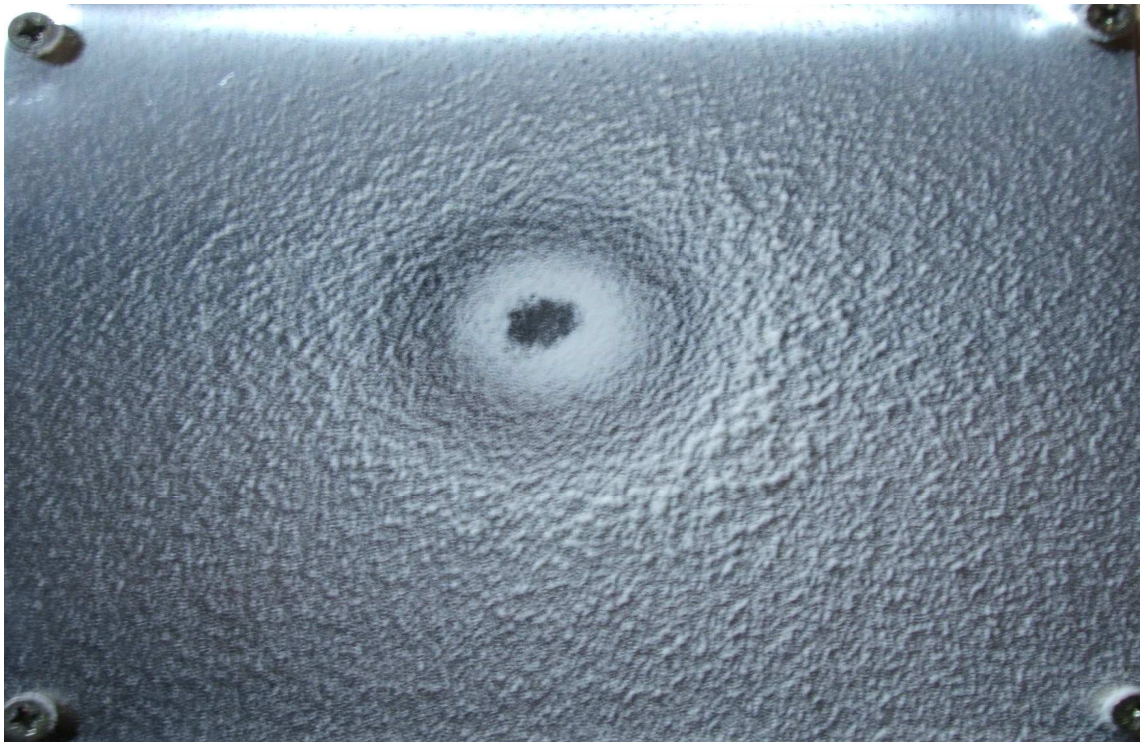

Figure A1.20 Deposit morphology at air velocity of 10.3 m/s and bulk particle fraction. T-T_g = 37.2 °C; % Dep = 19.20 %.

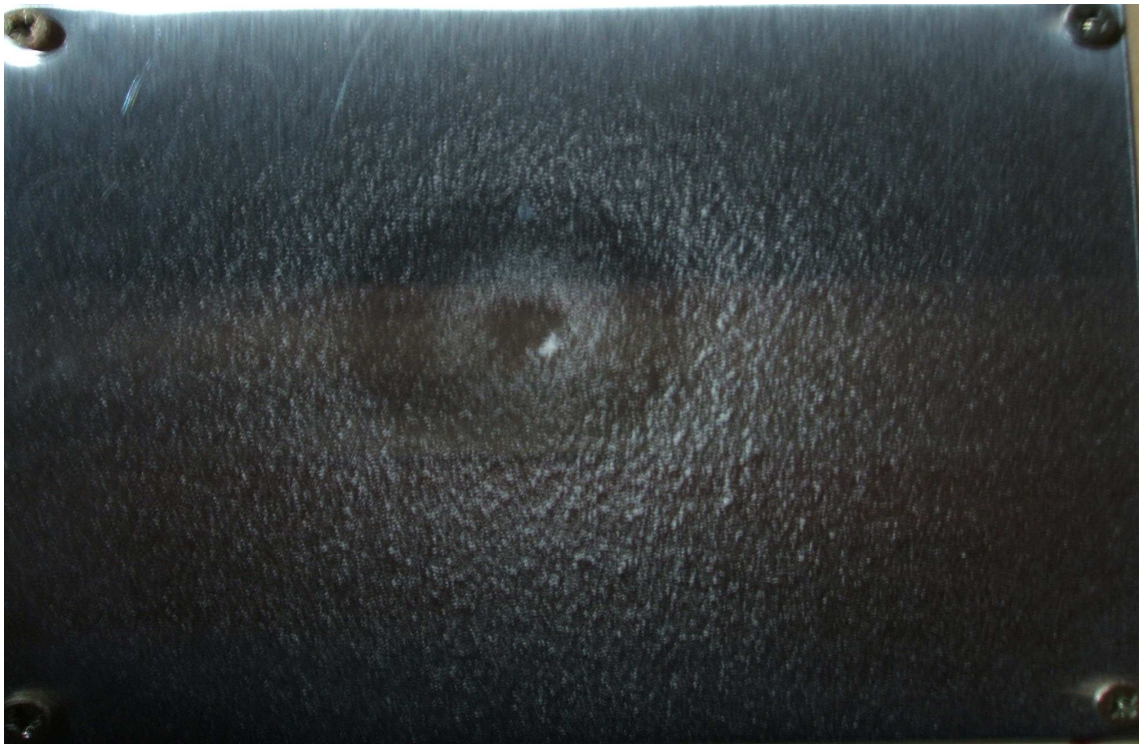

Figure A1.21 Deposit morphology at air velocity of 10.3 m/s and bulk particle fraction. T-T_g = 42.7 °C; % Dep = 13.04 %.

A1.4 Air Velocity of 14.8 m/s and Bulk Particle Size

Figure A1.22 Deposit morphology at air velocity of 14.8 m/s and bulk particle fraction. T-T_g = 15.3 °C; % Dep = 0.05 %.

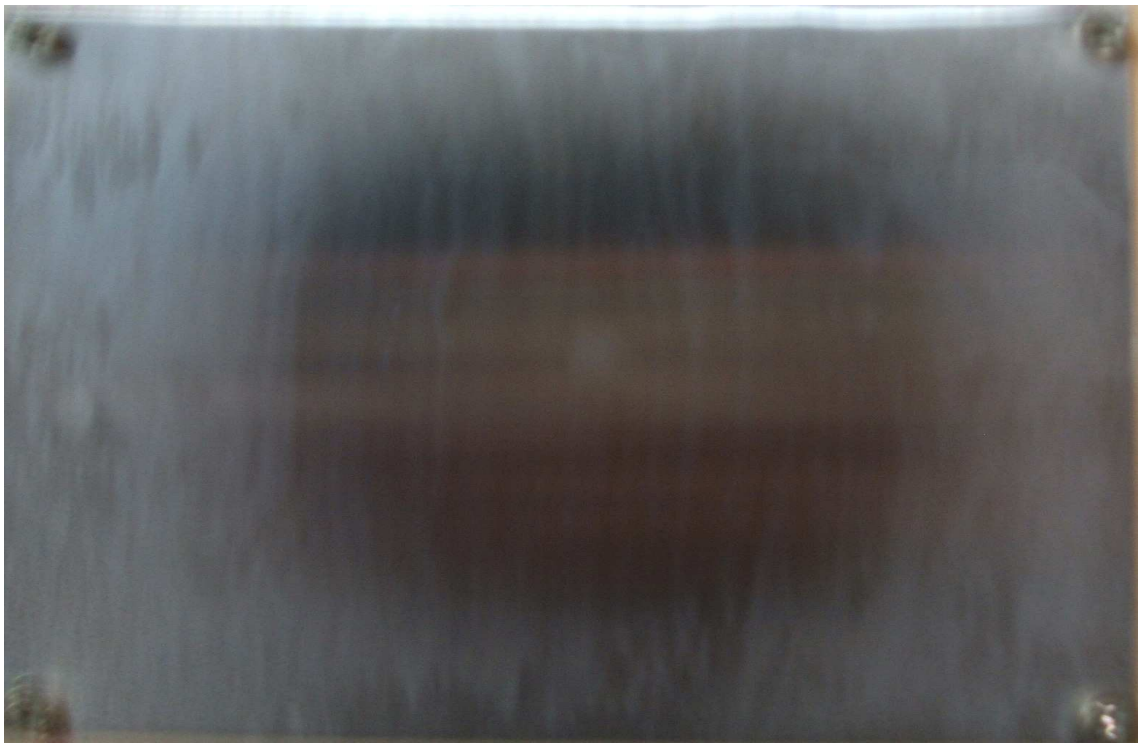

Figure A1.23 Deposit morphology at air velocity of 14.8 m/s and bulk particle fraction. T-T_g = 21.4 °C; % Dep = 0.4 %.

Figure A1.24 Deposit morphology at air velocity of 14.8 m/s and bulk particle fraction. T-T_g = 25.9 °C; % Dep = 1.38 %.

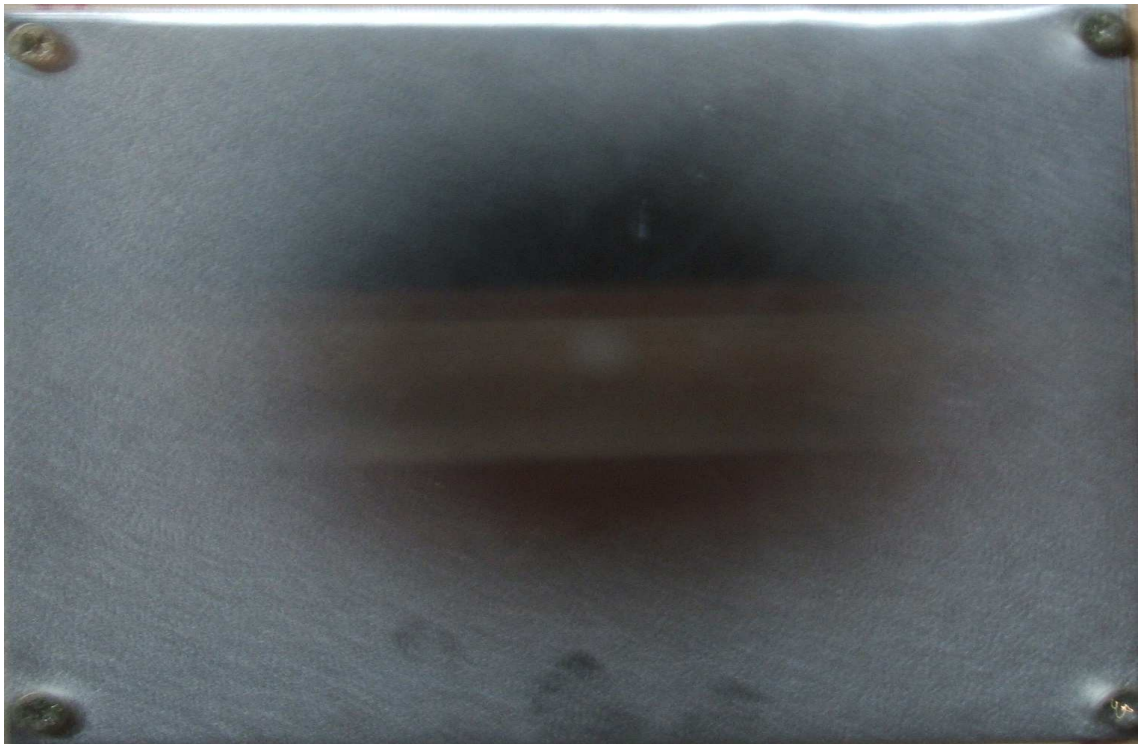

Figure A1.25 Deposit morphology at air velocity of 14.8 m/s and bulk particle fraction. T-T_g = 29.4 °C; % Dep = 1.47 %.

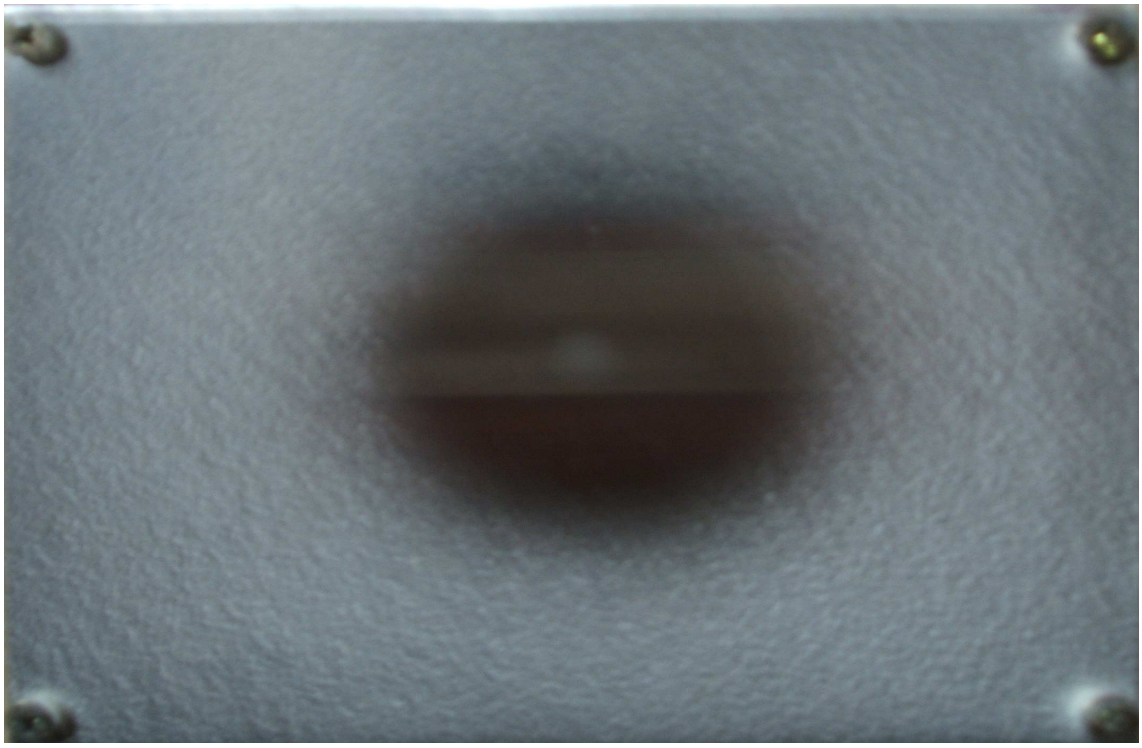

Figure A1.26 Deposit morphology at air velocity of 14.8 m/s and bulk particle fraction. T-T_g = 35.1 °C; % Dep = 3.82 %.

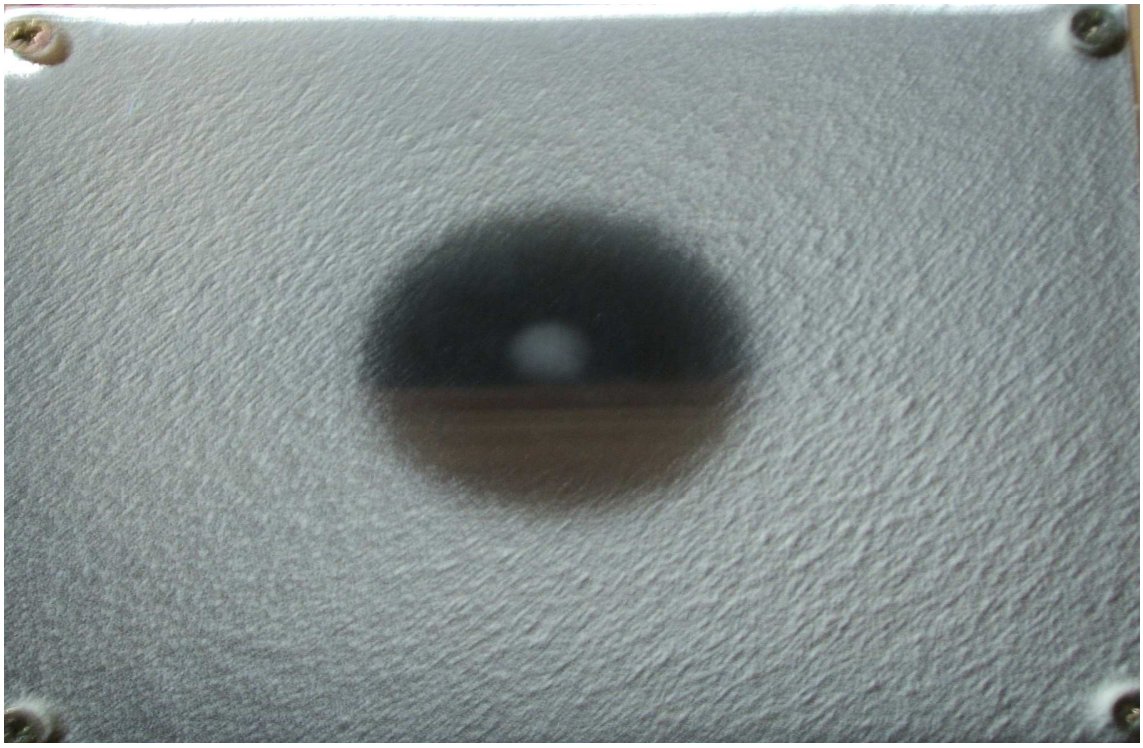

Figure A1.27 Deposit morphology at air velocity of 14.8 m/s and bulk particle fraction. T-T_g = 37.5 °C; % Dep = 9.28 %.

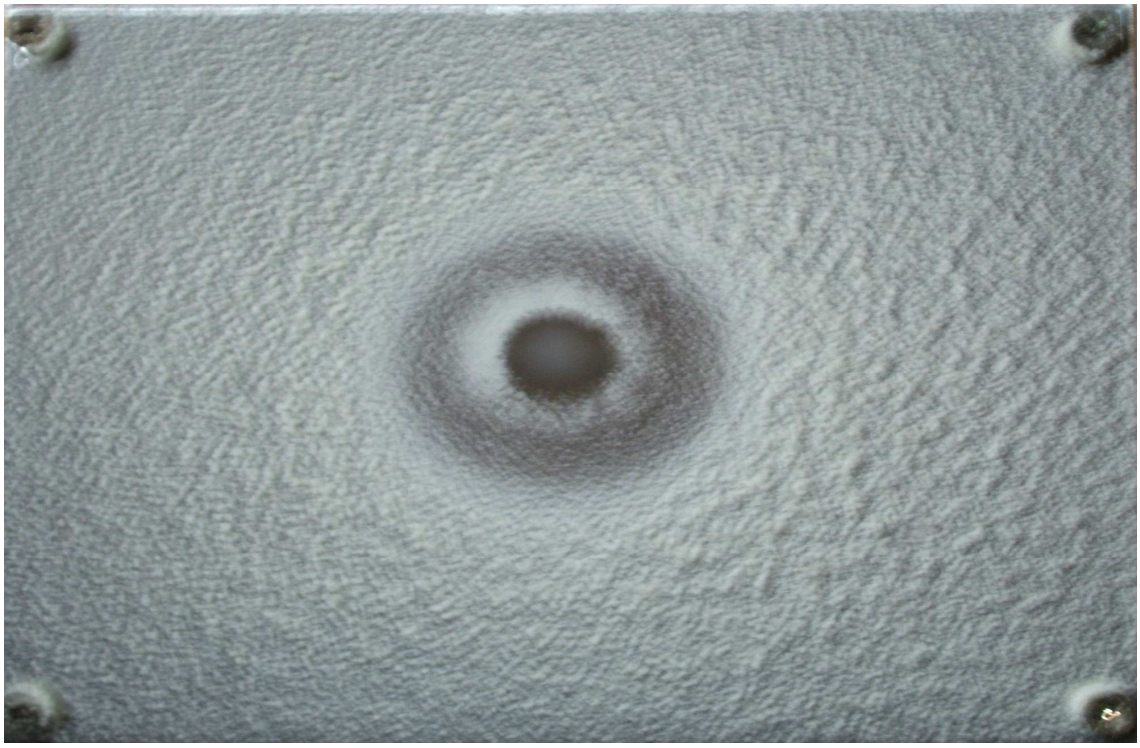

Figure A1.28 Deposit morphology at air velocity of 14.8 m/s and bulk particle fraction. T-T_g = 40.0 °C; % Dep = 21.13 %.

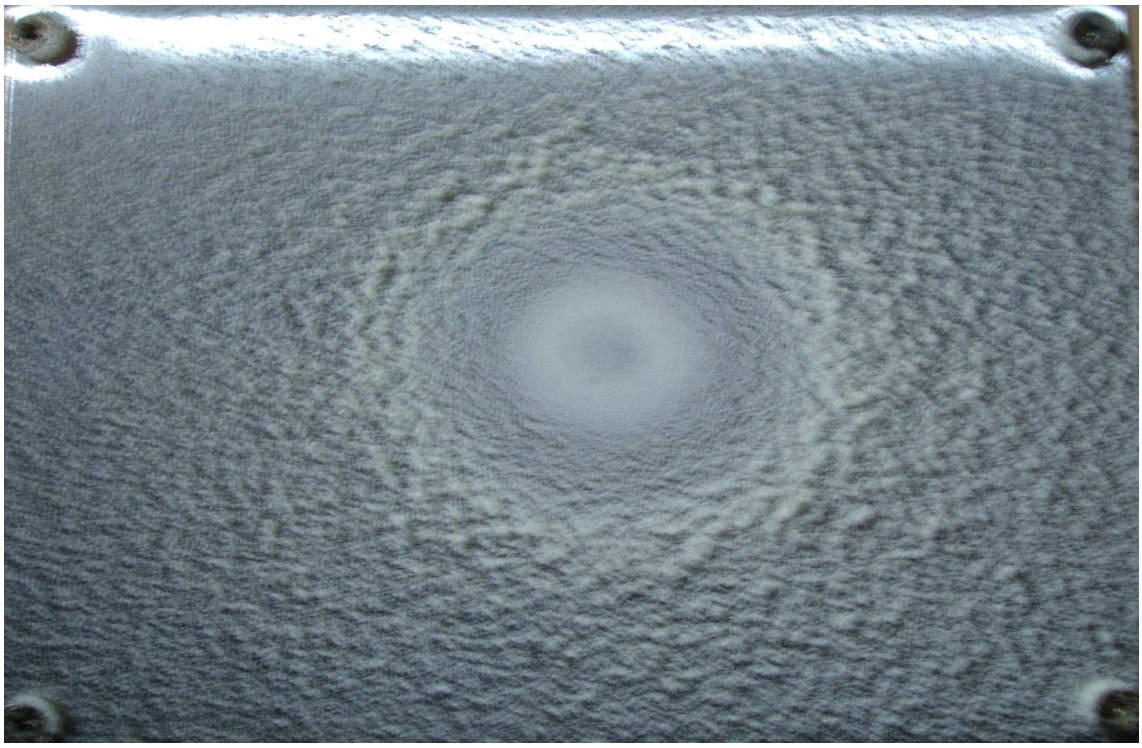

Figure A1.29 Deposit morphology at air velocity of 14.8 m/s and bulk particle fraction. T-T_g = 42.7 °C; % Dep = 26.07 %.

A1.5 Air Velocity of 10.3 m/s and d_p<45µm Particle Size, 45° of Impact

Figure A1.30 Deposit morphology at air velocity of 10.3 m/s, d_p<45µm particle size and 45° of impact. T-T_g = 16.6 °C; % Dep = 3.52 %.

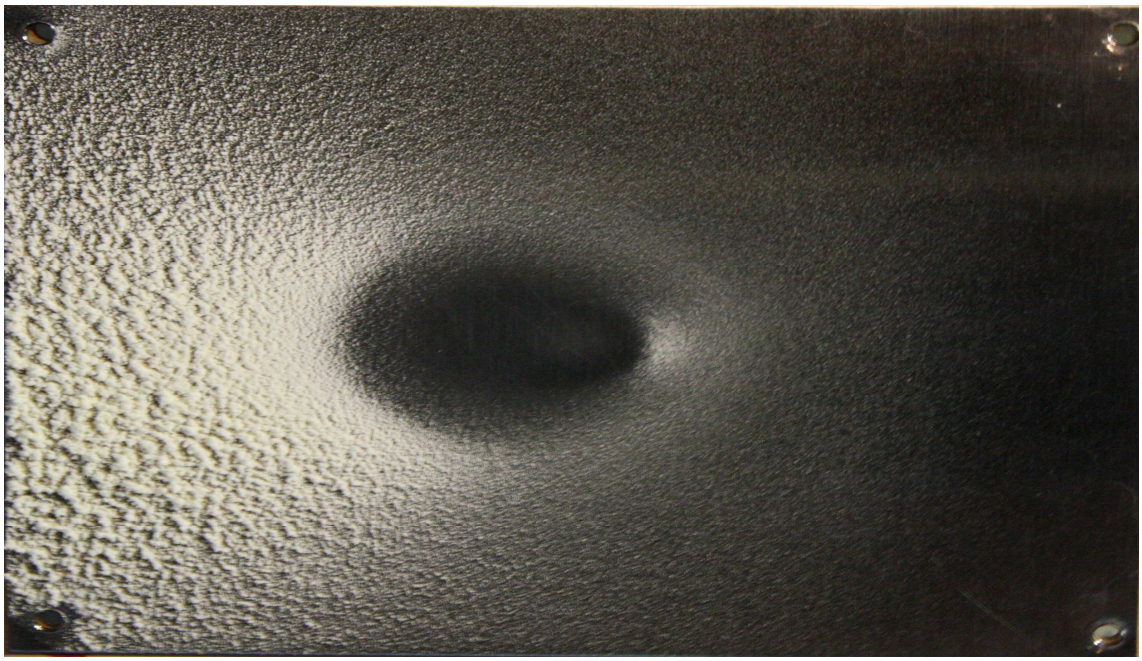

Figure A1.31 Deposit morphology at air velocity of 10.3 m/s, d_p<45µm particle size and 45° of impact. T-T_g = 210.3 °C; % Dep = 14.23 %.

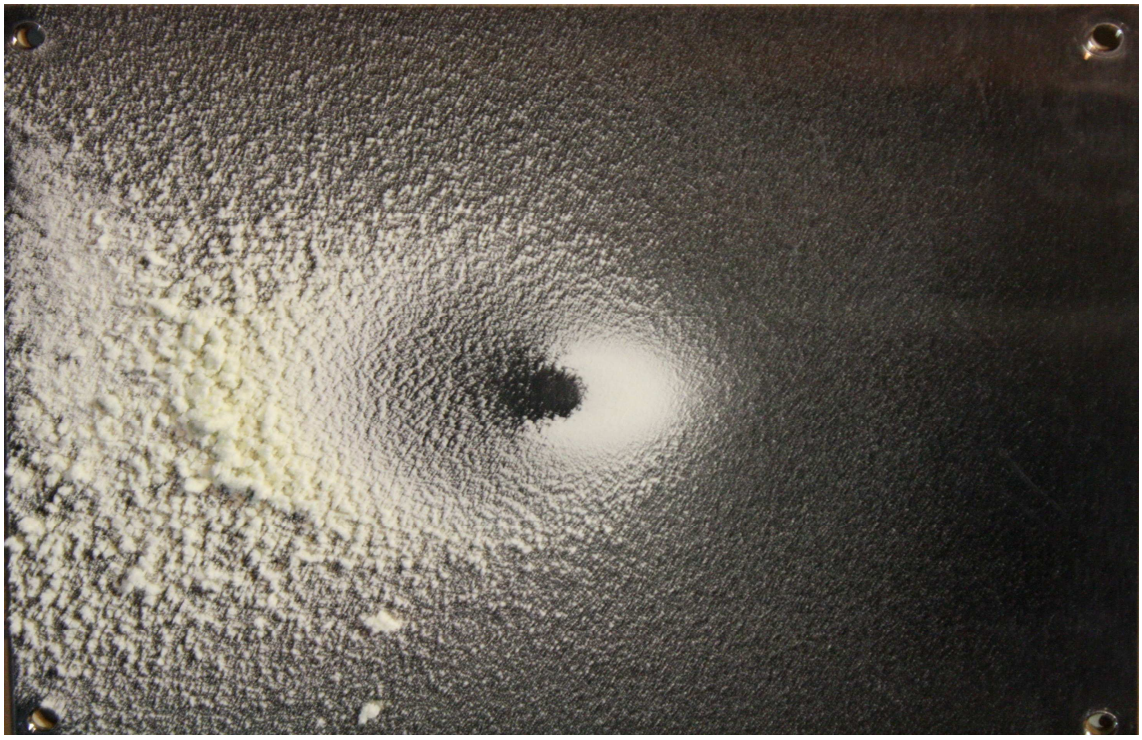

Figure A1.32 Deposit morphology at air velocity of 10.3 m/s, d_p<45µm particle size and 45° of impact. T-T_g = 33.1 °C; % Dep = 25.51 %.

Figure A1.33 Deposit morphology at air velocity of 10.3 m/s, d_p<45µm particle size and 45° of impact. T-T_g = 38.4 °C; % Dep = 37.96 %.

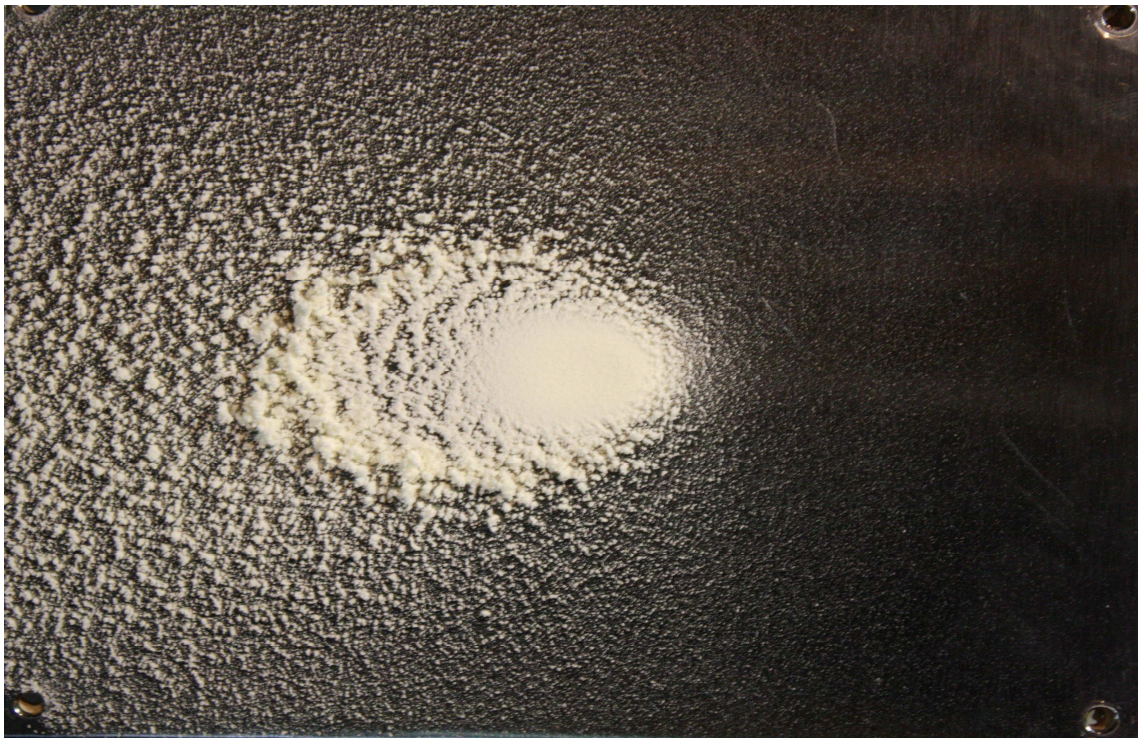

Figure A1.34 Deposit morphology at air velocity of 10.3 m/s, d_p<45µm particle size and 45° of impact. T-T_g = 42.9 °C; % Dep = 45.74 %.

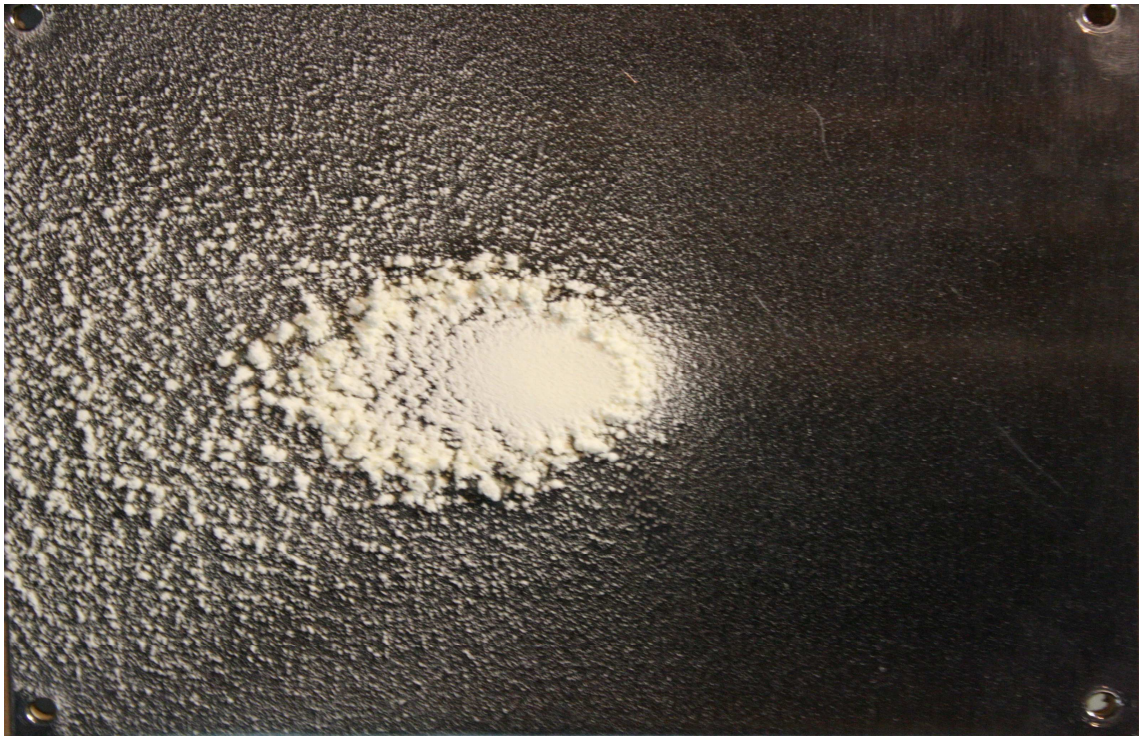

Figure A1.35 Deposit morphology at air velocity of 10.3 m/s, d_p<45µm particle size and 45° of impact. T-T_g = 47.7 °C; % Dep = 49.47 %.

APPENDIX 2- UDF IMPLMENTED IN FLUENT CONSIDERING ONLY THE CRITICAL NORMAL VELOCITY FOR DEPOSITION

```
/* wall boundary condition for inert particles */
#include "udf.h"


DEFINE_DPM_BC(walla,p,t,f,f_normal,dim)
{
   real normal_velocity = 0.;
   real tangential_velocity;
   real total_absolute_velocity;
   FILE * f1;
   real normal[3];
   int i, idim = dim;
   real NV_VEC(x);
   real particlemass = P_MASS(p);
   real Vcriticalnormal = 2;
   real Eloss;
   real Erebound;
   real Einormal;
   real Vreboundnormal;


#if RP_2D
   /* dim is always 2 in 2D compilation. Need special treatment for 2d
        axisymmetric and swirl flows */
   if (rp_axi_swirl)
      {
         real R = sqrt(p->state.pos[1]*p->state.pos[1] +
                              p->state.pos[2]*p->state.pos[2]);
         if (R > 1.e-20)
            {
               idim = 3;
               normal[0] = f_normal[0];
```

```
            normal[1] = (f_normal[1]*p->state.pos[1])/R;
            normal[2] = (f_normal[1]*p->state.pos[2])/R;
         }
      else
         {
            for (i=0; i<idim; i++)
               normal[i] = f_normal[i];
         }
   }
 else
#endif

for (i=0; i<idim; i++)
      normal[i] = f_normal[i];

 if(p->type==DPM_TYPE_INERT)

   {

      if ((NNULLP(t)) && (THREAD_TYPE(t) == THREAD_F_WALL))
         F_CENTROID(x,f,t);


  total_absolute_velocity = NV_MAG(p->state.V);

   /* next compute normal velocity. */

 for(i=0; i<idim; i++)
         normal_velocity += p->state.V[i]*normal[i]; /* this produces a scalar */

 /* Subtract off normal velocity to get tangential velocity */

 for(i=0; i<idim; i++)
         p->state.V[i] -= normal_velocity*normal[i]; /*this produces a vector which is the orginal velocity less the normal velocity */

 tangential_velocity = NV_MAG(p->state.V); /* this calculates absolute tangential velocity from vector less normal velocity */


 Eloss = 0.5 * particlemass * Vcriticalnormal * Vcriticalnormal;

 Einormal = 0.5 * particlemass * normal_velocity * normal_velocity;
```

```
    Erebound = Einormal - Eloss;

    Erebound = MAX (Erebound, 0);

    Vreboundnormal = sqrt(2 * Erebound / particlemass);


if (Erebound == 0)

     {

     f1= fopen("D:\\55 walla.txt","a");


     fprintf(f1,"%d %e %e %e %e %e %e \n",p->part_id,normal_velocity,
tangential_velocity,P_POS(p)[0], P_POS(p)[1], P_POS(p)[2], P_MASS(p));

     fclose(f1); /* close the file pointed to by f1 */

     p->stream_index=-1;

     return PATH_ABORT;

     }

   else
     {

       for(i=0; i<idim; i++)
       p->state.V[i] *= 1; /* 1 is the tan COR, this computes rebound tan_velocity in vector form */

       for(i=0; i<idim; i++)
       p->state.V[i]-= Vreboundnormal * normal[i]; /* 1 is the normal COR, this computes rebound
normal velocity in vector form */

       for(i=0; i<idim; i++)
       p->state0.V[i] = p->state.V[i];

       return PATH_ACTIVE; } } }
```

APPENDIX 3 - CFD SIMULATION OF PARTICLE DEPOSITION, WITH VT/VN< 30 INCLUDED

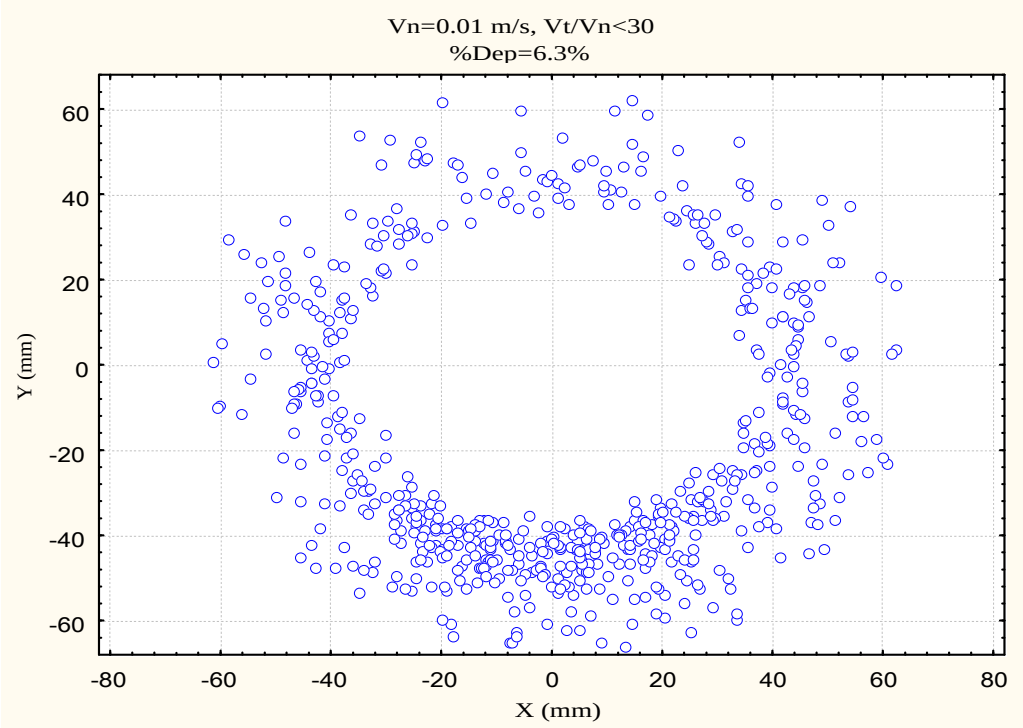

Figure A3.1 Deposit morphology for the CFD simulation with V_n = 0.01 m/s, V_t/V_n<30.

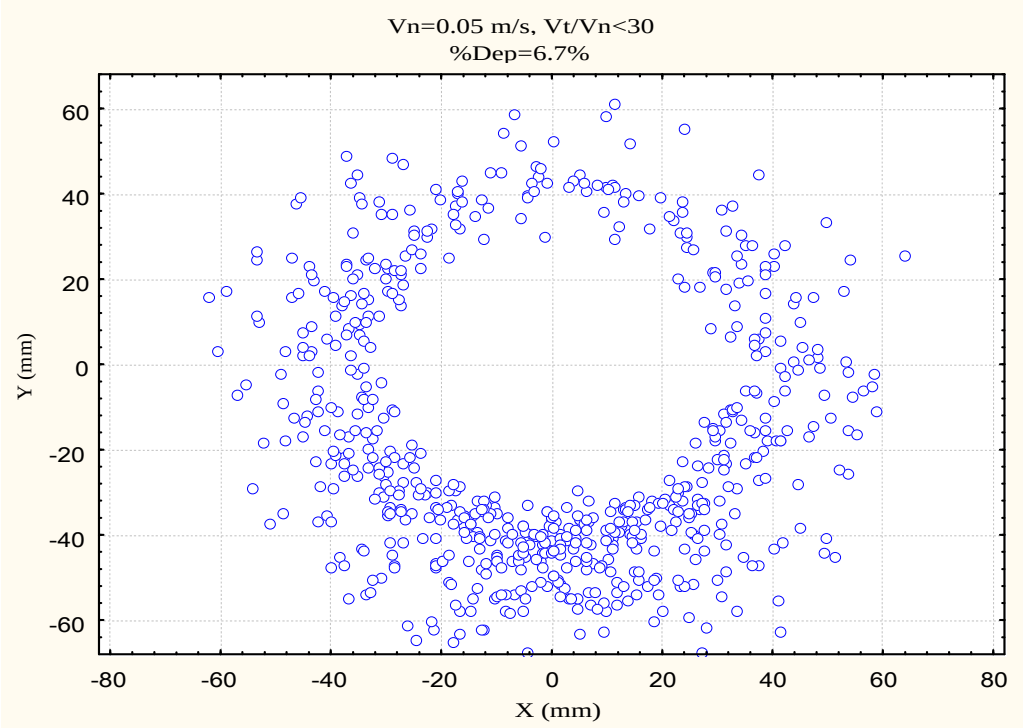

Figure A3.2 Deposit morphology for the CFD simulation with V_n = 0.05 m/s, V_t/V_n<30.

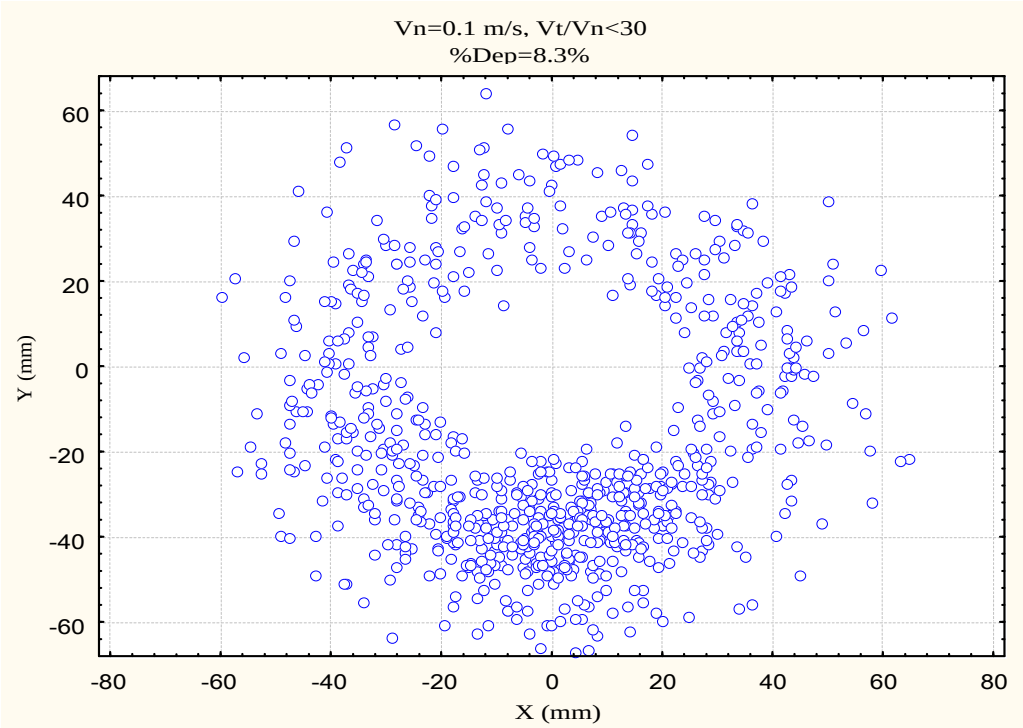

Figure A3.3 Deposit morphology for the CFD simulation with V_n = 0.1 m/s, V_t/V_n<30.

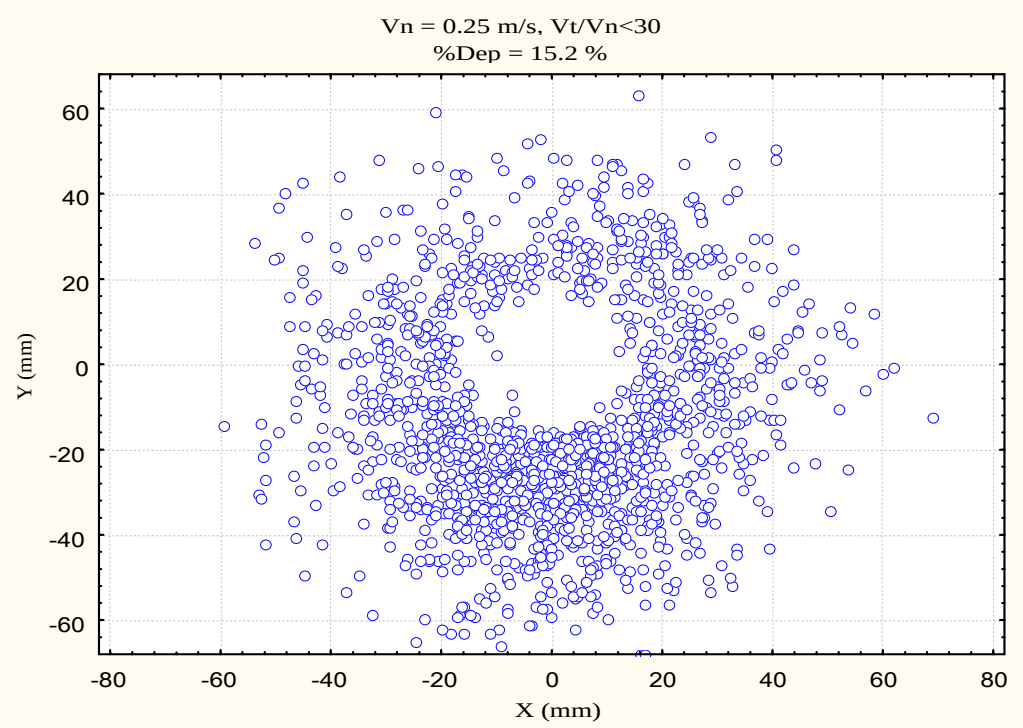

Figure A3.4 Deposit morphology for the CFD simulation with V_n = 0.25 m/s, V_t/V_n<30.

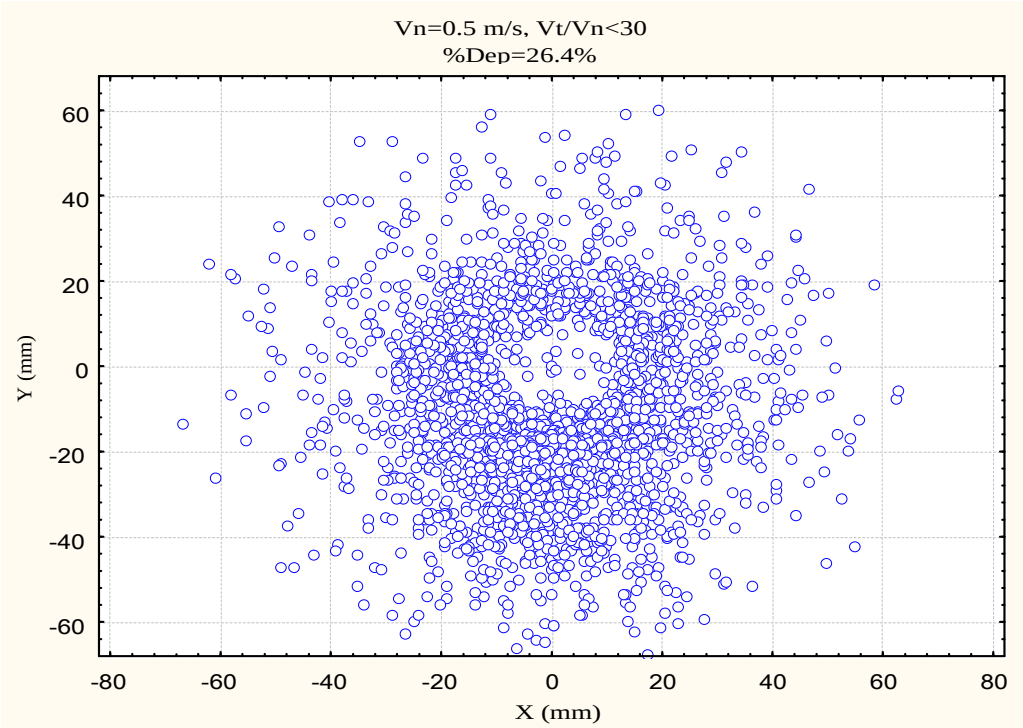

Figure A3.5 Deposit morphology for the CFD simulation with V_n = 0.5 m/s, V_t/V_n<30.

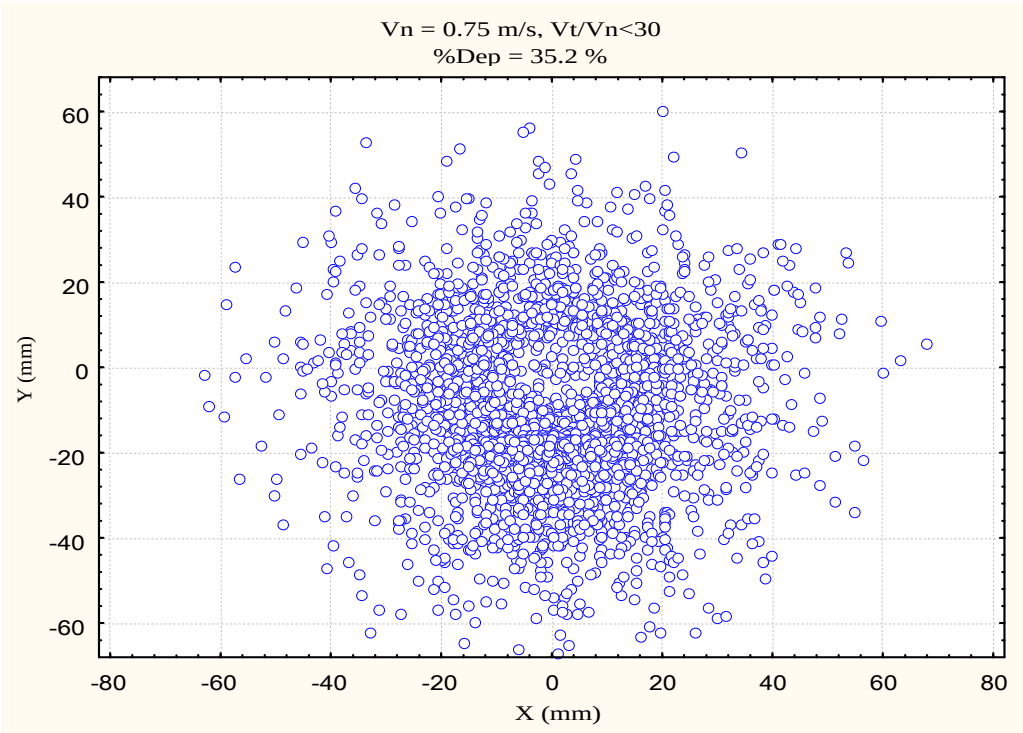

Figure A3.6 Deposit morphology for the CFD simulation with V_n = 0.75 m/s, V_t/V_n<30.

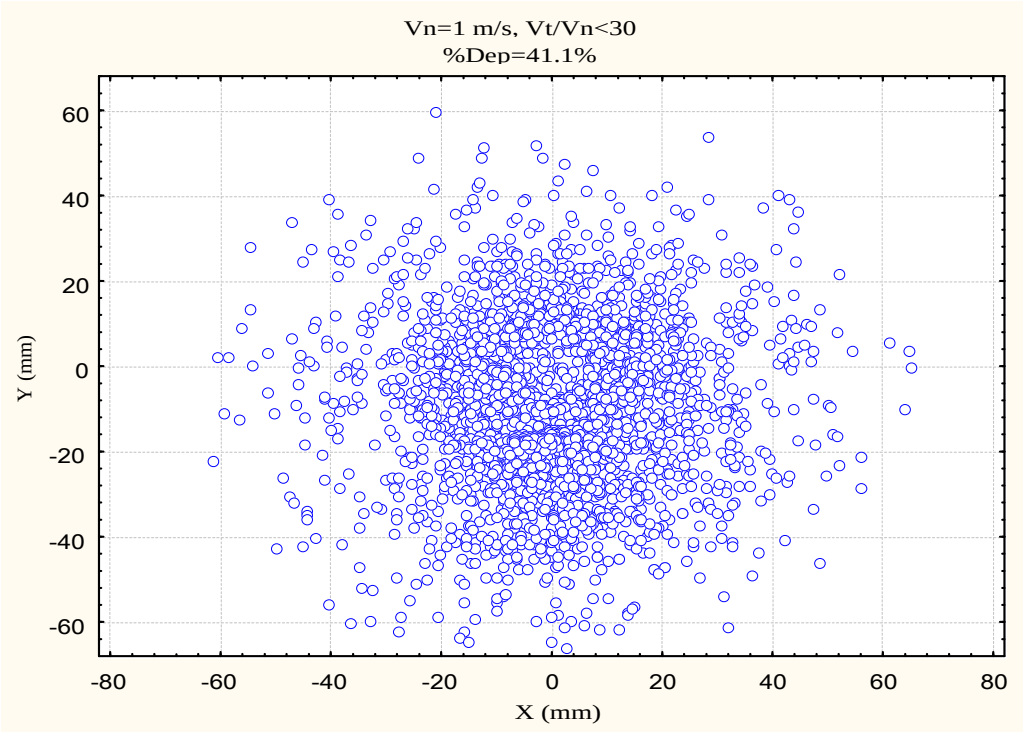

Figure A3.7 Deposit morphology for the CFD simulation with V_n = 1 m/s, V_t/V_n<30.

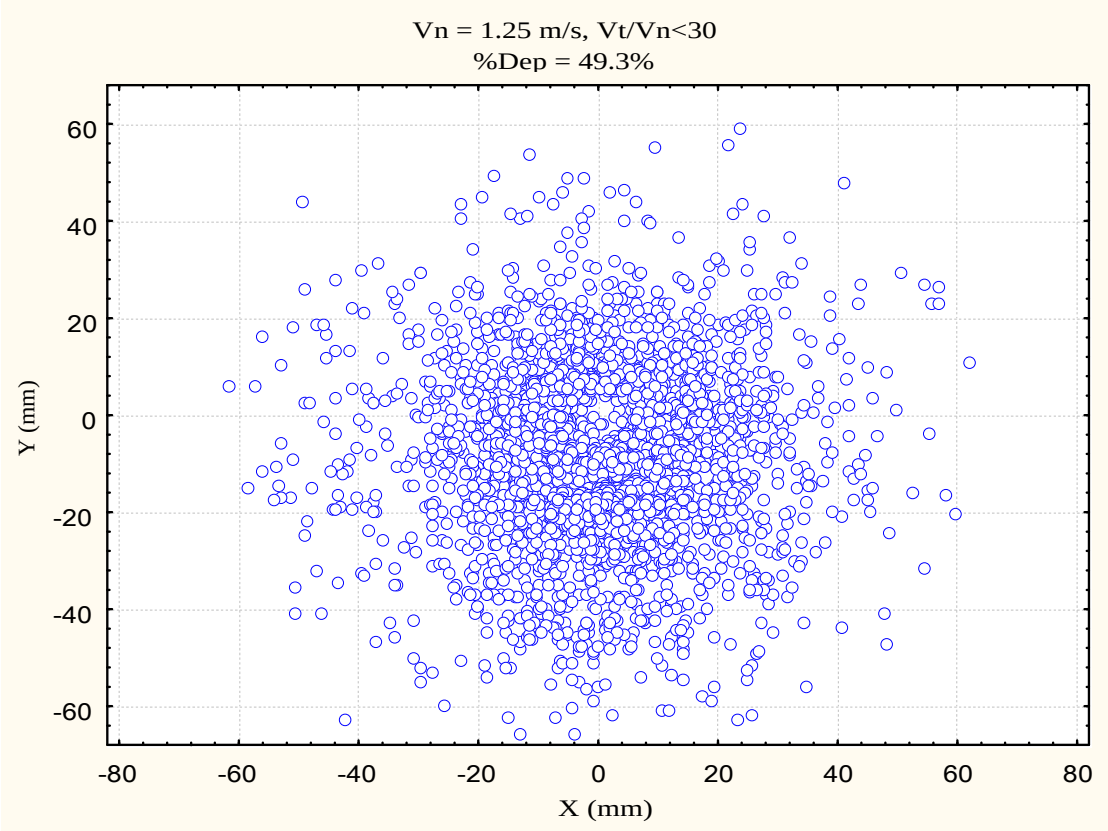

Figure A3.8 Deposit morphology for the CFD simulation with V_n = 1.25 m/s, V_t/V_n<30.

APPENDIX 4 - CONTRIBUTION TO THE TOTAL %DEPOSITED PARTICLES FROM EACH PARTICLE SIZE FRACTION

Table A4.1. Contributions to total %deposition from different particle size classes.

Vn(m/s)	2	1.5	1.25	1	0.75	0.5	0.25	0.1	0.05	0.01
Total Number Deposited	6560	5696	4971	4375	3594	3024	2194	1158	707	296
No. of <22.8 um	661	621	585	503	444	343	243	116	62	38
%	10.1	10.9	11.8	11.5	12.4	11.3	11.1	10.0	8.8	12.8
No. of 22.8 um< dp <30.1 um	672	605	505	433	348	286	165	100	80	55
%	10.2	10.6	10.2	9.9	9.7	9.5	7.5	8.6	11.3	18.6
No. of 30.1 um< dp <37.3 um	689	578	496	428	322	257	159	90	73	63
%	10.5	10.1	10.0	9.8	9.0	8.5	7.2	7.8	10.3	21.3
No. of 37.3 um< dp <44.6 um	710	586	499	452	363	320	185	109	94	53
%	10.8	10.3	10.0	10.3	10.1	10.6	8.4	9.4	13.3	17.9
No. of 44.6 um< dp <51.8 um	798	663	550	447	364	318	227	107	67	27
%	12.2	11.6	11.1	10.2	10.1	10.5	10.3	9.2	9.5	9.1
No. of 51.8 um< dp <59 um	769	662	607	552	424	344	242	117	76	31
%	11.7	11.6	12.2	12.6	11.8	11.4	11.0	10.1	10.7	10.5
No. of 59 um< dp <66.3 um	680	633	556	549	457	389	316	136	90	19
%	10.4	11.1	11.2	12.5	12.7	12.9	14.4	11.7	12.7	6.4
No. of 66.3 um< dp <73.5 um	526	481	421	390	359	334	280	173	85	7
%	8.0	8.4	8.5	8.9	10.0	11.0	12.8	14.9	12.0	2.4
No. of 73.5 um< dp <80.8 um	526	431	378	340	294	238	222	124	54	2
%	8.0	7.6	7.6	7.8	8.2	7.9	10.1	10.7	7.6	0.7
No. of 80.8 um< dp <88 um	529	436	374	281	219	195	155	86	26	1
%	8.1	7.7	7.5	6.4	6.1	6.4	7.1	7.4	3.7	0.3